INVESTIGATION OF THE EFFECT OF SYNTHESIS PARAMETERS AND FORMATION KINETICS ON THE STRUCTURE, MECHANICAL PERFORMANCE AND METHYLENE BLUE ADSORPTION OF ALKALI ACTIVATED MAGNESIUM SILICATES

by

Serhat Arca

B.S., Chemical Enginering, Boğaziçi University, 2013

M.S., Chemical Enginering, Boğaziçi University, 2016

Submitted to the Institute for Graduate Studies in
Science and Engineering in partial fulfillment of
the requirements for the degree of
Doctor of Philosophy

Graduate Program in Chemical Engineering

Boğaziçi University

2023

ACKNOWLEDGEMENTS

Firstly, I would like to thank my supervisor Prof. Sezen Soyer Uzun for her patience and support throughout my study. She provided an environment where I could focus on my research and her guidance helped me to gain new perspectives.

I also want to thank Prof. Ramazan Yıldırım, Prof. Uğur Ünal, Prof. Ahmet Erhan Aksoylu and Samira Fatma Kurtoğlu Öztulum, Ph.D. for their valuable comments and suggestions on my thesis as committee members.

Special thanks to Prof. Nilüfer Özyurt Zihnioğlu and Onur Öztürk for their support. I would like to thank Dr. Barış Yağcı and all other KUYTAM members for their help in my studies. Thanks to Prof. Burak Alakent for his guidance and help in modeling studies.

I am thankful to Feyza Kevser Öner and Kardelen Kaya Özkiper, Ph.D. for being so helpful and supporting me throughout my studies.

Finally, I would like to express my thanks to my beloved family members for their support throughout my life. They always contributed to my success and helped me with everything. Last but not least, I would like thank my dear wife Elif Erdinç Arca for her support, love and understanding. She was always there to support me whenever I needed.

The financial support provided by Boğaziçi University Research Fund through Project BAP 15281 is gratefully acknowledged.

ABSTRACT

INVESTIGATION OF THE EFFECT OF SYNTHESIS PARAMETERS AND FORMATION KINETICS ON THE STRUCTURE, MECHANICAL PERFORMANCE AND METHYLENE BLUE ADSORPTION OF ALKALI ACTIVATED MAGNESIUM SILICATES

Alkali activated materials (AAM), commonly referred as geopolymers, are environmentally friendly alternatives to Portland cement with their remarkable mechanical strength. In this thesis, the main motivation is to investigate the effects of synthesis parameters and formation kinetics on the structure, mechanical performance, and methylene blue (MB) adsorption properties of alkali activated magnesium silicates. The raw materials and the SAAMs are characterized by combining X-ray fluorescence (XRF) spectroscopy, X-ray diffraction (XRD), thermogravimetric analysis (TGA), and X-ray photoelectron spectroscopy (XPS). Attenuated total reflectance Fourier-transform infrared (ATR-FTIR) spectroscopic data is collected at different reaction times to shed light on the relation between the geopolymerization kinetics and the compressive strength. The results indicated that increasing pretreatment temperature has a negative impact, while increasing Si/Mg ratio has a positive impact on the compressive strength. The kinetics of geopolymerization is quantified by fitting exponential functions to the position of the main FTIR peak over time. The analysis demonstrated that early geopolymerization (time scales < 4 h) is a big contributor to the compressive strength. The highest MB removal capacity was obtained as 110.42 mg/g with a molar Na/Mg ratio of 1.3, a sepiolite treatment temperature of 750 °C and a molar Si/Mg ratio of 2.5. The ANOVA analysis showed a correlation coefficient (R^2) of 0.865 and lack of fit was found to be non-significant. From the model, the optimum values of molar Na/Mg ratio, temperature and molar Si/Mg ratio are found to be 1.3, 697 °C and 2.4, respectively. The findings of this thesis demonstrate that SAAMs can be economical and sustainable alternatives for construction and wastewater treatment applications with their remarkable mechanical strength and enhanced adsorption performance.

ÖZET

SENTEZ KOŞULLARININ VE OLUŞUM KİNETİĞİNİN MAGNEZYUM SİLİKAT BAZLI ALKALİ AKTİF MALZEMELERİN YAPISI, MEKANİK ÖZELLİKLERİ VE METİLEN MAVİSİ ADSORPLAMA ÖZELLİKLERİ ÜZERİNE ETKİSİ

Alkali aktif malzemeler (AAM), yüksek mekanik performanslarıyla Portland çimentoya alternatif olabilecek çevre-dostu malzemelerdir. Bu tezin amacı, magnezyum silikat içerikli AAM'ler için sentez koşullarının ve oluşum kinetiğinin yapı, mekanik dayanım ve metilen mavisi (MB) adsorplama özellikleri üzerine etkilerinin araştırılmasıdır. Bu amaçla ilk olarak, istatistiksel bir deney tasarımı kullanılarak sentez koşullarının sepiyolit bazlı AAM'lerin (SAAM) basma kuvveti üzerine etkileri incelenmiştir. Ham maddeler ve sentezlenen malzemeler, X-ışını floresans (XRF) spektroskopisi, X-ışını kırınım (XRD), termogravimetrik analiz (TGA) ve X-ışını fotoelektron spektroskopi yöntemleriyle karakterize edilmiştir. Azaltılmış tam yansıma Fourier dönüşümlü kızılötesi spektroskopisi (ATR-FTIR) verisi değişik reaksiyon sürelerinde toplanarak jeopolimerleşme kinetiği ve basma kuvveti arasındaki ilişkinin belirlenmesi amaçlanmıştır. Artan sepiyolit ön işlem sıcaklığının basma kuvvetini düşürdüğü, diğer taraftan artan molar Si/Mg oranının basma kuvveti üzerinde positif bir etkisi olduğu tespit edilmiştir. Jeopolimerleşme kinetiğinin sayısal verilere dökülmesi amacıyla, toplanan FTIR verilerinde temel bant pozisyounun zamana bağlı değişiminin üstel bir fonksiyona oturtulmuştur. Yapılan analiz, erken evre jeopolimerleşmenin (süre < 4 sa) basma kuvveti üzerindeki etkisinin oldukça yüksek olduğunu göstermiştir. En yüksek MB adsorplama kapasitesi Na/Mg oranının 1.3, sepiyolit ön işlem sıcaklığının 750 °C ve Si/Mg oranının 2.5 olduğu durumda elde edilmiştir. Varyans analizi (ANOVA) sonucunda korelasyon katsayısı (R^2) 0.865 olarak belirlenmiştir. Model kullanılarak optimum sentez koşulları Na/Mg oranı için 1.3, ön işlem sıcaklığı için 697 °C ve Si/Mg oranı için 2.4 olarak tespit edilmiştir. Tez sonucunda SAAM'ların yapı ve atıksu arıtım endüstrilerinde ekonomik ve sürdürülebilir alternatifler olabilecekleri belirlenmiştir.

TABLE OF CONTENTS

LIST OF SYMBOLS

at	Atomic
C	Concentration
h	Hour
q	Uptake
T	Temperature
t	Time
V	Volume
wt	Weight

LIST OF ACRONYMS/ABBREVIATIONS

AAM	Alkali activated material
Al	Aluminum
ATR	Attenuated total reflectance
BET	Brunauer Emmett Teller
CO_2	Carbondioxide
FGP	Fly ash-based geopolymer
FTIR	Fourier transform infrared spectroscopy
H_2O_2	Hydrogen peroxide
MB	Methylene blue
MK	Metakaolin
MKG	Metakaolin-based geopolymer
NaOH	Sodium hydroxide
$Na_2Si_3O_7$	Sodium silicate
SAAM	Sepiolite-based alkali activated material
Si	Silicon
TGA	Thermogravimetric analysis
UV-Vis	Ultraviolet-Visible spectroscopy
XRD	X-ray powder diffraction
XRF	X-ray fluorescence
XPS	X-ray photoelectron spectroscopy

LIST OF FIGURES

LIST OF TABLES

1. INTRODUCTION

Concrete is a widely used material in construction industry due to its strength and durability [1]. Concrete is made up of cement, fine aggregate and coarse aggregate together with water in the optimal range. Even though it has many advantages as a construction material, one drawback of concrete is that the production of cement results in very high amounts of Greenhouse gas emissions and requires large volumes of raw materials. It has been estimated that production of one tone of cement requires about two tons of limestone and shale and results in the emission of one ton of CO_2 and nitrogen oxide [2]. About 2 billion tons of greenhouse gas is produced annually as a result of cement production activities and this makes up around 6% of the world's anthropogenic greenhouse gas emissions [3]. In 2050, it is expected that the global cement demand will be 6 billion tons [4]. Therefore, it will be of paramount importance to find alternative materials for a sustainable construction industry. One such material that can replace cement in the concrete is the alkali- activated materials, which results in geopolymer concrete [5]. Alkali activation is the generic term which describes the reaction of a solid aluminosilicate under alkaline conditions to produce a hardened binder [6]. Provis and Bernal describes alkali activated material as a material that is formed by the reaction of an aluminosilicate precursor and an alkali activator and a material that has similar properties to traditional cement binder. On the other hand, geopolymer can be considered as a subset of alkali activated materials and can be described as an alkali activated material that contains little or no calcium and that is frequently synthesized from metakaolin or fly ash precursors [7]. A schematic representation of synthesis is given in Figure 1.1.

The term “geopolymer” was first used by Davidovits [8]. Geopolymers can be described as cement-free binder materials that are formed by the reaction of silica and alumina-rich raw materials with alkaline activators [9]. Previous research has pointed out that the use of geopolymers in place of Portland cement can result in 80% reduction in embodied carbon [10].

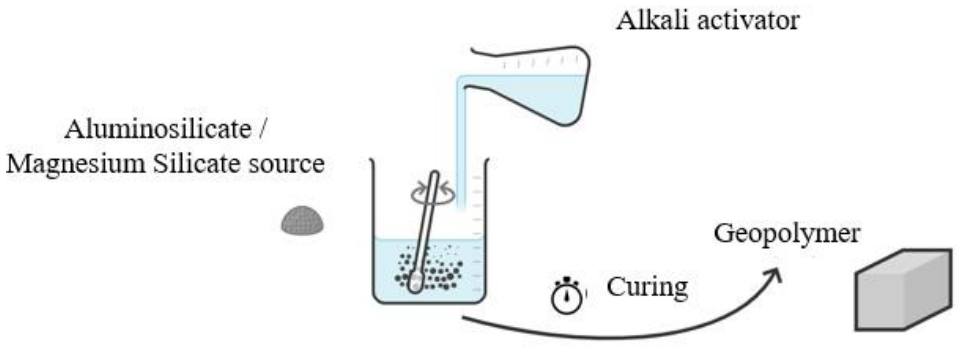

Figure 1.1. Schematic representation of geopolymer synthesis (Drawing created in Chemix).

In a recent life cycle assessment study, environmental impacts of blast furnace slag, fly ash and metakaolin- based alkali activated concretes were compared with Portland cement concrete [11]. The results of this study indicated that alkali activated concrete mixes can have between 57% and 39% lower global warming potential compared to Portland cement concrete. Among the alkali activated concrete mixes, blast furnace slag- based concrete was found as the best performer in terms of global warming potential reduction. They also found out that contrary to the previous studies, activators contribute between 13% to 33% to the CO_2 emissions depending on the mix design.

1.1. Geopolymerization Process

The geopolymer structure is generally formulated as $Mn[–(SiO_2)z–AlO_2–]n$ where M represents a charge balancing cation such as potassium or sodium, n is the degree of polycondensation degree and z is Si/Al molar ratio which is typically between 1 and 3 [8], [12]. During geopolymerization reactions, alumino-silicate oxides (Al^{+3} in 4-fold coordination) react with alkali polysilicates to give rise to Si-O-Al bonds. Amorphous to semi-crystalline silico- aluminate structures, such as Poly(sialate) type (–Si–O–Al–O–), Poly(sialate-siloxo) type (–Si–O–Al–O–Si–O–) and Poly(sialate-disiloxo) type (–Si–O–Al–O–Si–O–Si–O–), are obtained after the geopolymerization reactions [8].

Geopolymerization reactions takes place in three main stages. In the first stage, the dissolution of aluminosilicate materials in the alkali solution takes place to produce free silica and alumina tetrahedron. Following this, the gelation of materials, the condensation

reaction of alumina and silica hydroxyl to form the geopolymer gel phase takes place. Finally, as the gel phase hardens, it condenses to form a three-dimensional network that makes the geopolymer [13, 14].

Davidovits gives the reaction mechanism of geopolymer formation as in Figure 1.2 [8].

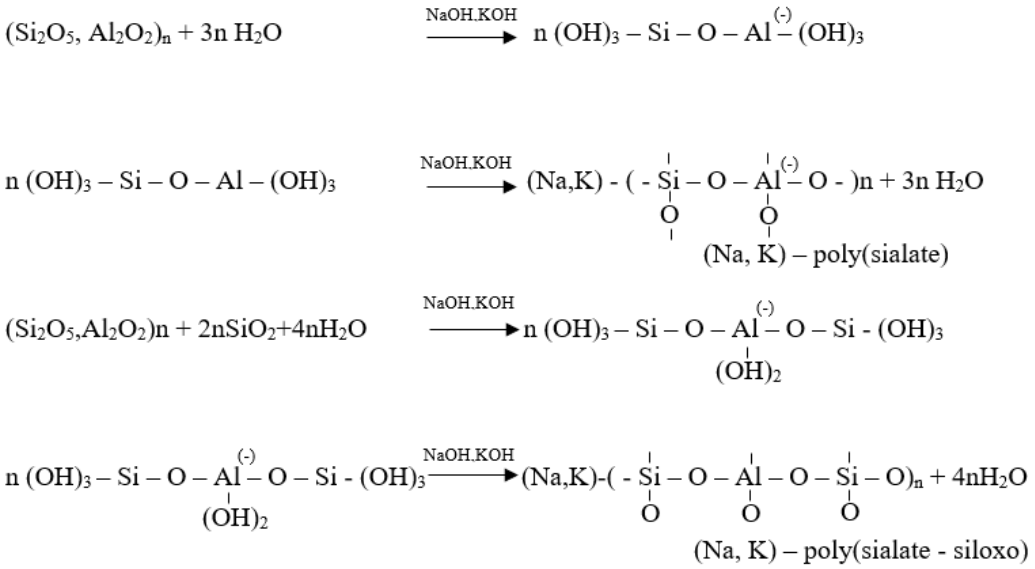

Figure 1.2. Reaction mechanism for geopolymer formation.

1.2. Raw Materials, Properties and Application Areas of Geopolymers (Alkali Activated Materials)

Geopolymers have a wide range of applications with construction being the most widely known and studied area [15]. The main property of the geopolymers to be investigated for construction applications is the compressive strength. Previous research shows that a number of parameters including, the type of aluminosilicate source and its composition, the type of activator and its concentration and the curing time have a strong effect on the compressive strength [15]. The main raw materials for the synthesis of geopolymers are fly ash, blast furnace slag and metakaolin.

Metakaolin is used as a raw material for geopolymer synthesis in many research studies due to its high purity compared to other aluminosilicate materials, which offers easier data interpretation. In their work, Duxson et al. investigated the effects of Si/Al ratio on the microstructure and compressive strength of metakaolin geopolymers. They observed through SEM investigations that the materials with Si/Al ratio < 1.4 were highly porous and the samples with Si/Al ratio > 1.65 were largely homogeneous. They observed the highest compressive strength at a Si/Al ratio of 1.90, beyond which the compressive strength decreased with increasing Si/Al ratio. They attributed this decrease to the amount of unreacted materials, which act as a defect [16]. In another study where the raw material for the geopolymerization was metakaolin, Ozer and Soyer-Uzun investigated the effects of Si/Al ratio on the compressive strength of metakaolin-based geopolymers in the range from 1.12 to 2.20. They characterized the samples by X-ray diffraction (XRD), Fourier-transform infrared (FTIR) and scanning electron microscope (SEM) to get an understanding of structure-performance relationship in the system. Their results indicated that the compressive strength value ranges between 13-23 MPa with the highest values obtained for a Si/Al ratio of 2.20 and lowest values obtained with a Si/Al ratio of 1.12. These results were correlated with the microstructures of the materials. For a Si/Al ratio of 1.12, the authors observed crystalline phases, which made them brittle, which resulted in a low compressive strength value [17]. In another study, Lahoti et al. investigated the effects of different mix design parameters, namely Si/Al molar ratio, water/solids mass ratio, Al/Na molar ratio and H_2O/Na_2O molar ratio on the compressive strength of metakaolin geopolymers through experiments and statistical analysis. Their results indicated that the most significant parameter on compressive strength is Si/Al molar ratio followed by Al/Na molar ratio. They also found that, unlike Portland cement, the water/solids mass ratio is not the chief factor on the compressive strength of metakaolin geopolymer [18]. The modelling study by Muracchioli et al. investigated the relationship between the compressive strength of metakaolin-based geopolymers and different processing conditions for both potassium and sodium based geopolymer systems through statistical analysis and experimental data. Their results indicated that curing time has a positive impact on compressive strength while increasing the curing temperature leads to a decrease in the compressive strength values. They observed a quadratic concave trend for the effects of SiO_2/Al_2O_3 ratio with compressive strength. An increase in the SiO_2/Al_2O_3 ratio resulted in an increase in the

compressive strength up to a certain value and above this value, further increase in SiO_2/Al_2O_3 led to a decrease in the mechanical properties [19].

Fly ash is a by-product of coal combustion from energy generation plants. The composition of the fly ash depends on a number of parameters such as the type of coal, operational conditions and the cooling control [20]. The amount of fly ash that is produced is increasing due to higher need for power production. The amount of fly ash produced annually is around 480 million tons globally [21]. This amount ends up in landfills or disposal ponds, which results in the leaching of heavy metals into the environment causing health hazards [22]. Because of this reason, the number of scientific studies that use of fly ash as a raw material for geopolymerization is increasing. The number of studies over the years is given given in Figure 1.3.

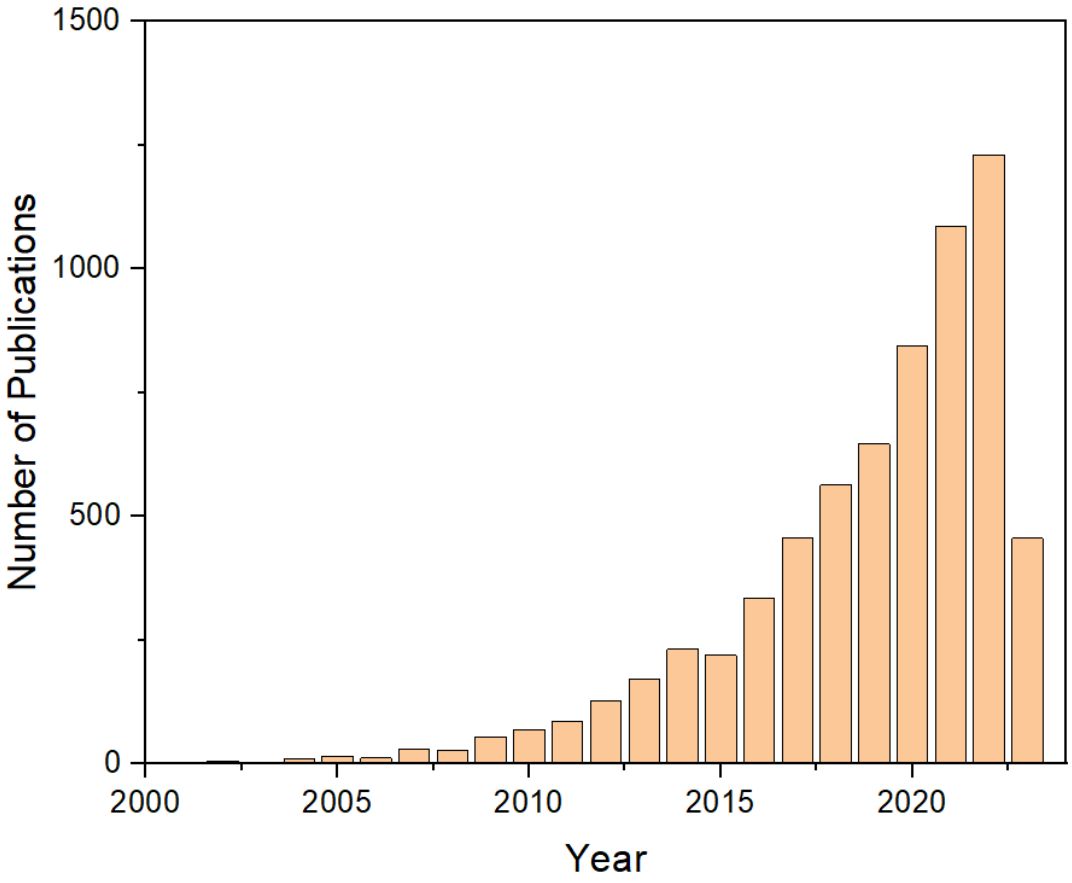

Figure 1.3. The number of publications with the keywords geopolymer and fly ash over the years (Source: Web of Science).

In their study, Fernandez- Jimenez and Palomo carried out a characterization study to investigate the potential of 5 different class F fly ash materials to be used as a raw material for alkali activation [23]. They used chemical analysis, laser granulometry, Blaine, Brunner-Emmett-Teller (BET) particle size distribution, XRD and ^{29}Si MAS NMR analysis for characterization and compressive strength as a measure of reactivity of the fly ashes as alkaline binders. Their results indicated that the reactive silica content, the vitreous phase and the particle size distribution are the main factor effecting the reactivity. In their work Ryu et al. investigated the effects of alkali activators on the compressive strength and microstructure of fly ash geopolymer mortar through SEM, EDX, XRD , FTIR and porosity assessments [24]. Their results indicated that chemical changes of the alkali activators had a significant effect on the early strength of the geopolymers. They observed compressive strength values as high as 47.5 MPa with a curing period of 91 days. Rees et al. studied the kinetics of geopolymer formation for a fly ash geopolymer using a novel in situ attenuated total reflectance Fourier-transform infrared (ATR-FTIR) technique [25]. They determined the reaction rates by monitoring the intensity of bands related to geopolymer gel and the unreacted fly ash particles. Their results indicated that an initial lag period takes place for hydroxide-activated geopolymers, which is followed by gel evolution. They also observed that the rate of network formation increases with increasing NaOH concentration up to a threshold value, beyond which the rate of network formation decreases. Hadi et al. examined the compressive strength of fly ash- based geopolymer mortar that is prepared from five different sources of fly ash [26]. They investigated the effects of the weight ratio of alkaline activator to fly ash content, the weight ratio of sodium silicate to sodium hydroxide and concentration of the NaOH. Their results indicated that the optimum value for the weight ratio of alkaline activator to fly ash content was in the range between 0.5-0.6. They also observed that fly ash samples that have a high amount of fine particles and amorphous components were activated with a low Na_2SiO_3/NaOH ratio and NaOH.

Blast furnace slag is produced as a by-product of smelting process where the oxides within the iron minerals are reduced and the impurities are separated [27]. Blast furnace slag is a widely used material in the synthesis of geopolymers. In their study, Aziz et al. investigated the strength development in ground granulated blast furnace slag geopolymers [28]. They obtained compressive strength values as high as 168.7 MPa after 28 days of curing. They found the optimum conditions for solid/liquid ratio and alkaline activator ratio

to be 3.0 and 2.5, respectively. In their study involving fly ash and ground granulated blast furnace slag as raw materials, Rao and Rao investigated the effects of alkaline activators of different molarities on the final setting time and compressive strength [29]. They observed that the compressive strength of the mortar increases with increasing percentage of ground granulated blast furnace slag into the fly ash- of ground granulated blast furnace slag system. Yurt used ground granulated blast furnace slag as the only binder in his study [30]. He investigated the effects of the molarity of the alkali solution and the activation temperature on the capillary water absorption, density, dynamic modulus of elasticity, compressive strength, splitting tensile strength, and abrasion resistance properties. The results indicated that alkali activated concrete can be synthesized by using ground granulated blast furnace slag as the only raw material. He obtained a high strength cementless concrete with a compressive strength value of 82.32 MPa.

There are also some studies that involve more than one material as the raw material for the synthesis of geopolymers. In their study, Kaya and Soyer- Uzun studied the structure-performance relationship in the red mud-metakaolin geopolymer system [31]. They investigated the effects of red mud addition to the system for the range from 0 to 40 % by XRD, FTIR, SEM and compressive strength measurements. They observed the highest compressive strength of 51.5 MPa with metakaolin geopolymer, while increasing red mud incorporation resulted in a decrease in the compressive strength values. Aouan et al studied the ternary system of kaolinite, metakaolin and fly ash as aluminosilicate sources [32]. They used augmented simplex- centroid design to prepare samples with different mixture proportions. They observed compressive strength values in the range 7.59 to 19.48 MPa. They used the validated cubic special model to evaluate the optimum mixture condition to be 75% fly ash and 25% metakaolin.

Although alumina and silica containing materials are considered as the raw materials for geopolymer synthesis, there are some studies which indicate that incorporation of MgO can enhance mechanical properties of the geopolymer binder. In their study, Yi et al. investigated the activating efficiency of MgO and compared with hydrated lime for ground granulated blast-furnace slag [33]. They investigated the obtained products by means of compressive strength, X-ray diffraction, scanning electron microscopy, Fourier transform infrared spectroscopy, energy dispersive X-ray and thermogravimetric analysis. Their results

indicated that reactive MgO acts as an effective activating agent and yields higher compressive strength compared to hydrated lime after 28 days of curing. In another study, Abdalqader et al. studied the effects of reactive MgO addition on an alkali activated fly ash/slag system [34]. They carried out compressive strength, X-ray diffraction, thermogravimetric analysis, infrared spectroscopy and scanning electron microscopy measurements for their investigations. In the light of their isothermal calorimetry results, they concluded that addition of reactive MgO results in an increased hydration rate while the strength and compositions of the samples varied with the introduction of MgO.

These studies are clear signs that Mg incorporation enhances the mechanical strength in building materials. Considering the fact that sepiolite is rich in Mg content (around 20% MgO), geopolymerization studies that start with sepiolite as the main raw material, looks very promising.

The number of geopolymerization studies that use sepiolite is very limited. The results of a web of science research with the keywords geopolymer, geopolymer and fly ash, geopolymer and metakaolin, geopolymer and furnace blast slag and geopolymer and sepiolite over the time period from 2000 to present is given in Figure 1.4.

An investigation of Figure 1.4 reveals that geopolymer technology is a widely studied topic with over 12.000 publications since the year 2000. The number of publications with aluminosilicate raw materials make up a large portion of these studies while the number of studies that use sepiolite is around 10.

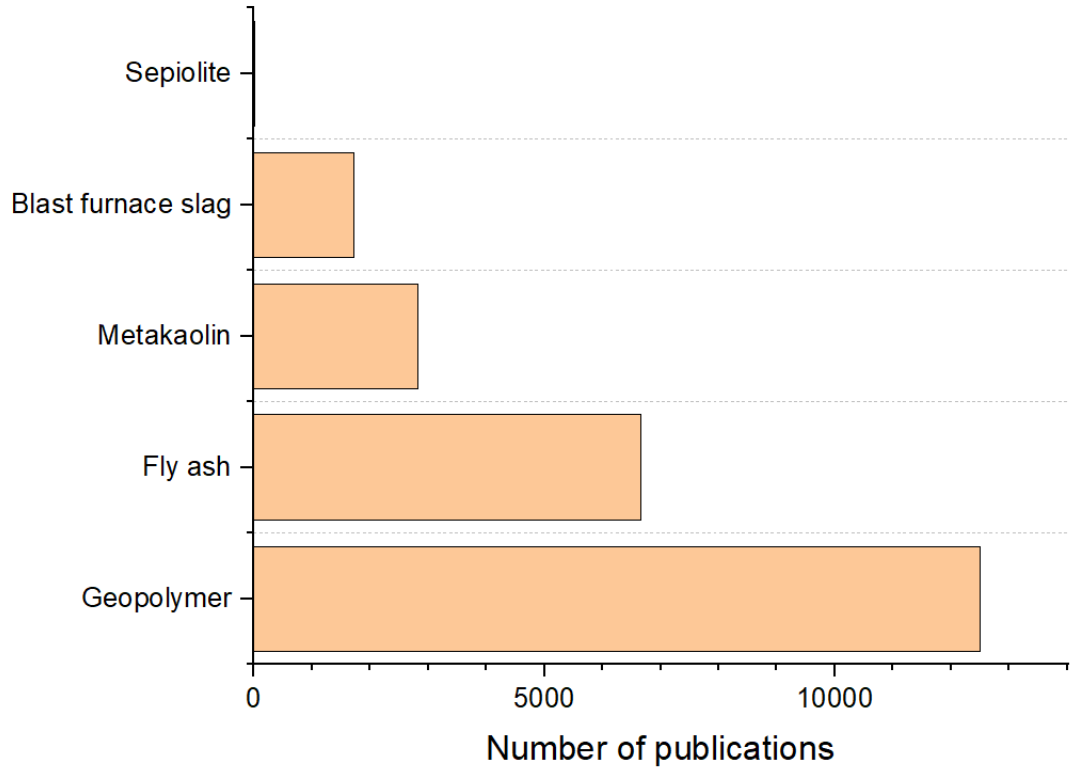

Figure 1.4. The results of a web of science research with the keywords geopolymer, geopolymer and fly ash, geopolymer and metakaolin, geopolymer and furnace blast slag and geopolymer and sepiolite over the time period from 2000 to present.

In their study, Wang et al. investigated the performance of admixture of sepiolite and fly ash modified cement mortar. Their results indicated that incorporation of sepiolite can greatly improve the strength of mortar at various curing periods. The highest compressive strength of 55 MPa is obtained with 30 % sepiolite addition and 56 days of curing time [35]. Kaya-Ozkiper et al. investigated the adsorption and mechanical strength of metakaolin and sepiolite based alkali activated monoliths for methylene blue removal. They observed the highest compressive strength of 37 MPa with the sample synthesized with 100 % sepiolite [36].

Although there are some studies on incorporation of sepiolite into AAM synthesis, the literature is limited for studies that use sepiolite as the main raw material of geopolymerization. A previous study from our group reported that a sepiolite-based magnesium silicate alkali activated (geopolymer-like) material offers potential as an effective adsorbent for methylene blue removal from aqueous solutions along with a high

mechanical strength, making these materials suitable candidates both for adsorption and construction materials [37]. However, this study was only for a single composition and a more in-depth analysis of different synthesis parameters on the mechanical strength and the relation between the mechanical strength and geopolymerization kinetics is required.

In addition to its mechanical properties, geopolymers have chemical and fire resistant properties, which make them suitable for a number of applications, such as fire- resistant coatings [38] and immobilization of hazardous and radioactive waste [39, 40]. One of the emerging area of application of geopolymers is adsorption and photocatalysis.

The results of a web of science search with the keywords geopolymer and adsorption is presented in Figure 1.5.

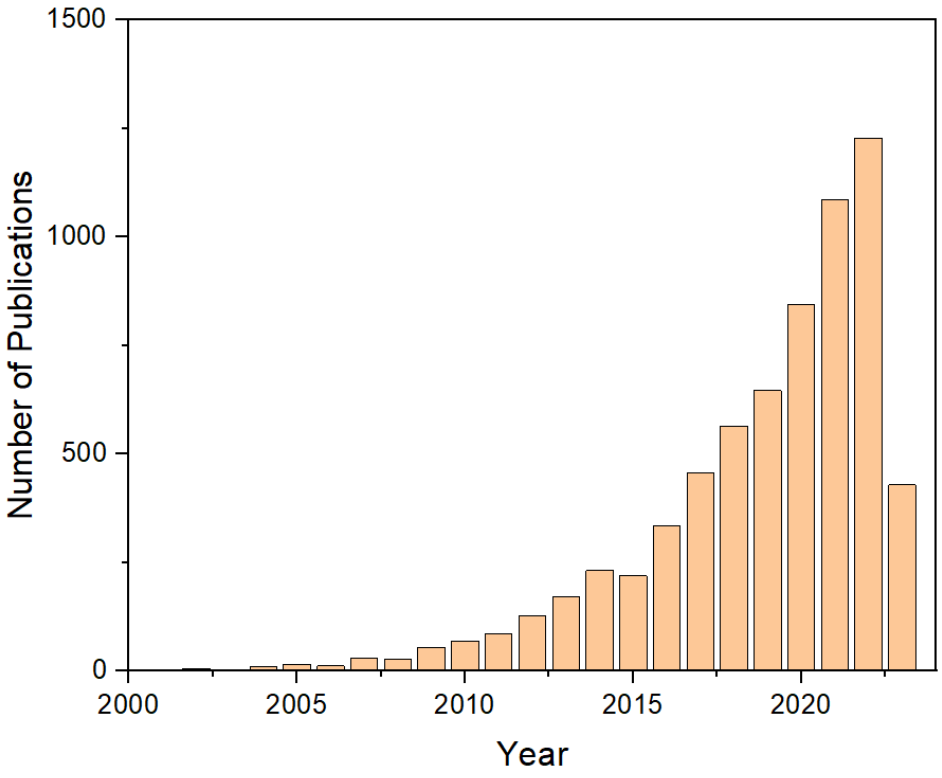

Figure 1.5. The results of a web of science search with the keywords geopolymer and adsorption over the years.

An investigation of Figure 1.5 reveals that research on the adsorption of materials by geopolymers has increased significantly over the last five years. It has been suggested in previous studies that geopolymers can be used as adsorbents for the treatment of wastewater due to their structure [41]. A good adsorbent should have properties such as high surface area, pore volume and suitable pore distribution [42]. As geopolymers have all these properties, they stand out as good candidates to be adsorbents. According the to the geopolymerization mechanism presented in Figure 1.2, geopolymers contain negatively charged surface hydroxyl groups, which make them suitable for the adsorption of cationic dyes [43].

In their study, Karuppaiyan et al. investigated the methylene blue removal performance of a metakaolin- based geopolymer coated with nano copper oxide on the surface. They studied the removal efficiency of the material in both powder and monolith forms. The results of their study revealed that introduction of nano copper particles enhanced the adsorption capacity in both monolith and powder forms, with the powder form having significantly higher adsorption capacity [44]. In another study, Fumba et al. studied the methylene orange removal capacity of kaolinite, metakaolin and activated geopolymer. They investigated the effects of different parameters such as contact time, pH, adsorbent dosage and initial dye concentration. Their results indicated that the equilibrium contact time is 15 minutes for kaolinite and geopolymer and 10 minutes for metakaolin. They observed the maximum adsorption capacity of 3.076 mg/g with metakaolin, which is followed by kaolinite and geopolymer with adsorption capacities of 1.247 and 0.3393 mg/g, respectively [45].

Li et al. investigated the effects of synthesis condition of fly ash geopolymers on the removal capacity of methylene blue and crystal violet. They found the optimal conditions to be 1.2:1 weight ratio of Na/fly ash at 250-350 ˚C fusion temperature. Their results indicated that the synthesized geopolymers have a much higher adsorption capacity compared to the fly ash that is used as the raw material for synthesis [43]. In their work, Novais et al. used fly ash- based geopolymer spheres for the first time to extract methylene blue from synthetic wastewater. They investigated the effects of sorption time, initial dye concentration and adsorbent amount on the dye removal efficiency and uptake by porous spheres. Their results indicated that a faster and higher methylene blue uptake compared to the literature was

possible with the materials of their study [46]. In another study by Novais et al., biomass fly ash geopolymer monoliths were used for the first time as adsorbents for the removal of methylene blue from synthetic wastewater. The maximum uptake was reported to be 15.4 mg/g, which was higher than several powdered adsorbents reported in literature. In addition to that, the material was stated to have the potential be used directly in packed beds as membranes, which is a major advantage compared to powdered adsorbents [47]. In another study with fly ash geopolymers, Kaewmee et al. synthesized geopolymeric cubes by potassium- activation at different silicate/hydroxide ratios. They obtained the highest methylene blue adsorption capacity to be 84 mg/g with a ratio of 0.3:1. They also concluded that incorporation of potassium into the aluminosilicate structure was the driving force for the adsorption of methylene blue [48].

As previously mentioned, geopolymers are more suitable for the removal of cationic species in wastewater due to their negative surface charge. However, although very few in number, there are some studies that focus on the removal of anionic dyes with geopolymers. One such study is done by Açıslı et al., where they applied a simple and low cost surface modification to a fly ash geopolymer for the removal of anionic Acid Blue 185 without the need for strongly acidic conditions. They investigated the effects of the surface modifier dosage, adsorbent dosage and the initial dye concentration and obtained the highest removal efficiency to be 98.19 % [49]. In another study, Siyal et al. worked on the optimization of synthesis parameters of fly ash- based geopolymers for the removal of anionic surfactant sodium dodecylbenzene sulfonate using response surface methodology. They investigated the effects of silica to alumina (Si/Al), sodium to alumina (Na/Al) and water to solids ratio on the adsorption properties of geopolymers. Their results indicated that the composition of Si/Al- 2.87, Na/Al- 1.0 and W/S- 0.35 displayed the highest adsorption capacity with a value of 743.706 mg/g [50].

In addition to the studies that use only one precursor for the synthesis of geopolymers, there are some studies that investigate the effects of using more than one precursor on the adsorption properties. Aouan et al. used a simplex- augmented- centroid mixture design to optimize the adsorptive properties of geopolymers by varying the content of the aluminosilicate precursors. The results of their studies indicated that the special cubic models they generated were significant and based on these models, the optimum content of the

geopolymer was determined to be 58 % metakaolin and 42 % kaolin [51]. In their study Kaya- Ozkiper et al. synthesized a family of sepiolite and metakaolin- based alkali activated monoliths for methylene blue adsorption. They observed a maximum adsorption capacity of 10.3 mg/g for sepiolite monoliths and 7.8 mg/g for metakaolin monoliths [52].

1.3. Sepiolite-Based Alkali Activated Materials

Geopolymer technology is gaining interest as described in Section 1.2. Easy synthesis with cheap and abundant materials is a major factor that can promote the use of geopolymers.

Sepiolite is a natural hydrous magnesium silicate material with the chemical formula $Si_{12}O_{30}Mg_8(OH)_4(H_2O)48H_2O$ [53]. Turkey is among the countries that have a significant amount of sepiolite reserves [54]. The structure of sepiolite is made up of a central sheet of magnesium oxide- hydroxide that lies in between two tetrahedral silica sheets.

Because of its high surface area and unique structure sepiolite is known for its adsorptive properties. In one study, Dogan et al. investigated the rate of adsorption under various parameters, such as contact time, stirring speed, ionic strength, pH and temperature for the removal of methyl violet and methylene blue. Their results indicated that the adsorption rate of dyes on sepiolite increased with increase in initial dye concentration, ionic strength, pH and temperature but stirring speed had no effect on the adsorption rate [55]. In a more recent study, Largo et al. studied the potential of sepiolite as an adsorbent for the removal of cationic (methylene blue) and anionic (Direct Red-23) dyes from aqueous solution. They investigated the effects of adsorbent amount, the contact time, pH, ionic strength and initial dye amount. They obtained the maximum amount of adsorbed dye to be 124.9 and 649.37 mg/g for methylene blue and Direct Red-23, respectively [56].

In order for the adsorbent material to be applicable, it is very important that it has the necessary mechanical strength so that it will not cause any problems in the industrial units [57]. Although sepiolite has very good adsorption properties, it provides very little mechanical strength, which decreases the possibility of its use in the industry. Sepiolite-based geopolymers were first introduced by Mackenzie et al., where they experimentally showed by NMR studies that sepiolite-based geopolymers closely resembled an

aluminosilicate geopolymer and some of the Mg in the system was located in tetrahedral sites [58]. A previous study in our research group introduced a sepiolite geopolymer with high methylene blue adsorption capacity and high mechanical strength. They observed a removal capacity of 99.92 mg/g and compressive strength values of 40 MPa and concluded that concluded that these innovative materials offer high potential for wastewater treatment [37]. This study was based on one synthesis condition only. However, different applications might require different adsorption and mechanical characteristics. Therefore, a more in-depth analysis of different synthesis parameters on the mechanical strength and adsorption properties is required.

1.4. Methodology

1.4.1. Experimental Design and Data Analysis

The experimental design was carried out as 2^3 central composite design (CCD). The reason for choosing this design was that, it can be run sequentially, meaning that the design can be divided into two subsets, the first to estimate linear and two- factor effects and the second to estimate curvature effects [43]. CCD is efficient that allows a lot of information about the variables to be gained in a small number of experiments. The three parameters of interest are chosen as the molar Na/Mg ratio, pretreatment temperature of the raw material (T) and molar Si/Mg ratio. The synthesis parameters are then correlated with the mechanical strength measurements and methylene blue adsorption capacity to synthesize the geopolymers with optimum mechanical strength and adsorption properties.

A predictive model was built for the estimation of methylene blue adsorption capacities of the synthesized materials. The generated model was of the form:

$$Y = a_0 + a_1A + a_2B + a_3C + a_{12}AB + a_{13}AC + a_{14}BC + a_{11}A^2 + a_{22}B^2 + a_{33}C^2, \quad (1.1)$$

where Y is adsorption capacity(mg/g), a_o is constant coefficient, a_i, a_{ii}, and a_{ij} are linear, quadratic and interaction coefficients, A, B and C are molar Na/Mg ratio, sepiolite treatment temperature and molar Si/Mg ratio, respectively.

The significance of the model was validated by means of an ANOVA analysis. The alpha value was taken to be 0.05. Backward elimination was used for the generation of the model. By using backward elimination, the least significant term, the term with the highest p-value, is removed from the model and the statistical analysis is repeated until all the terms are significant.

1.4.2. Geopolymer Synthesis

The first step in the geopolymer synthesis was the treatment of sepiolite at the given temperatures (500 – 1000 °C) for 1 hour to activate the raw material. After pretreatment and cooling, required amounts of sodium hydroxide and sodium silicate were mixed with the activated sepiolite to obtain the desired compositions.

After mixing, the samples were stored for ex-situ ATR-FTIR measurements. In addition to that, geopolymer samples were poured into 1 cm x 1 cm x 1 cm cells and were cured for 6 weeks for compressive strength measurements.

1.4.3. ATR-FTIR Data Collection

ATR-FTIR is used to understand the kinetics of sepiolite-based geopolymers. Throughout the geopolymerization reactions, different phases, including unreacted particles, partially reacted particles, newly formed aluminasilicate gel, liberated aluminasilicate etc., are present in the system. In order to investigate the geopolymerization reactions, a method which can simultaneously analyze all these phases and which will not disrupt the balance between these materials, is required. ATR-FTIR stands out as a very good candidate to carry out these studies [59].

FTIR spectroscopy can be used to obtain information about different types of bonds in a material along with ordering and network arrangement. ATR-FTIR makes it possible to obtain data without destructive sample preparation, which makes it very useful for studying different phases that are present in the geopolymerization reaction [59]. In fact, there are

several studies in literature that make use of FTIR spectroscopy to monitor the reactions taking place during geopolymerization reactions.

Hajimohammadi and van Deventer investigated the kinetics of one-part geopolymerization using fly ash as the starting raw material. In their FTIR investigations, they observed that the position of the main feature shifts to a lower wavenumber and then increases to a certain level and stays constant throughout. This observation, along with the data in the literature suggests that a two- stage gel formation takes place during geopolymerization reaction of fly ash [60]. In another study, Reese et al., investigated the effects of sodium hydroxide and silicate concentrations on structural changes of fly ash geopolymer using attenuated total reflectance Fourier transform infrared (ATR-FTIR) spectroscopy over 200 days. Their results indicated that there is strong correlation between silicate concentration in the activating solution and the position of main Si–O–T (T: Al or Si) stretching band. Furthermore, they observed that use of high order silicate in activating solution results in rapid formation of a steady gel composition before obtaining an Al-rich gel first [59].

The FTIR spectroscopy of the samples were collected using a Perkin Elmer Frontier FT-IR Spectrometer. Absorbance spectra was collected in the range from 4000-650 cm^{-1} at a resolution of 2 cm^{-1} and a scanning speed of 5 kHz with 16 scans. For the kinetics studies, FTIR data was collected for all the samples on an hourly basis in the early geopolymerization, and on the order of days afterwards for a 30-day period.

1.4.4. Compressive Strength Measurements

Compressive strength measurements were conducted on an MTS model servo-hydraulic test machine with capacity of 500 kN with a loading rate of 0.01 mm per second. After synthesis, the geopolymer samples were poured into 1 cm × 1 cm × 1 cm silicon molds and kept at room temperature for 6 weeks before compressive strength measurements. An image of the 1 cm × 1 cm × 1 cm cubes that are synthesize are presented in Figure 1.6.

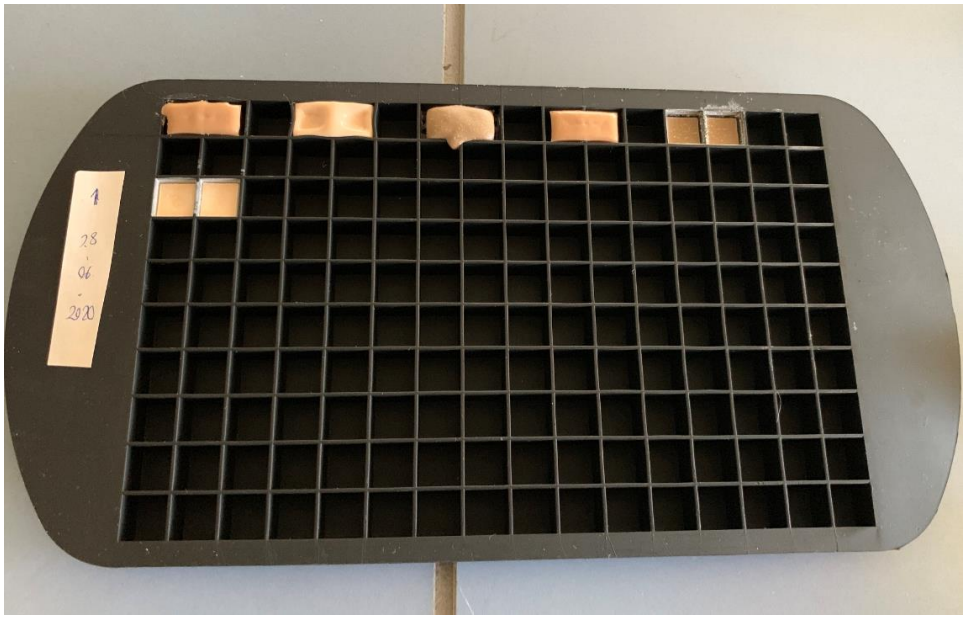

Figure 1.6. An image of the 1x1x1 cm cubes.

1.4.5. Structural Characterization

The structure of the raw materials and the synthesized geopolymers were characterized in detail by a number of methods including X-ray fluorescence (XRF) spectroscopy, X-ray diffraction (XRD) spectroscopy, X-ray photoelectron spectroscopy (XPS), Brunauer Emmett Teller (BET surface) area analysis and thermogravimetric analysis (TGA). XRF analysis was used to determine the chemical composition of the raw materials. The composition data is then used to synthesize the geopolymer samples with the desired composition. XRD was used to investigate the crystal structure and amorphous character of the samples. XRD was also used for investigating the changes in the crystal structure upon geopolymerization reactions. XPS analysis was performed to get an understanding of the surface chemistry, composition and binding state of the atoms. BET analysis was used to determine the surface area of the samples, along with pore volume and pore size information. TGA was used to determine the thermal stability of the materials. The parameters and conditions of these characterization techniques are thoroughly presented in the relevant parts of this thesis.

1.4.6. Methylene Blue Adsorption Tests

For the measurement of the methylene blue removal of the synthesized materials, firstly a methylene blue solution of known concentration is prepared. Then, a measured amount of adsorbent is immersed into the solution and is mixed at constant speed until equilibrium was reached. The mixing was done at room temperature and atmospheric pressure. A snapshot of the mixing process is given in Figure 1.7.

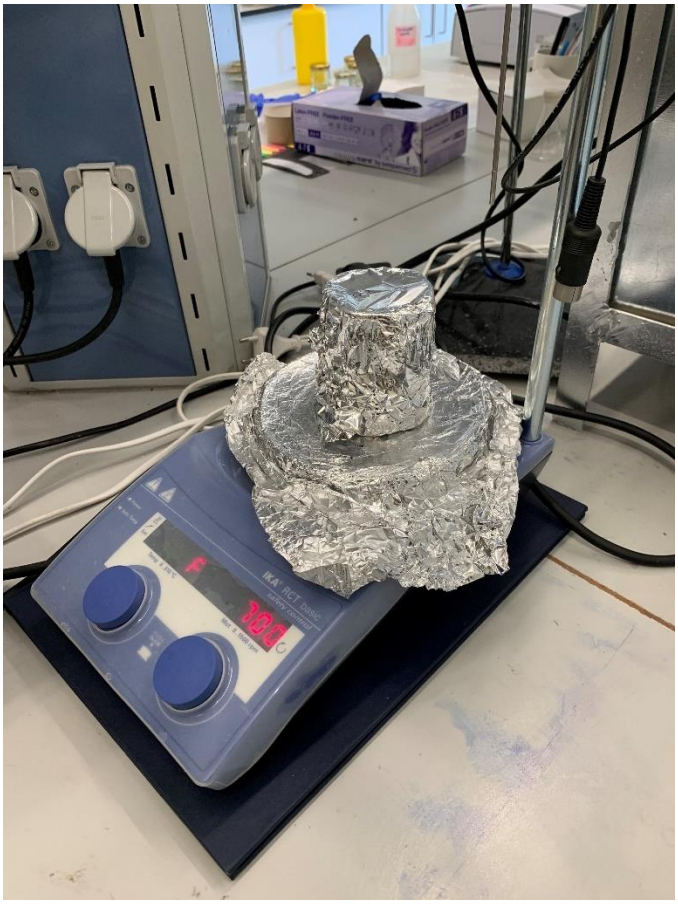

Figure 1.7. Mixing process before the methylene blue adsorption tests.

Aliquots were collected from the methylene blue solutions and analyzed with a Flame-S-UV-Vis-ES spectrometer (Ocean Optics, USA) by measuring the absorbance value at λ = 664 nm. Removal efficiency (%) was measured as stated in the following equation:

$$Removal\ efficiency\ (\%) = \frac{C_o - C_t}{C_o}\ x\ 100 = \frac{A_o - A_t}{A_o}\ x\ 100, \quad (1.2)$$

where C_0 and C_t are the concentration of MB solution at initial time t = 0 and at time t, respectively. A0 and At denote to absorbance values at initial time t = 0 and at time t, respectively [61]. The amount of MB adsorbed on adsorbents were determined by:

$$q_e = \left(\frac{C_o - C_e}{m}\right) x\ V, \quad (1.3)$$

where q_e is the amount of MB dye uptake by the adsorbent (mg MB dye/g adsorbent), m is the mass of the adsorbent (g), and V is the volume of the MB solution (L).

During the course of the mixing, methylene blue is adsorbed by the adsorbent and a change in the color of the solution takes place. An image displaying the change before and at the end of the equilibrium time is presented in Figure 1.8.

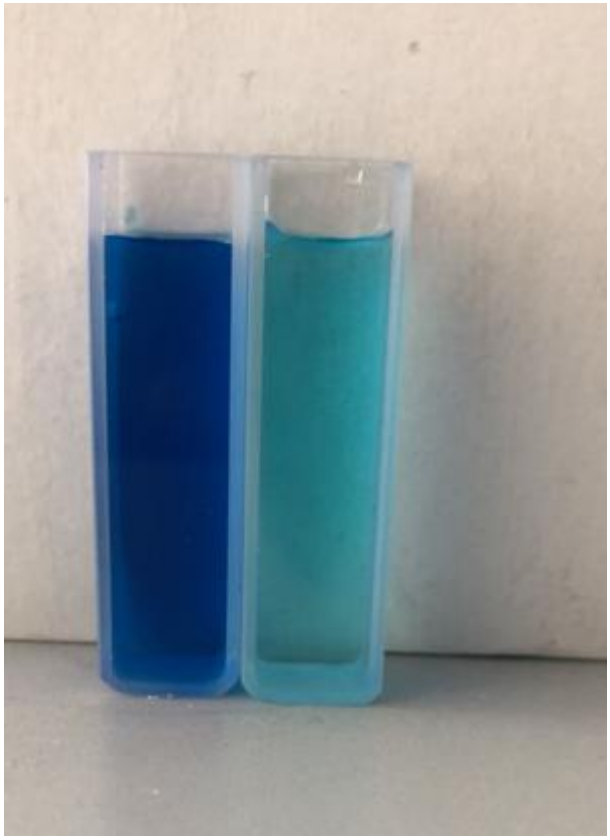

Figure 1.8. The change in the color before and at the end of equilibrium time.

1.5. Aim and Scope of This Work

The main goal of this thesis study is to understand the effect of the synthesis conditions and the formation kinetics on the mechanical performance and methylene blue adsorption characteristics in SAAM systems.

Alkali- activated aluminosilicate geopolymers are widely studied in the literature and the composition that maximizes the mechanical strength is mainly known ($NaAlSi_2O_6.5.5H_2O$) [62]. However, as mentioned earlier, the number of studies that uses sepiolite as the raw material in alkali-activation is very limited and the optimum composition that maximizes mechanical strength is unknown. Although it was reported by MacKenzie et al. that magnesium silicate anologs of aluminosilicate geopolymers can be synthesized and Mg sites seem to behave like Al and they are in tetrahedral coordination [58], there are no studies focusing on the relationships between the synthesis condition and compressive strength in these systems. Geopolymerization is a time-dependent process where structure and properties vary. Kinetics of sepiolite geopolymerization and its effect on mechanical properties are also important points to be addressed. In addition to the mechanical strength considerations, a recent study has shown that sepiolite geopolymers demonstrate high potential as an adsorbent [37]. However, this study was based on one synthesis condition only. Considering the fact that different applications might require different adsorption and mechanical characteristics, an in-depth analysis of different synthesis parameters on the mechanical strength and adsorption is also carried out as part of this thesis.

In Chapter 2 of this thesis, the effects of synthesis parameters on the mechanical strength of sepiolite-based geopolymers were studied by an experimental design. The reaction kinetics of the sepiolite-based geopolymers were studied by ATR-FTIR data collection at different reaction times for the first time in literature. The mechanical strength data was analyzed along with the kinetic data and the relations were quantified. All of the synthesized materials were characterized by a number of characterization tools including XRF, XRD, TGA, XPS and the results were used to explain the way the materials behave. The results of Chapter 2 are being prepared for publication.

In Chapter 3 of this thesis, the effects of synthesis parameters on the methylene blue adsorption characteristics in sepiolite- based alkali-activated materials are studied by experimental design. The adsorption data was analyzed by statistical tools and a response surface model was built based on the experimental data. The results are analyzed in combination with the mechanical properties presented in Chapter 2. The results are being prepared for publication.

The results of this thesis point out that synthesis parameters and formation kinetics have significant impacts on the mechanical strength and adsorption properties of magnesium silicate alkali activated materials and these materials have huge potential in construction and wastewater treatment applications as environmentally friendly and sustainable options.

2. EFFECTS OF SYNTHESIS PARAMETERS ON THE KINETICS AND MECHANICAL STRENGTH OF SEPIOLITE BASED ALKALI ACTIVATED MATERIALS

2.1. Introduction

The risks related to climate change are increasing which is evident with the fact that the last five years have been the warmest on record [63]. CO_2 emissions are one of the major contributors to global warming. Cement industry is one of the largest CO_2 emitting industries and is responsible for 7-8% of all anthropogenic CO_2 emissions [64]. It is the third largest industry to produce difficult-to-eliminate emissions after load-following electricity and iron and steel [65]. Production of cement is an energy-intensive process and CO_2 emissions per ton of cement range between 800 -1000 kg [66]. Several approaches can be taken to reduce the CO_2 emissions originating from cement industry, such as replacing the cement by secondary raw materials and secondary cementitious materials and using alternative fuels in cement production [67]. Geopolymers, or alkali activated materials (AAM) in a broader context, stand out as a promising alternative to cement as a construction material [17], [31], [68].

Alkali activation is the term to describe the reaction of a solid aluminosilicate (precursor) under alkaline conditions to produce a hardened binder [6]. Commonly used cementitious materials, such as blast furnace slag, fly ash, calcined clays and pozzolans, are suitable to be used as the precursor for the synthesis of AAMs [7] and the success with several raw materials were shown in previous studies [69-71].

The literature is rich for the synthesis of AAMs with raw materials containing alumina and silica but is more limited for other raw materials, such as those containing magnesium and silicate. There are some studies that investigate the effects of MgO content on alkali-activated slag geopolymers. In their study, Yi et al. investigated the activating efficiency of MgO and compared with hydrated lime for ground granulated blast-furnace slag. They investigated the obtained products by means of compressive strength, X-ray diffraction,

scanning electron microscopy, Fourier transform infrared spectroscopy, energy dispersive X-ray and thermogravimetric analysis. Their results indicated that reactive MgO acts as an effective activating agent and yields higher compressive strength compared to hydrated lime after 28 days of curing [33]. In another study, Abdalqader et al., studied the effects of reactive MgO addition on an alkali activated fly ash/slag system. They carried out compressive strength, X-ray diffraction, thermogravimetric analysis, infrared spectroscopy and scanning electron microscopy measurements for their investigations. In the light of their isothermal calorimetry results, they concluded that addition of reactive MgO results in an increased hydration rate while the strength and compositions of the samples varied with the introduction of MgO [34]. In another study, Haha et al., studied the effects of MgO on hydration and microstructure of alkali activated slags. They investigated the effects of MgO on the interval 8-13 wt. % in presence of two different alkaline activators, NaOH and $Na_2SiO_3 \cdot 5H_2O$ (WG). Their results indicated that, increasing the MgO content yields higher compressive strength and faster reaction in the firsts days. They also concluded that increasing the MgO content in presence of WG resulted in 50-80% increase in compressive strength after 28 days of curing [72]. Jin et al., also investigated the effects of two different commercial reactive MgO's on the hydration of ground granulated blast furnace slag. They studied in the range 2.5- 20 wt.% for up to 90 days. They carried out selective dissolution, thermogravimetric analysis, X-ray diffraction and scanning electron microscopy for their investigations. Their results indicated that increasing amounts of MgO resulted in improved compressive strength and based on compressive strength measurements, MgO is a better activator compared to hydrated lime [73].

These studies are clear signs that Mg incorporation enhances the mechanical strength in building materials. As a result of these positive findings, the number of studies that make use of raw materials containing magnesium and silica, such as sepiolite, is increasing in the recent years. Sepiolite is a natural hydrous magnesium silicate material with the chemical formula $Si_{12}O_{30}Mg_8(OH)_4(H_2O)48H_2O$ [53]. Sepiolite is a widespread and abundant material. Spain is the world's largest sepiolite producer and 90% of the sepiolite in Europe comes from Spain with the remaining sepiolite mainly coming from Turkey [74]. Sepiolite is used in a wide range of areas including catalyst support and ion adsorption [75-77] due to its large surface area and unique structure. Despite the research in different areas, the

literature for the use of sepiolite as a raw material in the synthesis of AAMs for construction purposes is still limited.

In their study, Wang et al. investigated the influence of binary admixture of sepiolite and fly ash on the performance of modified cement mortar. Their results indicated that incorporation of sepiolite can greatly improve the strength of mortar at various curing periods [35]. Kaya-Ozkiper et al. investigated the adsorption and mechanical strength of metakaolin and sepiolite-based alkali activated monoliths for methylene blue removal. They observed compressive strength values as high as 37 MPa [52]. In another study, Pu et al. investigated the effects of sepiolite addition on compressive strength, flexural strength and microstructure to a fly ash-metakaolin geopolymer activated by sodium silicate and sodium hydroxide solutions. Their results indicated that addition of sepiolite up to 10% resulted in an increase in compressive strength after 7 days of curing and an increase in flexural strength regardless of days of curing [78]. Yan et al. investigated the effects of sepiolite addition compressive strength, flexural strength, surface abrasion resistance, Vickers-hardness of surface and microstructure evolution of fly ash-metakaolin geopolymer. They observed that the optimum amount of sepiolite addition is 10% for obtaining high compressive and flexural strength [79].

Although there are some studies on incorporation of sepiolite into AAM synthesis, the literature is limited for studies that use sepiolite as the main raw material of geopolymerization. In their work, MacKenzie et al. attempted to synthesize magnesium-containing analogues of aluminosilicate geopolymers [58]. They studied the effects of pretreatment, ie, grinding, dehydroxylation, by means of XRD, ^{29}Si and natural-abundance ^{25}Mg solid-state magic angle spinning (MAS) NMR spectroscopy measurements. Their results indicated that, the products that are formed by using sepiolite as the raw material results in structures similar to aluminosilicate geopolymers. A previous study from our group reported that a sepiolite-based magnesium silicate alkali activated (geopolymer-like) material offers potential as an effective adsorbent for methylene blue removal from aqueous solutions along with a high mechanical strength, making these materials suitable candidates both for adsorption and construction materials. However, this study was only for a single composition and a more in-depth analysis of different synthesis parameters on the

mechanical strength and the relation between the mechanical strength and geopolymerization kinetics is required.

Motivated from the potential of sepiolite-based alkali-activated materials, an experimental design is used to investigate the effects of different synthesis parameters on the compressive strength of these materials (SAAM) for the first time. The raw materials and the SAAMs are characterized by XRF for their chemical composition, XRD for an investigation of the crystalline phases, TGA for their thermal stabilities and XPS for their surface characteristics. ATR-FTIR data is collected at different reaction times to shed light on the relation between the geopolymerization kinetics and the compressive strength. The results of this chapter are being prepared for publication.

2.2. Materials and Methods

2.2.1. Sample Preparation

Sepiolite was kindly supplied by Dolsan Mining, Eskişehir, Turkey. Sepiolite is treated at 5 different temperatures for 1 h. Activating solution is prepared by mixing sodium silicate ($Na_2Si_3O_7$) solution (%9 of Na_2O, 28% of SiO_2 and 63% of H_2O; density: 1.401g/ml at 20 °C) and sodium hydroxide (NaOH) pellets. The amount used for each material is given in Table 2.1.

Sepiolite is calcined at 500, 600, 750, 900 and 1000 °C. Powdered and sieved (#70 mesh sieve, 200 μm) calcined sepiolite is mixed thoroughly with necessary amount of activating solution to obtain desired Si/Mg and Na/Mg ratios. The mixture is then left to curing at room conditions for 6 weeks for compressive strength measurements.

Geopolymers were synthesized with aluminosilicate precursors for a comparison of early stage geopolymerization in aluminosilicate and magnesium silicate systems. For this purpose, MK Imerys Metastar™ 501 was used as the metakaolin raw material and F-type fly ash was obtained from a power plant in Adana region.

Table 2.1. Amounts of raw materials used for geopolymer synthesis.

	Molar Na/Mg ratio	**Temperature (°C)**	**Molar Si/Mg ratio**	**Sepiolite (g)**	**Sodium Silicate (g)**	**Sodium Hydroxide (g)**
SAAM-1	1.3	750	2.5	12	26.8	1.9
SAAM-2	1.5	900	3	12	36.9	1.6
SAAM-3	1.1	600	3	12	36.9	0.2
SAAM-4	1.3	750	2.5	12	26.8	1.9
SAAM-5	1.5	600	2	12	16.8	3.7
SAAM-6	1.1	900	2	12	16.8	2.3
SAAM-7	1.1	600	2	12	16.8	2.3
SAAM-8	1.3	750	2.5	12	26.8	1.9
SAAM-9	1.5	600	3	12	36.9	1.6
SAAM-10	1.1	900	3	12	36.9	0.2
SAAM-11	1.5	900	2	12	16.8	3.7
SAAM-12	1.3	750	2.5	12	26.8	1.9
SAAM-13	1.3	750	3.3	12	42.9	0.3
SAAM-14	1.3	750	2.5	12	26.8	1.9
SAAM-15	1	750	2.5	12	26.8	0.9
SAAM-16	1.3	500	2.5	12	26.8	1.9
SAAM-17	1.3	750	1.7	12	10.7	3.6
SAAM-18	1.6	750	2.5	12	26.8	3
SAAM-19	1.3	750	2.5	12	26.8	1.9
SAAM-20	1.3	1000	2.5	12	26.8	1.9

2.2.2. Experimental Design and Statistical Analysis

The experimental design is carried out as 2^3 Central Composite Design (CCD). CCD design offers the advantage of running sequentially, meaning that the design can be divided into two subsets, the first to estimate linear and two- factor effects and the second to estimate curvature effects [80]. In addition to that, CCD is efficient that allows a lot of information about the variables to be gained in a small number of experiments. The three parameters of

interest are chosen as the pretreatment temperature of the raw material sepiolite (T), molar Si/Mg ratio and molar Na/Mg ratio. The synthesis conditions for the experimental design are given in Table 2.2.

The effects of different parameters on the compressive strength is investigated by means of statistical analysis. For this purpose, a model of the following form is generated

$$Y=a_0+a_1A+a_2B+a_3C+a_{12}AB+a_{13}AC+a_{14}BC+a_{11}A^2+a_{22}B^2+a_{33}C^2, \quad (2.1)$$

where Y is compressive strength (MPa), a_o is constant coefficient, a_i, a_{ii}, and a_{ij} are linear, quadratic and interaction coefficients, A, B and C are molar Na/Mg ratio, sepiolite treatment temperature and molar Si/Mg ratio, respectively.

Table 2.2. Synthesis conditions for the experimental design.

Sample name	Molar Na/Mg ratio	Temperature (°C)	Molar Si/Mg ratio
SAAM-1	1.3	750	2.5
SAAM-2	1.5	900	3.0
SAAM-3	1.1	600	3.0
SAAM-4	1.3	750	2.5
SAAM-5	1.5	600	2.0
SAAM-6	1.1	900	2.0
SAAM-7	1.1	600	2.0
SAAM-8	1.3	750	2.5
SAAM-9	1.5	600	3.0
SAAM-10	1.1	900	3.0
SAAM-11	1.5	900	2.0
SAAM-12	1.3	750	2.5
SAAM-13	1.3	750	3.3
SAAM-14	1.3	750	2.5
SAAM-15	1.0	750	2.5
SAAM-16	1.3	500	2.5
SAAM-17	1.3	750	1.7
SAAM-18	1.6	750	2.5
SAAM-19	1.3	750	2.5
SAAM-20	1.3	1000	2.5

2.2.3. Structural Characterization

The chemical compositions of raw and calcined sepiolite were determined using X-ray fluorescence (Bruker S8 Tiger). X-ray diffraction (XRD) measurement of the samples were performed on a Bruker D8 Advance Diffraction system with a Cu Kα1 radiation source. XRD data was collected 3 months after the samples were synthesized. The data were recorded in the range 2θ = 10–80°. The FTIR spectroscopy of the samples were collected using a Perkin Elmer Frontier FT-IR Spectrometer. Absorbance spectra was collected in the range from 4000-650 cm^{-1} at a resolution of 2 cm^{-1} and a scanning speed of 5 kHz with 16 scans. For the kinetics studies, FTIR data was collected for all the samples on an hourly basis in the early geopolymerization, and on the order of days afterwards for a 30-day period. X-ray photoelectron spectroscopy (XPS) analysis was conducted on a Thermo Scientific K-Alpha X-ray Photoelectron Spectrometer and Avantage 5.9 software was utilized for XPS data fitting. Thermogravimetric analysis (TGA) was conducted on a Perkin Elmer TGA 4000 instrument. The analysis was done in a temperature range from 25 to 900 °C at a heating rate of 10 °C/min for raw sepiolite, calcined samples and the geopolymer samples under N2 flow. Compressive strength measurements were conducted on a MTS model servo-hydraulic test machine with capacity of 500 kN with a loading rate of 0.01 mm per second. After synthesis, the geopolymer samples were poured into 1 cm × 1 cm × 1 cm silicon molds and kept at room temperature for 6 weeks before compressive strength measurements.

2.3. Results

2.3.1. Structural Characterization of Raw Materials

The XRD patterns for as-received sepiolite along with sepiolite calcined at 600, 750 and 900 °C are given in Figure 2.1. Main crystalline phases observed in as-received sepiolite are observed to be sepiolite and dolomite along with minor contributions from quartz. Upon calcination at 600 °C, formation of a new feature is observed, which is attributed to calcite. This feature represents the first step of calcinations of the dolomite to give calcite [81]. Some structural changes take place after further heating to 750 °C. The peaks related to dolomite and sepiolite completely disappear and some new features related to calcium magnesium

silicate and periclase are observed. New peaks are formed after heating the sample to 900 °C, suggesting the formation of enstatite as a new crystalline phase [81, 82].

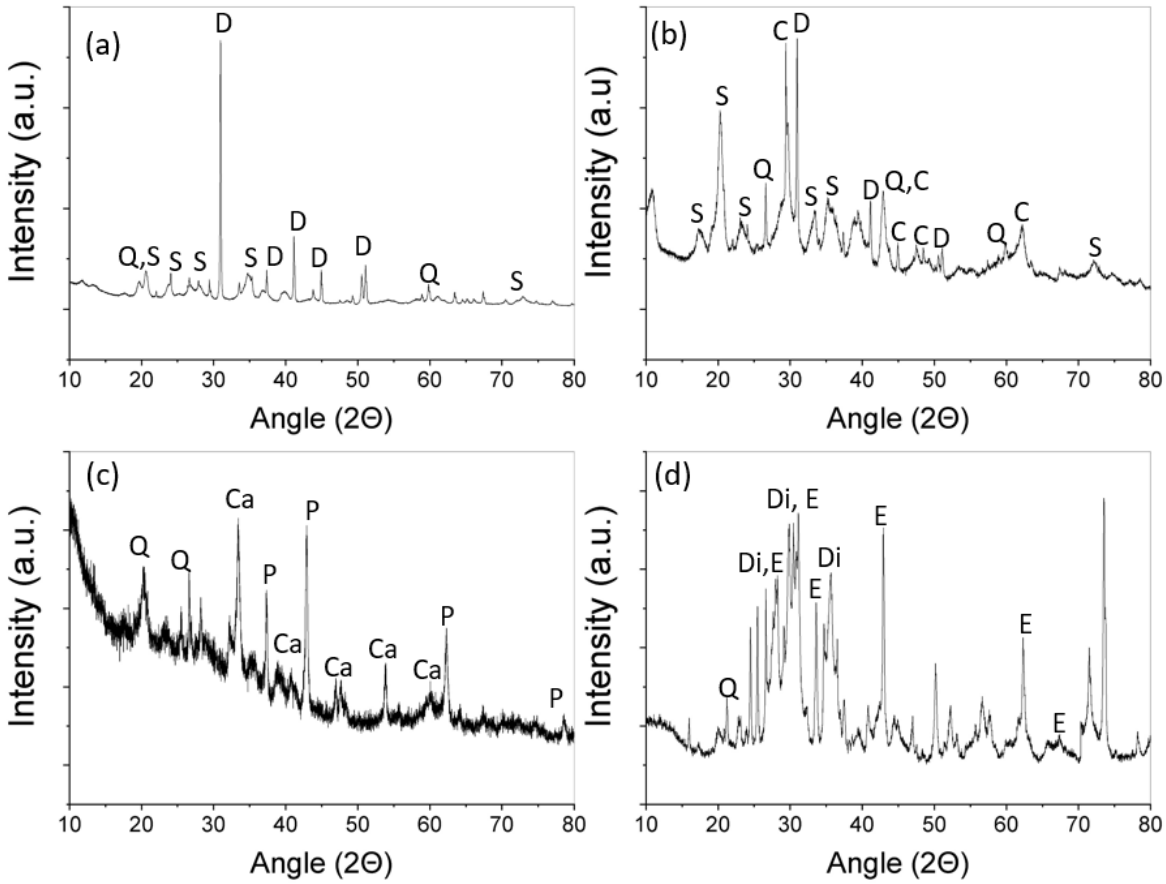

Figure 2.1. XRD Patterns of (a) sepiolite and calcined sepiolite samples at (b) 600 °C, (c) 750 °C and (d) 900 °C (D: Dolomite, S: Sepiolite, Q: Quartz, C: Calcite, Ca: Calcium Magnesium Silicate, P: Periclase, Di: Diopside, E: Enstatite).

The FTIR spectra of raw sepiolite and calcined sepiolite at 600 °C, 750 °C, and 900 °C are given in Figure 2.2 FTIR spectrum of raw sepiolite displays features at 3690, 3620, 3560, 3370 and 3240 cm^{-1}, which are associated with the presence of water molecules. The band at 3690 cm^{-1} is assigned to hydroxyl stretching vibrations of MgOH groups [83, 84]. The features at 3620 and 3560 cm^{-1} are assigned to vibrations associated with water coordinated to magnesium ions at the edge of structural blocks while the features at 3370, 3240 and 1640 cm^{-1} are related to the presence of zeolitic water [84], The feature located at 1456 cm^{-1} is associated with the stretching vibration of C–O indicating the presence carbonate groups [81], [85]. The feature at 882 cm^{-1} is assigned to the out- of- plane

deformation of carbonate impurities [86]. The high intensity features located at 1008 and 976 cm^{-1} are ascribed to Si–O in plane stretching vibration [87], while the minor contribution at 689 cm^{-1} is associated with translation of hydroxyls in Mg_3OH groupings [88].

Several changes take place in the FTIR features upon calcination of sepiolite. The features related to the presence of water molecules significantly decrease for sepiolite calcined at 600 °C and completely disappear for sepiolite samples calcined at 750 and 900 °C. The main features at around 1020 cm^{-1} for sepiolite treated at 600 and 750 °C are ascribed to Si–O–Si in plane vibrations [81]. The shoulders at around 960 and 880 cm^{-1} for sepiolite treated at 600 and 750 °C are related to asymmetric stretching vibrations of Si–O–Si and Si–OH bending, respectively [89]. The intensity of the feature around 1450 cm^{-1} decrease with calcination and completely disappear for the sepiolite sample treated at 900 °C. Significant differences in the FTIR spectrum are observed for the sepiolite sample calcined at 900 °C. New features are formed at 1068 and 925 cm^{-1} which are due to Si–O stretching vibrations of enstatite [82]. These results are in agreement with the XRD results presented in Figure 2.1.

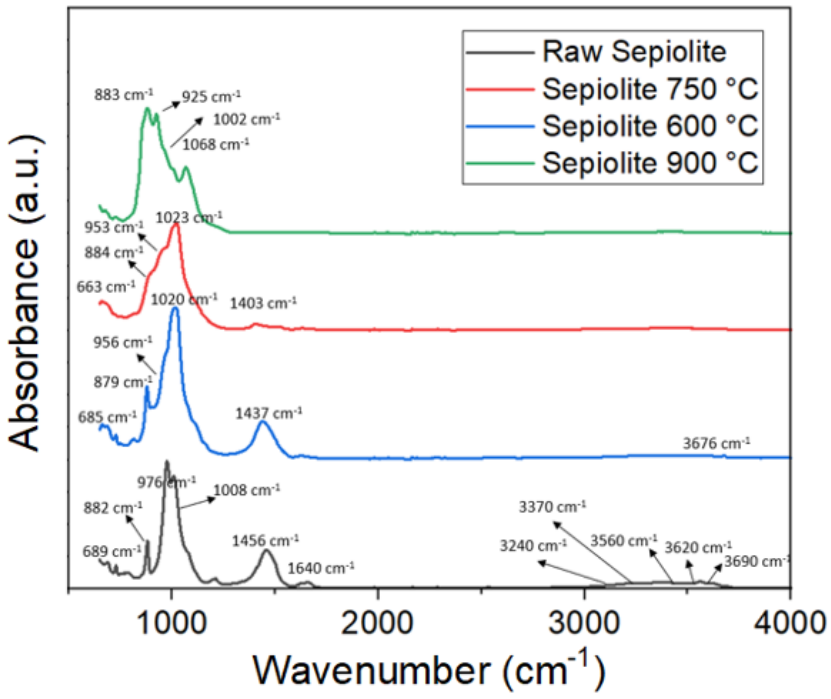

Figure 2.2. FTIR spectra of sepiolite and calcined sepiolite samples at 600 °C, 750 °C and 900 °C.

During thermal treatment of sepiolite, several transformations take place. In his study, Kok investigated the thermal behavior of sepiolite samples by TG/DTG analysis. The results of the study revealed that there are four distinct weight loss regions for sepiolite. The first peak is attributed to the loss of hygroscopic and zeolitic water, while the second peak is related to the loss of half the Mg-coordinated water and structural modification. The third peak and fourth peak are attributed to the loss of second half of the Mg-coordinated water still remaining in the channels and dihydroxylation of the octahedrally coordinated hydroxyl groups, respectively [90].

The TGA curve for raw sepiolite is given in Figure 2.3 together with the sepiolite samples calcined at 600 °C, 750 °C, and 900 °C, respectively.

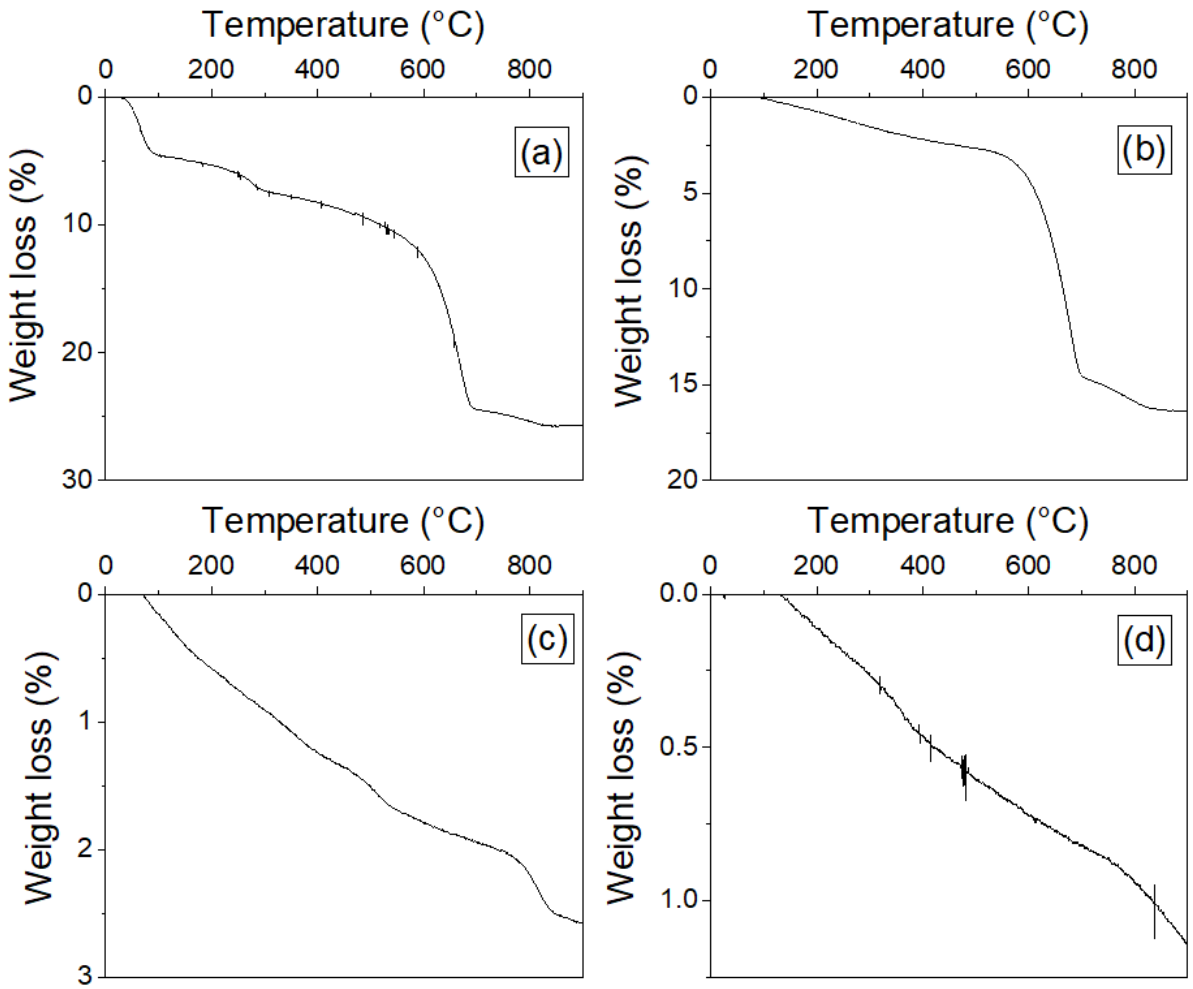

Figure 2.3. Weight loss results of (a) sepiolite and calcined sepiolite samples at (b) 600 °C, (c) 750 °C and (d) 900 °C.

Looking at Figure 2.3 it is seen that removal of hygroscopic water from the external surface and zeolitic water from the voids of the structure takes place up to 220°C with a 6% weight loss. The removal of bound water starts at a temperature of 250°C and continues up to 700°C with a weight loss of 18%. The removal of structural water molecules continues up to 850°C and corresponds to 1% weight loss. The weight loss values for calcined samples are significantly lower compared to uncalcined sepiolite, as expected. The sample calcined at 600 °C exhibits a weight loss of around 16.4%. The weight loss results for the samples treated at 750 and 900 °C are significantly lower, with weight loss values of 2.6% and 1.1%, respectively. The reason for this is that the removal of hydroscopic water, zeolitic water and bound water takes place until 700 °C and these types of water are already removed from sepiolite calcined at 750 and 900 °C. Structural water makes the 1% difference between 750 and 900 °C, and the weight loss results are in agreement with the raw sepiolite results, for which the weight loss for structural water was around 1%.

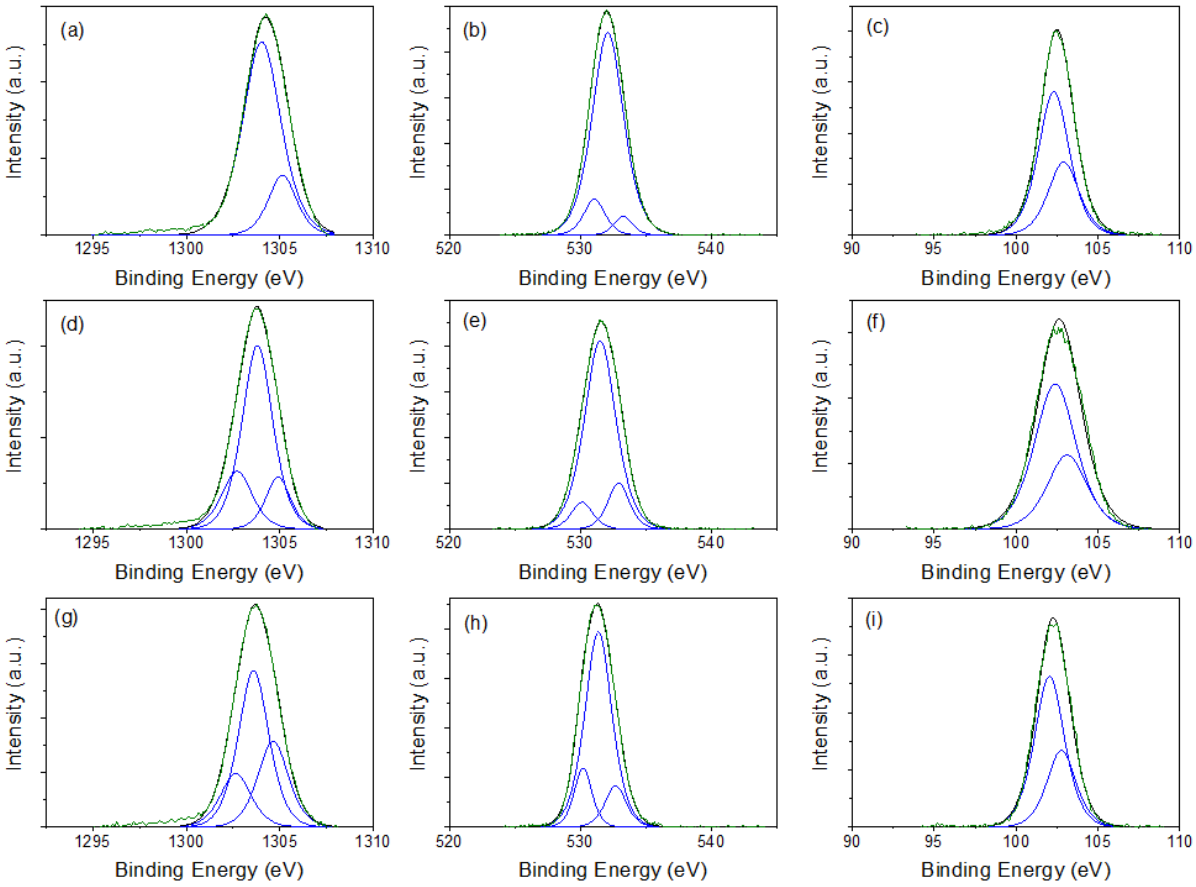

Figure 2.4. Mg 1s, O 1s and Si 2p XP Spectra of calcined sepiolite samples at (a)-(c) 600 °C, (d)-(f) 750 °C and (g)-(i) 900 °C.

XPS analysis was carried out to get an understanding of the surface characteristics with as-received sepiolite along with sepiolite samples calcined at 600, 750 and 900 °C. Deconvoluted O 1s, Mg 1s and Si 2p spectra of the samples and the peak positions are given in Figure 2.4.

Deconvolution of O 1s spectra revealed that the high intensity peak located at approximately 531.8 eV is correlated with the binding energy of O 1s in Mg–O–Si environment [91]. The feature at around 532.9 eV in all the samples are ascribed to silicate framework oxygens [92]. The feature at around 530 eV in the spectra of calcined sepiolite at 750 and 900 °C are related to the presence of Si–O oxygens [92].

The main contribution at around 1304 eV in the Mg 1s spectra of the sepiolite samples is related to the Mg-O-Si bonds of sepiolite [93]. The feature at around 1303 eV in the sepiolite samples calcined at 750 and 900 °C are ascribed to Mg–O bonds [91]. The contribution at around 1305 eV is due to Mg^{+2} ions occupied in tetrahedral sites [94].

Two main contributions at around 1303 and 1304 eV are observed in the Si 2p spectra of calcined sepiolite. These contributions are correlated with Si–O–Si and Si–O–Mg bonding environments [91].

2.3.2. Characterization of Geopolymers

The XRD patterns of the selected geopolymers are given in Figure 2.5. The geopolymers are grouped together based on the raw materials that are used in the synthesis.

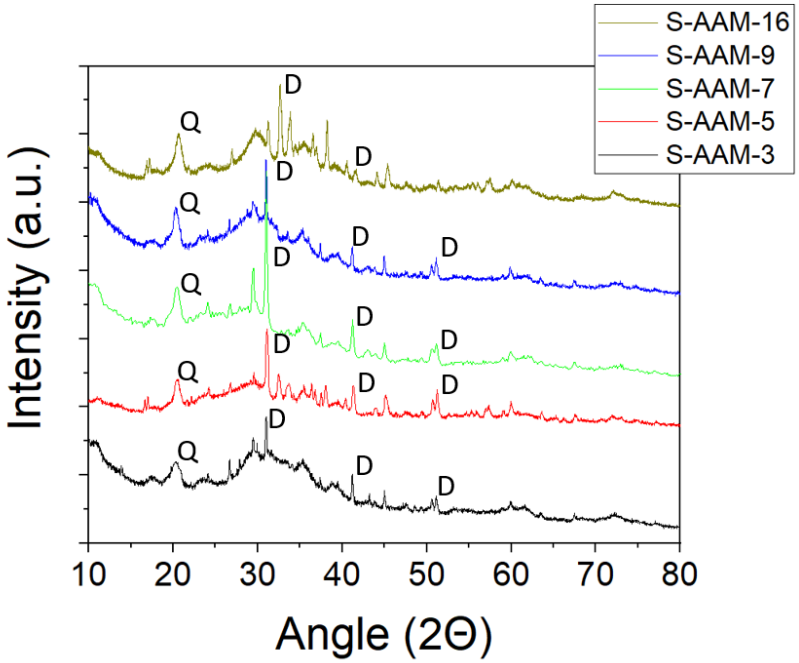

Figure 2.5. XRD Patterns of geopolymers synthesized with sepiolite treated at 600 °C (D: Dolomite, Q: Quartz).

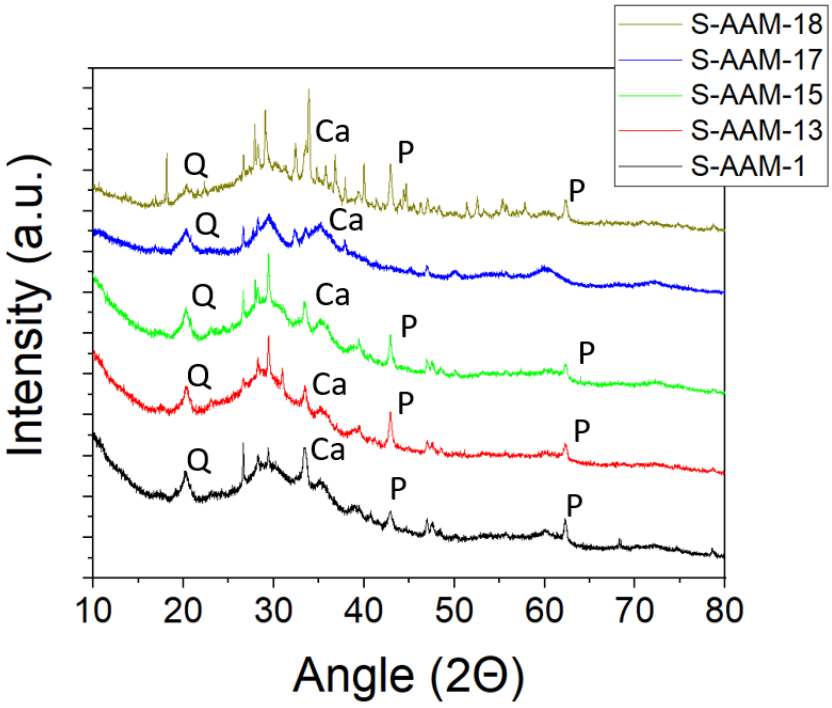

Figure 2.6. XRD patterns of geopolymers synthesized with sepiolite treated at 750 °C (Q: Quartz, Ca: Calcium Magnesium Silicate, P: Periclase).

Comparing the XRD patterns of the geopolymer samples with the XRD patterns of calcined sepiolite in Figure 2.5, it is seen that there is a profound decline in crystalline phase. A featureless hump that is centered around 28° is an indication of geopolymer structure [14]. The hump is observed in many of the alkali activated materials, although some crystalline phases due to quartz, calcite and calcium magnesium silicate are still present.

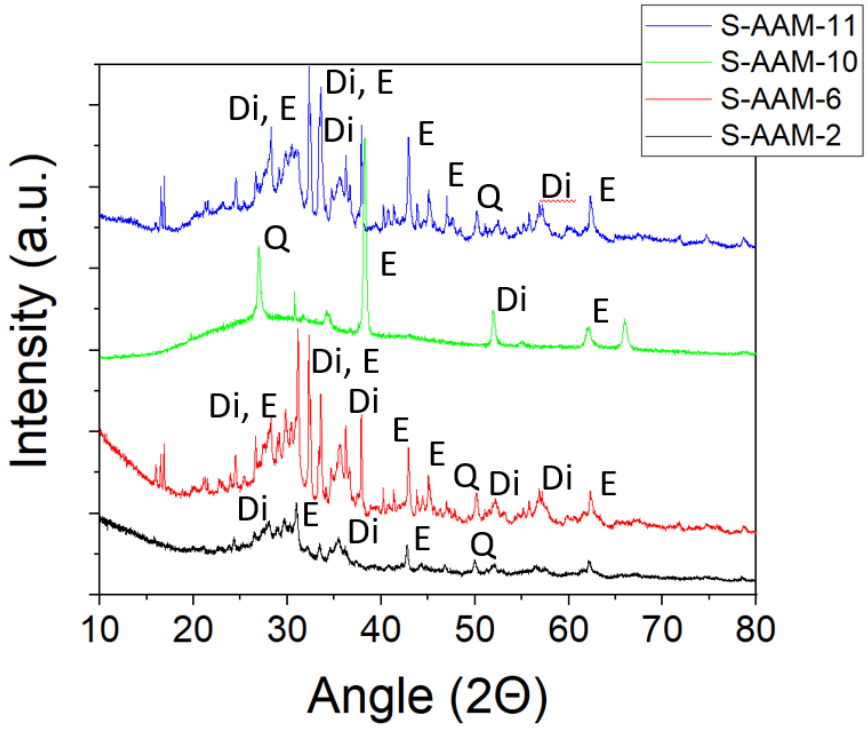

Figure 2.7. XRD patterns of geopolymers synthesized with sepiolite treated at 900 °C (Q: Quartz, Di: Diopside, E: Enstatite).

In addition to the raw sepiolite, the thermal behavior of the SAAM samples are also studied by TGA analysis. The weight loss results for the SAAM samples are given in Table 2.3.

Table 2.3. Weight loss results for different SAAM samples.

	Weight loss (%)
SAAM-1	27.80
SAAM-2	20.90
SAAM-3	30.17
SAAM-4	25.29
SAAM-5	29.15
SAAM-6	16.03
SAAM-7	31.65
SAAM-8	26.11
SAAM-9	29.15
SAAM-10	19.84
SAAM-11	23.01
SAAM-12	26.78
SAAM-13	26.42
SAAM-14	27.08
SAAM-15	29.46
SAAM-16	29.20
SAAM-17	31.84
SAAM-18	27.75
SAAM-19	25.96
SAAM-20	17.63

Looking at Table 2.3 it is seen that the weight loss is strongly correlated with the sepiolite treatment temperature, as expected. The average weight loss is around 25% for all the samples and the thermal stability of the geopolymer samples are high.

2.3.3. Relations Between Synthesis Conditions and Compressive Strength

Compressive strength data is collected for geopolymer samples prepared with different synthesis parameters. The results for the compressive strength measurements are given in Table 2.4 along with a representation on a 3D map in Figure 2.8.

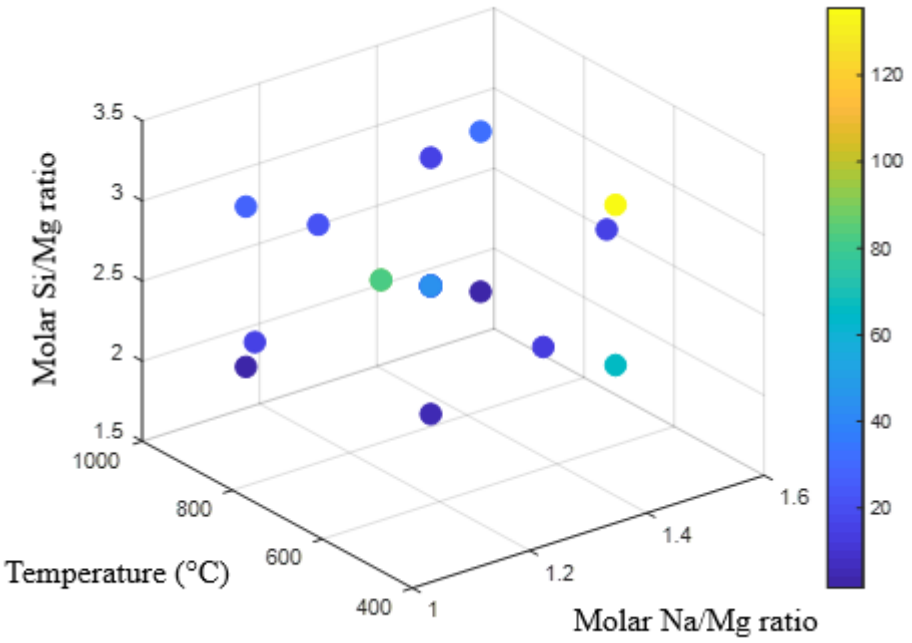

Figure 2.8. Compressive strength results for different geopolymer samples on a 3D map.

When the compressive strength results and the XRD patterns given in Figure 2.5-2.7 are evaluated together, it is seen that geopolymers with low compressive strength, such as SAAM-6 and SAAM-11, it is seen that these materials have higher amounts of crystalline structures. Several reactions, including dissolution, reorientation and solidification takes place during alkali activation [95]. The presence of high amounts of crystalline phases in these samples is an indication that these reactions did not take place to the extent that geopolymerization reactions are complete. This might be correlated with the lower compressive strength results of these samples.

Table 2.4. Compressive strength results.

	Compressive Strength (MPa)
SAAM-1	33.9
SAAM-2	31.0
SAAM-3	92.4
SAAM-4	43.8
SAAM-5	65.7
SAAM-6	1.5
SAAM-7	14.8
SAAM-8	24.0
SAAM-9	135.5
SAAM-10	27.1
SAAM-11	3.2
SAAM-12	34.5
SAAM-13	14.9
SAAM-14	42.6
SAAM-15	15.8
SAAM-16	13.1
SAAM-17	3.8
SAAM-18	15.8
SAAM-19	44.7
SAAM-20	21.5

The results in Table 2.4 indicate that the compressive strength depends very much on the synthesis parameters. The compressive strength values range between 1.5 MPa and 135.5 MPa. The relation between the synthesis parameters and compressive strength is investigated by generating a model in order to learn more about the critical parameters on compressive strength.

The inputs for the model were the synthesis parameters and the output was the compressive strength values. Deviations from normal distribution were observed when

compressive strength was used in linear regression. Therefore, $1/\sqrt{Compressive\ Strenght}$ transformation was used in the modeling studies. A model of the form given in Eq 2.1 with backward elimation was generated. The linear terms are added to the model at the end to preserve model hierarchy. The model results are presented in Table 2.5.

Table 2.5. Model results for synthesis parameters and compressive strength.

Source	DF	Adj SS	Adj MS	F-Value	P-Value
Regression	4	0.437	0.109	9.82	0.000
Temperature	1	0.107	0.107	9.64	0.007
Si/Mg Ratio	1	0.013	0.013	1.18	0.295
Si/Mg Ratio*Si/Mg Ratio	1	0.074	0.074	6.62	0.021
Temperature*Si/Mg Ratio	1	0.082	0.082	7.38	0.016
Error	15	0.167	0.011		
Lack-of-Fit	10	0.165	0.017	38.16	0.000
Pure Error	5	0.002	0.000		
Total	19	0.604			
R^2	72.36				
Adjusted R^2	64.99				

The R^2 of the model came out to be around 0.72, which indicates that the model can moderately explain the experimental data. Large residuals are observed especially for the samples synthesized at temperature extremes. This indicated that the treatment temperature range that is used in this study is too large and quadratic term is not enough to explain the data. In order to improve the model, the current model is used as a guide to estimate the range of synthesis conditions that could result in higher compressive strength values and compressive strength data at these synthesis conditions is collected. The conditions are chosen as Na/Mg ratio = 1.3, Si/Mg ratio = {2.25, 2.75} and T = {625, 675 °C}. The synthesis conditions for the new set is presented in Figure 2.9:

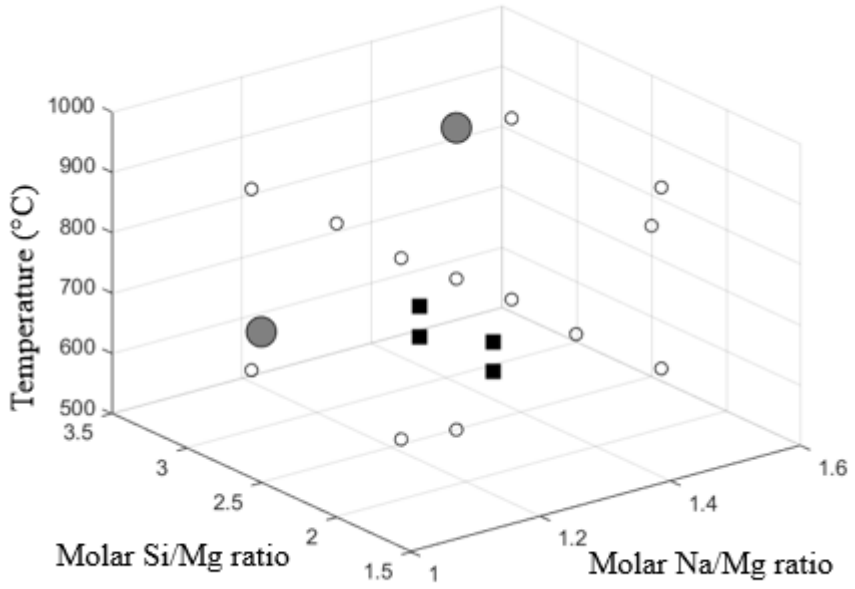

Figure 2.9. 20 samples from CCD (empty circle), 4 additional tests (full square) and 2 CCD levels (large circle) that are not used in modeling studies

A new model is generated after removing the temperature extremes (500 and 1000 °C) and adding the new data. The results for the second model are presented in Table 2.6. An investigation of Table 2.6 reveals that the R^2 value of the model significantly improved compared to the initial model with a value around 0.95. The normal probability plot is presented in Figure 2.10.

It is seen from Figure 2.10 that there is not a large deviation from normal distribution. The lack of fit is significant with a p-value of 0.015, which might be a concern regarding the adequacy of model. The updated model needs improvement with data collected in a narrower range. However, it can be used to get an understanding of the effects of the synthesis parameters on the compressive strength.

The obtained model is used to estimate the optimum synthesis conditions for the highest compressive strength. The synthesis conditions that maximize the compressive strength are estimated to be molar Na/Mg ratio = 1.4, pretreatment temperature = 600 °C, molar Si/Mg ratio = 2.48.

Table 2.6. Updated model results for synthesis parameters and compressive strength.

Source	DF	Adj SS	Adj MS	F-Value	P-Value
Regression	7	0.648	0.093	37.21	0.000
Na/Mg Ratio	1	0.029	0.029	11.58	0.004
Temperature	1	0.146	0.146	58.50	0.000
Si/Mg Ratio	1	0.033	0.033	13.32	0.003
Na/Mg Ratio*Na/Mg Ratio	1	0.015	0.015	5.83	0.030
Si/Mg Ratio*Si/Mg Ratio	1	0.088	0.088	35.37	0.000
Na/Mg Ratio*Si/Mg Ratio	1	0.017	0.017	6.63	0.022
Temperature*Si/Mg Ratio	1	0.093	0.093	37.38	0.000
Error	14	0.035	0.002		
Lack-of-Fit	9	0.033	0.004	8.42	0.015
Pure Error	5	0.002	0.000		
Total	21	0.683			
R^2	94.90				
Adjusted R^2	92.35				

Condidering the optimum conditions, it is observed that increasing pretreatment temperature has a negative impact on the compressive strength values. The effects of increasing temperature on compressive strength can be discussed together with the XRD results presented in Figure 2.1. In Figure 2.1, it was observed that increasing the calcination temperature to 900 °C resulted in formation of additional crystalline phases, namely enstatite and diopside. A more crystalline structure might be an important factor to a more brittle material with low compressive strength [17].

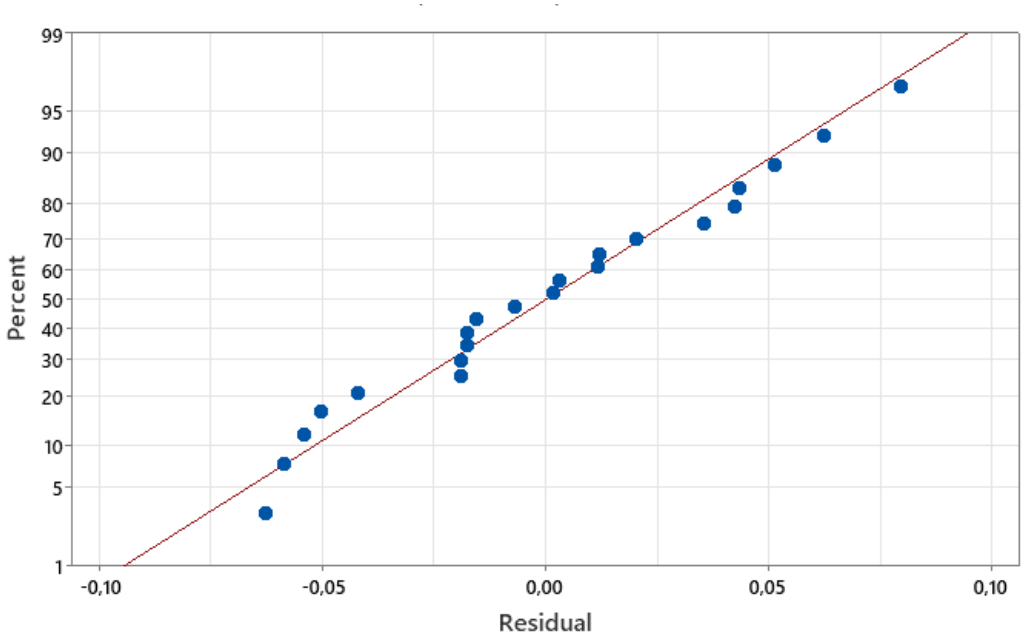

Figure 2.10. Normal probability plot for updated model

The molar Si/Mg ratio of 2.48 predicted by the model indicates that there is a threshold value of Si/Mg molar ratio above which the compressive strength decreases. A similar observation is done for aluminosilicate counterparts in previous studies [19]. The presence of Si up to a threshold value enhances Si–Si structure instead of Si–Al bonds, which results in oligemeric silicates that have higher mechanical strength. After the threshold value, excessive Si in the structure makes dissolution of raw material harder. The unreacted raw material acts as a defect in the structure and causes a decrease in the compressive strength [19].

In a previous study on the mechanism of zeolite synthesis from coal fly ash by alkali hydrothermal reaction, it was proposed that OH^- ion contributes to the dissolution of Si^{+4} and Al^{+3} from fly ash, while Na^+ ion contributes to the crystallization of zeolite [96]. The amounts of these ions in the samples would be parallel to each other as the main source of these ions is NaOH in the activating solution. In a sample with low Na content, the concentration of OH^- would not be sufficient to completely dissolve Si^{+4} and Mg^{+2} from the sepiolite and the low Na content would result in incomplete polymerization of the network. This would result in unreacted sepiolite and consequently lower compressive strength. In case of high Na content, there would be enough OH^- to dissolve Si^{+4} and Mg^{+2} completely. However, in this case there would be excess Na left in the sample, which would weaken the

structure and would again result in a low compressive strength [97]. This means that lower compressive strength results can be obtained at high and low Na content, which might explain the optimum molar Na/Mg ratio value of 1.4 obtained from the model.

2.3.4. Relations Between Formation (Geopolymerization) Kinetics and Compressive Strength

The chemical changes that take place during geopolymerization reactions are investigated by collecting ATR-FTIR data over time. The FTIR spectrum of all the samples after 1 hour, 3 hours and 1 day are given in Figure 2.11 and Figure 2.12. The FTIR data of all the samples over the 30-day period is presented in Figure A.1-A.20 of the Appendix.

Comparing the data in Figure 2.11 and 2.12 with the FTIR spectrum of the calcined sepiolite presented in Figure 2.2, it is seen that the position of the main feature at 1020 cm^{-1} shifts to lower wavenumbers upon alkali activation. Shift of main feature after geopolymerization reactions to lower wavenumbers is verified for other geopolymer samples synthesized as part of this study along with the observations from literature. This systematic shift to lower wavenumbers can be a result of an increase in substitution of Mg in the silicon network [25]. Fly ash-based geopolymers (FGP) and metakaolin-based geopolymers (MGP) are synthesized for a comparison of early stage geopolymerization with SAAMs. The position of the main FTIR feature for early reaction times is given in Figure 2.13.

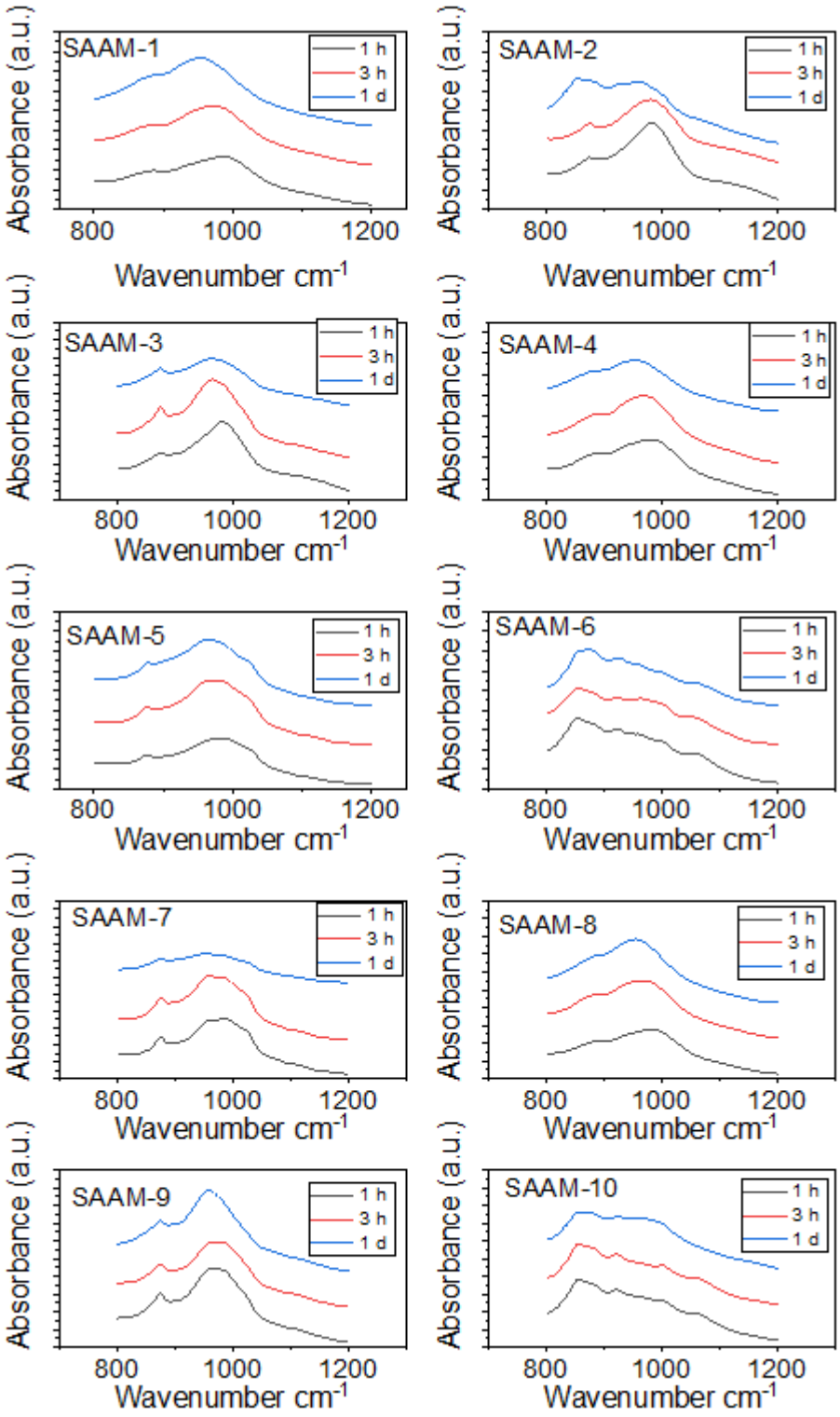

Figure 2.11. FTIR spectra of SAAM-1 to SAAM-10 as a function of time.

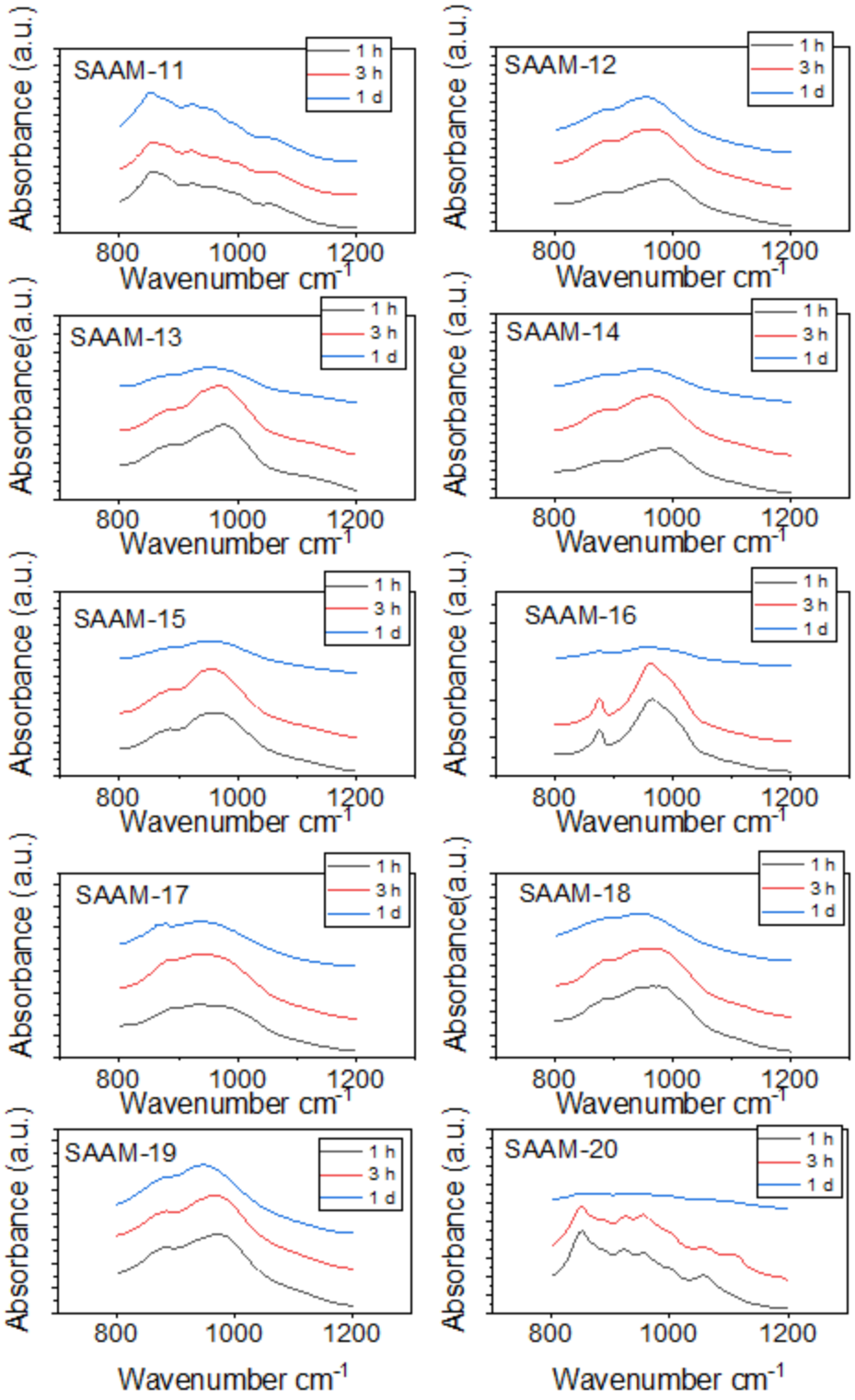

Figure 2.12. FTIR spectra of SAAM-11 to SAAM-20 as a function of time.

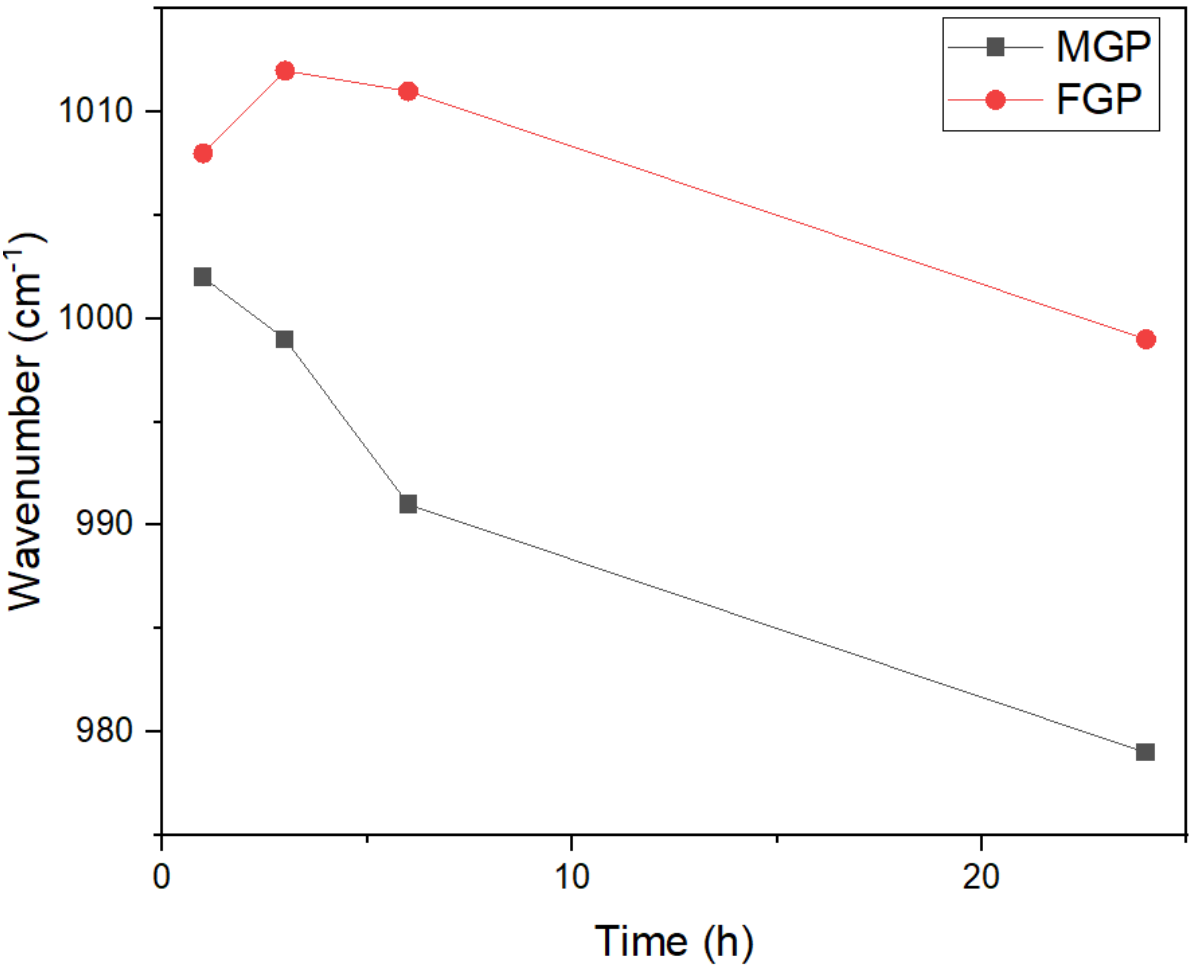

Figure 2.13. Position of main FTIR feature for fly ash and metakaolin geopolymers.

In addition to the observations of the shift to lower wavenumbers upon alkali activation, the changes in the geopolymer samples over time is also studied. For this purpose, the position of the main Si–O–T asymmetric stretching vibration is defined as the point of maximum absorbance in the region 900-1200 cm^{-1} [59] and the position of this feature over different reaction times is monitored. Afterwards, the position of the main feature over time is fitted to an exponential function of the form:

$$\frac{P_e - P_t}{P_e - P_0} = e^{-(\frac{t}{\tau})}, \tag{2.2}$$

where τ represents the time constant and the subscripts 0, t and e represent the position of the main FTIR feature at t=0, any time t and the final value at equilibrium, respectively.

The exponential function fittings for all the samples are done by non-linear least squares fitting and the results are given in Figure 2.14- 2.15, while a summary of the values obtained for Po, Pe and τ are given in Table 2.7.

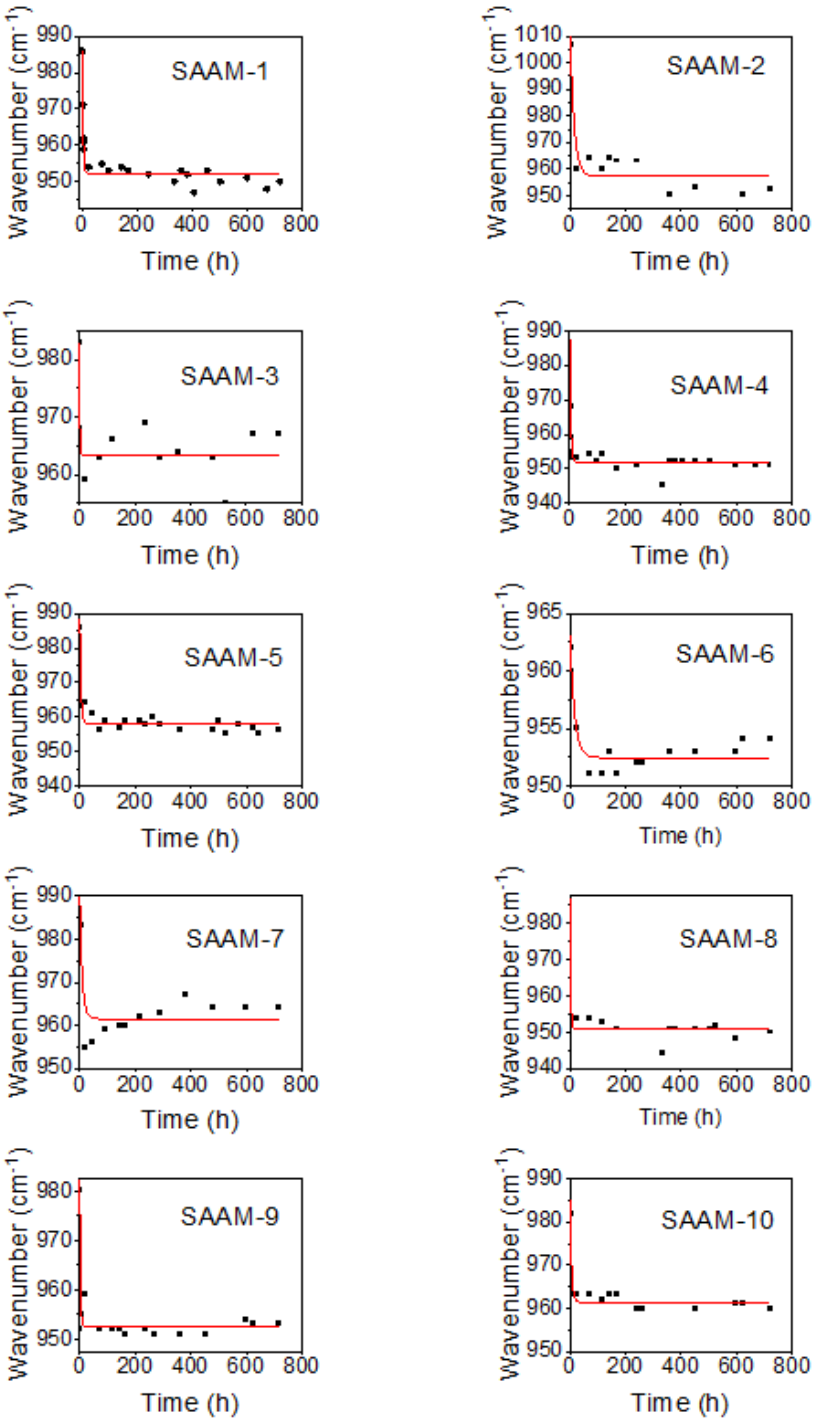

Figure 2.14. Exponential function fit for SAAM-1 to SAAM-10.

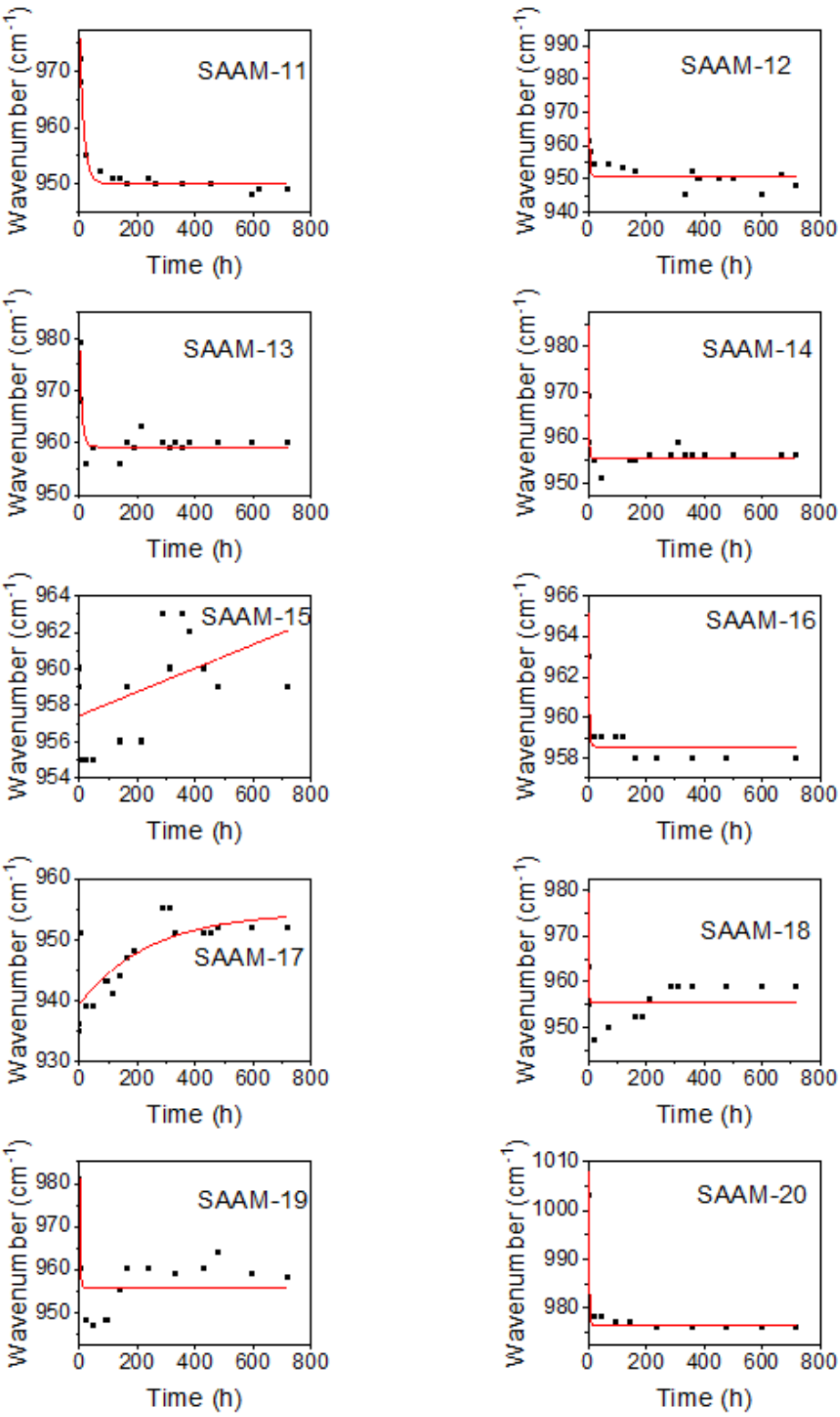

Figure 2.15. Exponential function fit for SAAM-11 to SAAM-20.

Table 2.7. Summary of non-linear least squares fitting.

No	Po	Pe	Tau	Delta
SAAM-1	999.9	952.1	2.9	47.8
SAAM-2	1018.7	961.0	12.7	57.7
SAAM-3	1052.2	963.5	0.7	88.6
SAAM-4	999.0	951.7	3.7	47.4
SAAM-5	999.5	958.1	2.6	41.4
SAAM-6	963.8	952.2	17.1	11.6
SAAM-7	993.1	961.5	9.1	31.6
SAAM-8	1002.9	951.0	2.7	51.9
SAAM-9	995.4	952.5	2.8	42.9
SAAM-10	989.6	961.3	5.8	28.3
SAAM-11	977.6	950.2	14.7	27.4
SAAM-12	1004.8	950.7	2.9	54.2
SAAM-13	980.0	959.2	8.4	20.8
SAAM-14	1005.2	955.6	1.8	49.6
SAAM-15	956.7	963.1	394.8	-6.4
SAAM-16	967.7	958.6	3.1	9.1
SAAM-17	939.5	957.1	319.3	-17.6
SAAM-18	1011.3	956.8	1.1	54.5
SAAM-19	994.4	955.8	2.4	38.7
SAAM-20	1021.9	976.3	2.8	45.6

The compressive strength results are investigated in relation to the data in Table 2.7 in order to get an understanding of how geopolymerization kinetics impact compressive strength. For this purpose, a parameter, Delta, is defined as Po-Pe. The relationship between Delta and the compressive strength is presented in Figure 2.16.

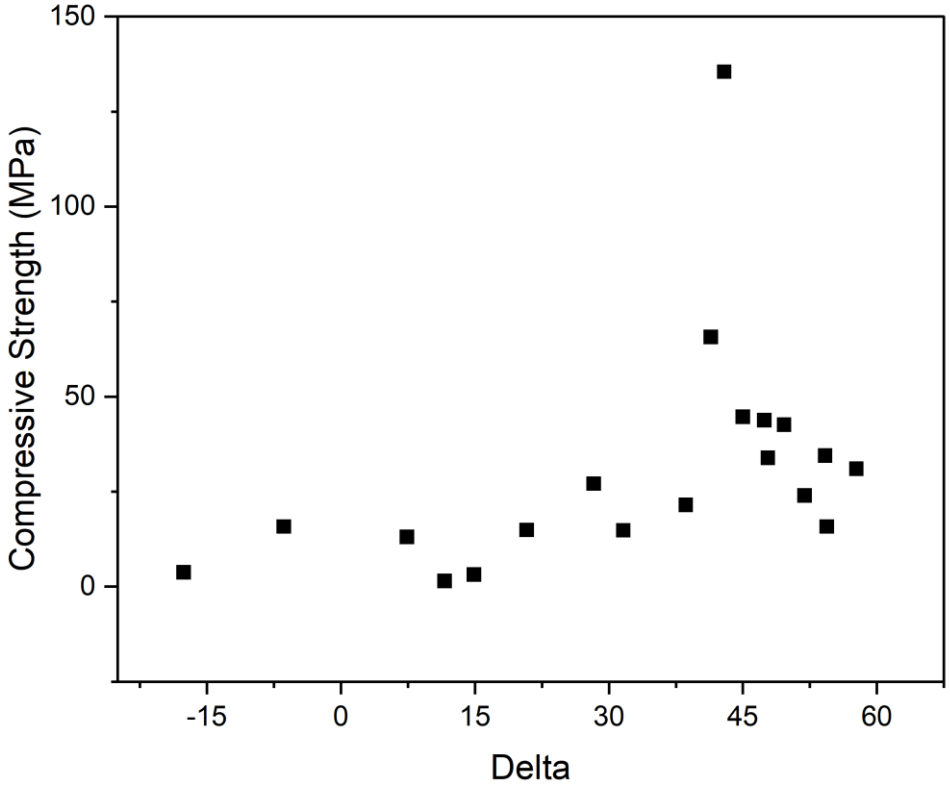

Figure 2.16. Relationship between Delta and compressive strength.

An investigation of Figure 2.16 reveals that Delta and compressive strength have a positive correlation, meaning that a higher compressive strength is observed for geopolymer samples with higher shift in their main FTIR features. This shift indicates changes in the length and angle of Si–O–T bonds in the gel [98]. This can be as a result of more substitution of Mg into the geopolymer network [99]. The shift to lower wavenumbers indicates reduced time until gel formation, which can be correlated to the higher compressive strength results.

In addition to the investigation of the relationship between Delta and the compressive strength, the relation of Delta to the synthesis parameters is also studied. The results indicated that the shift to lower wavenumbers increases with increasing Si/Mg ratio with a correlation coefficient of 0.41. In the presence of higher silica concentration, liberation of more Mg-rich species might be taking place resulting in higher Mg substitution into the geopolymer network and a higher shift in the position of the main FTIR feature.

In addition to these studies, the effects of τ on the compressive strength is investigated. The value of τ indicates how fast the shift to lower wavenumbers takes place, with a low τ meaning a more rapid change. The relationship between τ and the compressive strength is presented in Figure 2.17.

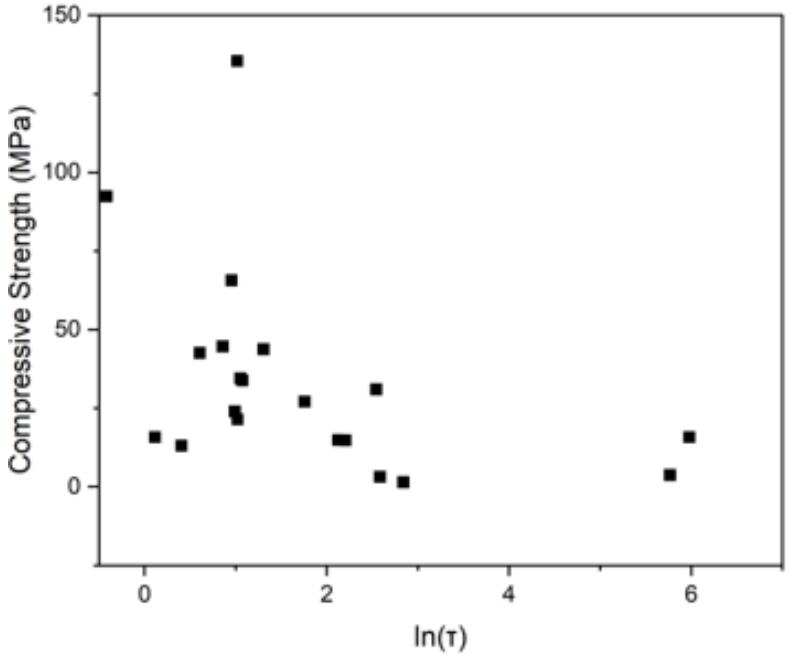

Figure 2.17. Relationship between ln(τ) and compressive strength.

Looking at Figure 2.17, it is seen that lower compressive strength values are obtained for the samples with higher τ. This means that a higher compressive strength is obtained for samples for which the shift in FTIR peak position takes place at the early stage and more rapidly. This result is a clear indication that early geopolymerization is a big contributor to the compressive strength.

2.3.5. Relations Between Atomic Scale Characteristics and Compressive Strength

Atomic scale characteristics of the SAAMs are investigated by XPS analysis. Deconvoluted Mg 1s, O 1s and Si 2p XP spectra of geopolymer samples and related peak positions are given in Figures 2.18-2.23.

An investigation of the Si 2p spectra reveals that the Si 2p spectra of the geopolymer samples display two main features corresponding to Si bonding in Si–O–Mg and Si–O–Si environments [91]. A comparison of the Si 2p spectra of geopolymer samples and the calcined

sepiolite reveals that there is a slight shift to lower binding energies upon alkali activation, which is in agreement with previous findings [37].

The data presented in Figure 2.18-2.23 along with the data for the raw materials that are used in the synthesis of SAAMs points out that a shift in Mg 1s binding energy takes place upon alkali activation. This shift can be related to transition of octahedral Mg atoms to tetrahedral coordination [100]. This transition was previously verified ^{25}Mg MAS NMR spectroscopy [58].

By making use of the data in Table 2.7 and the compressive strength measurements, correlation between compressive strength and XPS spectra is investigated. For this purpose, the shift in the binding energy for Mg 1s, Si 2p1 and Si 2p3 upon alkali activation is presented in Figure 2.24.

An investigation of Figure 2.24 reveals that there is a correlation between Delta Mg 1s, which is defined as the shift of peak Mg1s binding energy from calcined sepiolite to geopolymer sample, and the compressive strength. The shift in binding energy can be related to the transition of octahedral Mg atoms into tetrahedral coordination upon alkali activation [100]. This shift can be considered as an indication of degree of geopolymerization as tetrahedral coordination would be expected in the geopolymer structure. In this sense, higher compressive strength values can be explained by higher degree of geopolymerization observed in XPS measurements. This is in agreement with the FTIR results previously described in Figure 2.11-2.12.

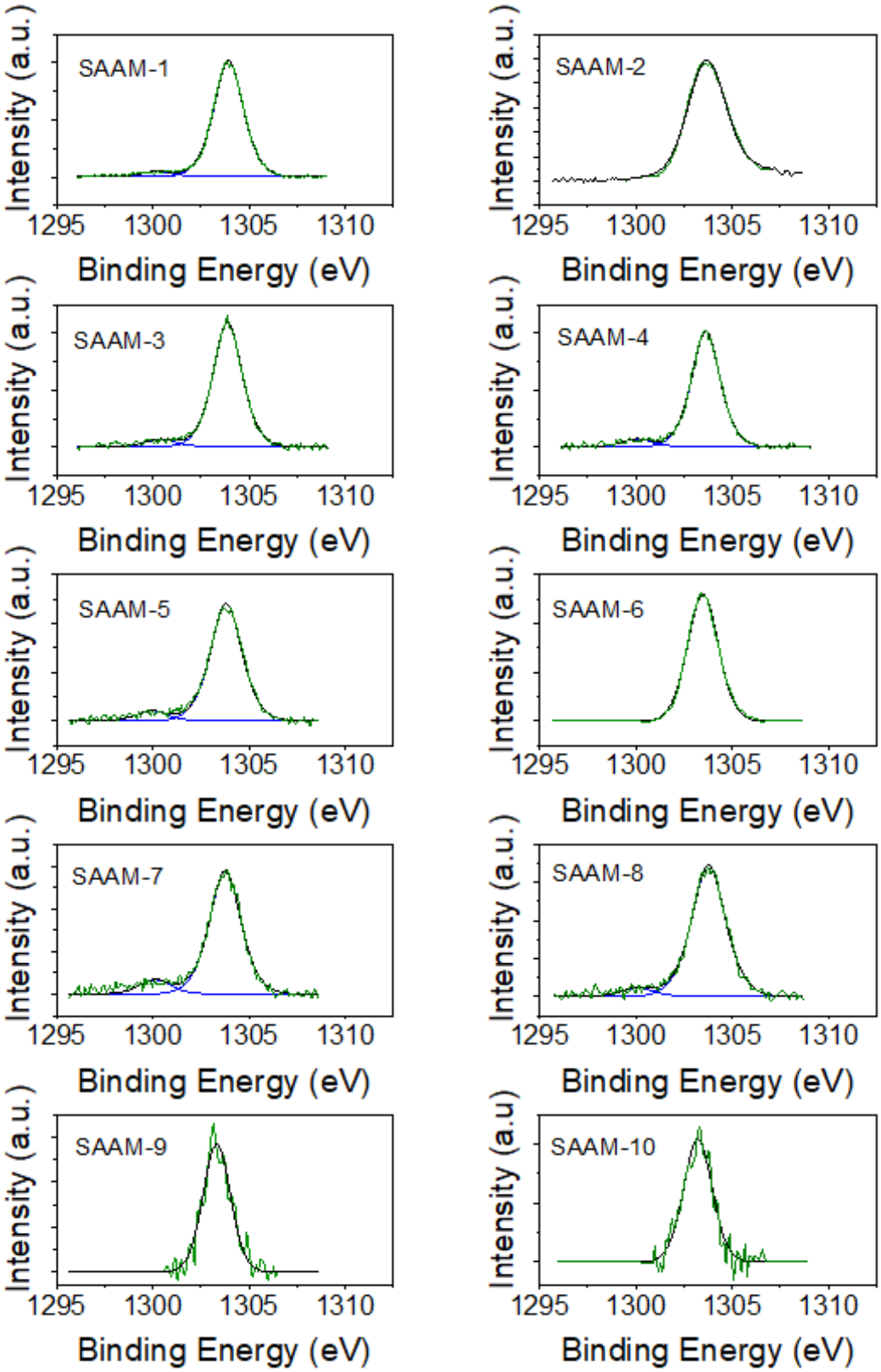

Figure 2.18. XPS Mg 1s spectra for SAAM-1 – SAAM-10.

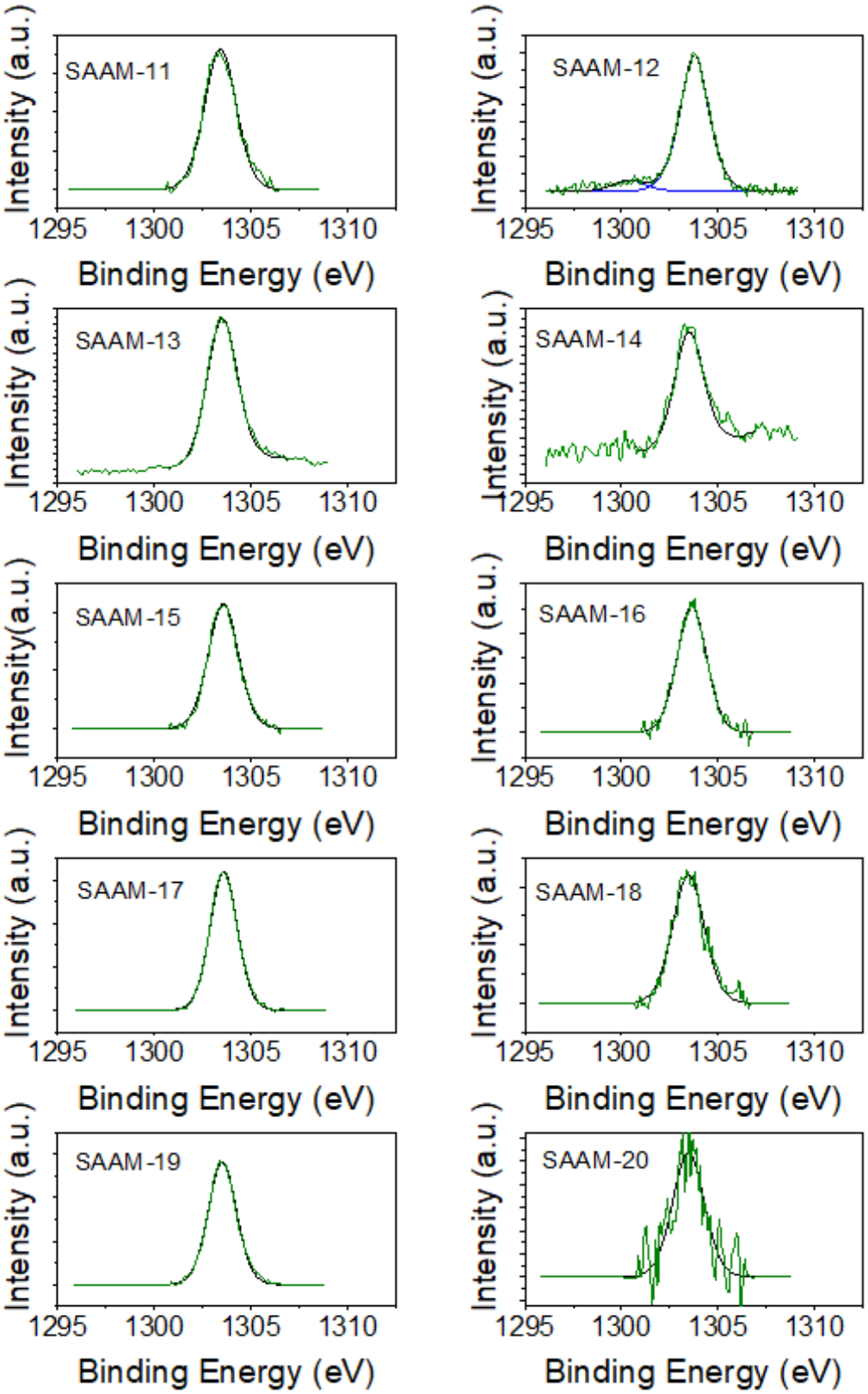

Figure 2.19. XPS Mg 1s spectra for SAAM-11 – SAAM-20.

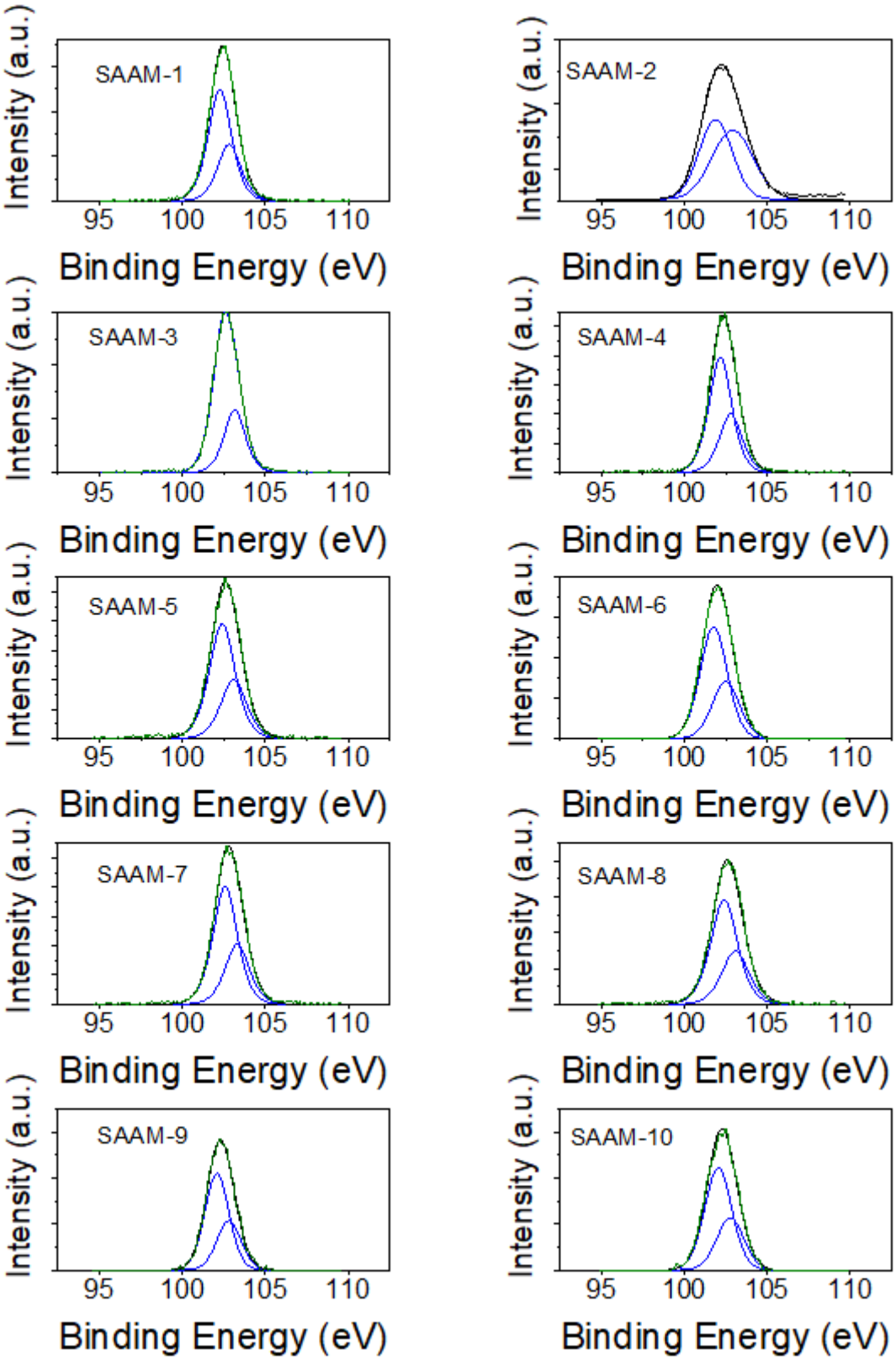

Figure 2.20. XPS Si 2p spectra for SAAM-1 - SAAM-10.

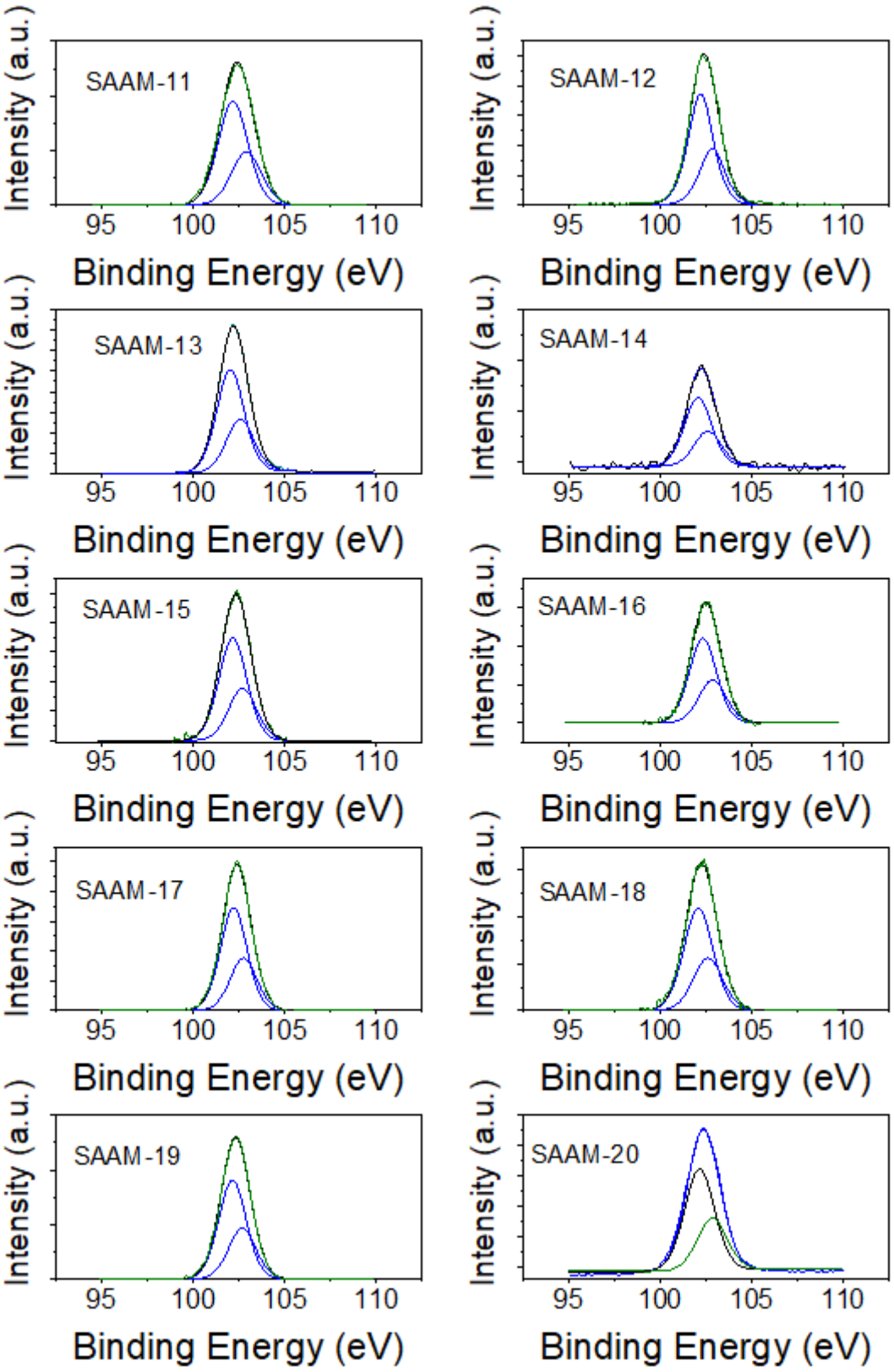

Figure 2.21. XPS S i2p spectra for SAAM-11 to SAAM-20.

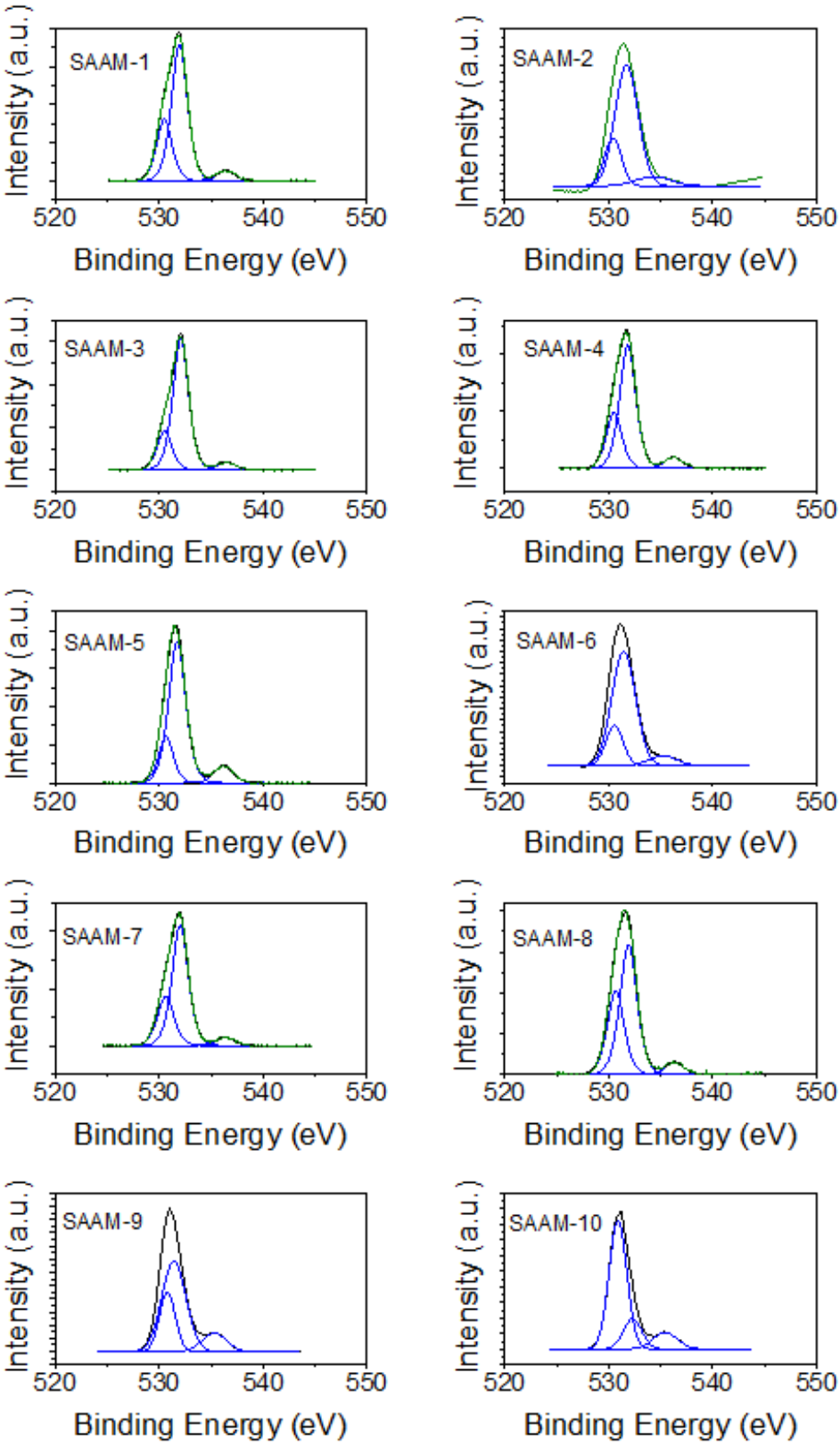

Figure 2.22. XPS O1s spectra for SAAM-1 - SAAM-10.

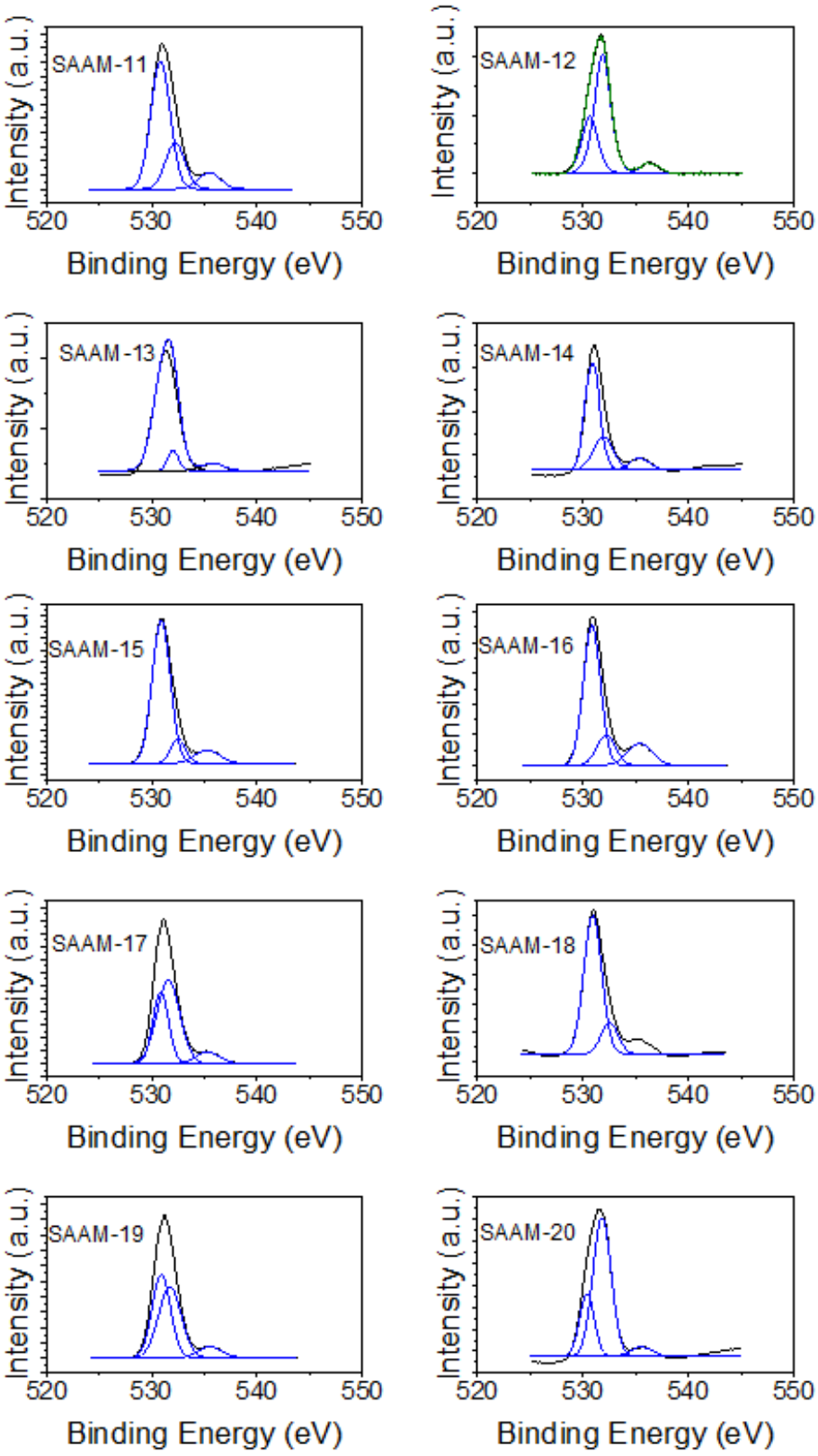

Figure 2.23. XPS O1s spectra for SAAM-11 - SAAM-20.

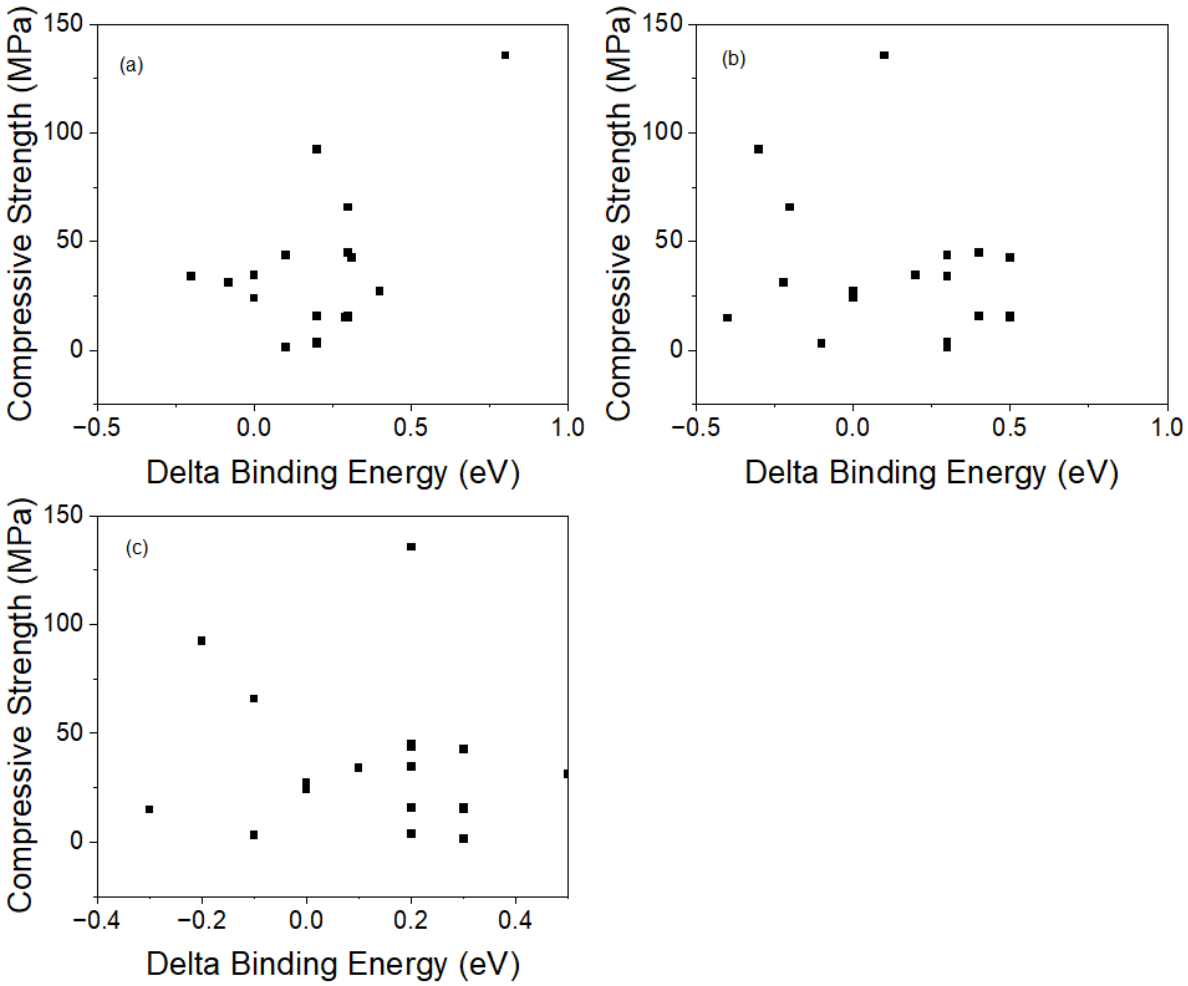

Figure 2.24. Relationship between XPS spectra and compressive strength (a) Delta Mg 1s (b) Delta Si 2p1 (c) Delta Si 2p3.

2.4. Conclusions

In this section, an in-depth analysis of the effects of synthesis parameters on the compressive strength of SAAMs is done for the first time. The results demonstrated that increasing pretreatment temperature has a negative impact, while increasing Si/Mg ratio has a positive impact on the compressive strength of the materials. The raw materials and the S-AMMs are characterized by XRF, XRD, TGA and XPS. The comparison of the XRD patterns of the SAAMs and the calcined sepiolite samples demonstrate that there is a significant decline in crystalline phase upon alkali activation. The hump that is centered around 28° is observed in many of the alkali activated materials, although some crystalline

phases due to quartz, calcite and calcium magnesium silicate are still present. The TGA results point out that the thermal stability of the SAAMs are high and the weight loss values decrease with increasing sepiolite pretreatment temperature, as expected. The atomic scale characteristics of the SAAMs is studied by XPS analysis. An investigation of the XPS results together with the compressive strength results indicated that a shift in the peak binding energy of Mg 1s spectra is correlated with the compressive strength measurements. The shift in binding energy can be related to the transition of octahedral Mg atoms into tetrahedral coordination upon alkali activation, thus a higher degree of geopolymerization and higher compressive strength. The relation between the reaction kinetics and the compressive strength is investigated by collecting FTIR data at different reaction times. The relation is quantified by fitting an exponential function to the position of the main FTIR feature over time. The results demonstrated that a higher compressive strength is obtained for samples for which the shift in FTIR peak position takes place at the early stage and more rapidly. This result is a clear indication that early geopolymerization is a big contributor to the compressive strength.

3. OPTIMIZATION OF SYNTHESIS PARAMETERS FOR SEPIOLITE- BASED ALKALI ACTIVATED MATERIALS FOR THE REMOVAL OF METHYLENE BLUE FROM AQUEOUS SOLUTIONS

3.1. Introduction

Industrialization and urbanization is increasing rapidly in the last few decades. Water pollution is becoming an important global issue due to insufficient treatment of the wastewater produced from different industries. Among different pollutants, dyes are one of the most threatening compounds for the water resources due to their toxic and carcinogenic nature [46]. In addition to that, dyes are harmful to the aquatic ecosystem, since they reduce the light penetration into the water [101]. There are more than 100.000 commercially available dyes [102] and the annual production of dyestuffs is more than $7x10^5$ tons [103]. It is estimated that more than 10-15 % of the dyestuff used in dye manufacturing and textile industry is released into the environment [104] and therefore it is vital to find solutions for the removal of dyes from wastewater.

Several methods are suggested for the removal of dyes from water, such as precipitation [105], membrane separation [106, 107], oxidation [108, 109], photocatalytic degradation [61] and adsorption [102], [110]. Among these methods, adsorption is regarded as a promising technique due to its economic feasibility, high efficiency, easy operation and adsorbents regeneration [111-114]. Different types of adsorbents are used for the removal of dyes from water, such as clays [115, 116], activated carbon [117, 118] and metal organic frameworks [119]. Activated carbon is the benchmark material for adsorption because of its high surface area, high stability and durability [49], [120]. Despite the unique properties of activated carbon, its high synthesis costs and difficulties in regeneration [49], [121] has led to extensive research for low cost alternatives. One promising alternative can be the use geopolymers [46], [49], [52], [122, 123]. Geopolymers are extensively researched due to their good mechanical strength, high durability, high thermal stability and toxic immobilization [122], [124].

Geopolymers are emerging as alternative and sustainable construction materials that can replace Portland Cement [17], [68], [125]. Geopolymer is a three-dimensional aluminosilicate structure with amorphous or semi-crystalline microstructure [123]. Materials that are commonly used as cementitious materials, such as blast furnace slag, fly ash, calcined clays and pozzolans, are suitable to be used as the precursor for the synthesis of geopolymers [6]. The successful implementation of these raw materials were shown in previous studies [69-71]. Even though the main application area of the geopolymers started as construction materials, the use of geopolymers for adsorption purposes is gaining interest [46], [49], [52], [70], [122].

One of the main reasons for geopolymers as a potential material to be used for adsorption purposes is that, geopolymers can be synthesized from cheap and abundant raw materials with very low synthesis costs. Because of this reason, sepiolite offers great potential to be used as a raw material in geopolymer synthesis. Sepiolite is a natural hydrous magnesium silicate material with the chemical formula $Si_{12}O_{30}Mg_8(OH)_4(H_2O)48H_2O$ [53]. Sepiolite is a widespread and abundant material. Spain is the world's largest sepiolite producer and 90% of the sepiolite in Europe comes from Spain with the remaining sepiolite mainly coming from Turkey [74]. Sepiolite has a unique structure formed by blocks and channels that extend in the fibre direction. Each block is made up of two tetrahedral silica sheets and a central octahedral magnesium sheet [126]. Its porous and fibrous structure along with its high surface area makes the penetration of organic and inorganic ions into the sepiolite easier [77], [127-129]. Because of its high surface area and unique structure, sepiolite is used in a wide range of areas including catalyst support and ion adsorption [75-77]. These studies clearly show that sepiolite offers broad potential for adsorbing water and organic molecules.

Even though sepiolite has excellent adsorption properties, it does not offer mechanical performance, which might limit its application. It is very important for the adsorbent material to have the necessary mechanical strength so that it will not cause any problems in the industrial units and it will be suitable for regeneration compared to powder adsorbents [57]. To fill in this gap, a previous study in our research group introduced a sepiolite geopolymer with high methylene blue adsorption capacity and high mechanical strength [52]. They

concluded that these innovative materials offer high potential for wastewater treatment and they can contribute to circular economy as a material to be used in sustainable construction. This study featured only one synthesis condition and focused on the effects of different parameters, such as pH, temperature, contact time, and regeneration potential. However, different applications might require different adsorption and mechanical characteristics. Therefore, an in-depth analysis of different synthesis parameters on the mechanical strength and adsorption properties is required.

In order to respond to this need, this chapter of the study focuses on an investigation of the effects of synthesis parameters on the methylene blue adsorption properties of SAAMs by means of an experimental design. Response surface methodology is used to determine the optimum values of molar Na/Mg ratio, sepiolite treatment temperature and molar Si/Mg ratio, and molar Na/Mg ratio, with the MB adsorption capacity as the output. The SAAMs were characterized by X-ray Diffraction (XRD), Fourier Transform Infrared Spectroscopy (FTIR), X-ray Photoelectron Spectroscopy (XPS), Thermogravimetric analysis (TGA), Brunauer- Emmett- Teller (BET) analysis. The obtained adsorption data can be used in parallel with the compressive strength data presented in Chapter 3 for a more in-depth analysis of applicability of the materials in an industrial environment. The results of this chapter are being prepared for publication.

3.2. Materials and Methods

3.2.1. Sample Preparation

Sepiolite was kindly supplied by Dolsan Mining, Eskişehir, Turkey. Activating solution is prepared by mixing sodium silicate ($Na_2Si_3O_7$) solution (%9 of Na_2O, 28% of SiO_2 and 63% of H_2O; density: 1.401g/ml at 20 °C) and sodium hydroxide (NaOH) pellets.

Sepiolite was treated at 5 different temperatures for 1 h. The treatment temperatures were 500, 600, 750, 900 and 1000 °C. Powdered and sieved (#70 mesh sieve, 200 μm) calcined sepiolite was mixed thoroughly with necessary amount of activating solution to obtain desired Si/Mg and Na/Mg ratios.

3.2.2. Structural Characterization

The chemical compositions of raw and calcined sepiolite were determined using X-ray fluorescence (Bruker S8 Tiger). X-ray diffraction (XRD) measurement of the raw materials and selected SAAMs were performed on a Bruker D8 Advance Diffraction system with a Cu Kα1 radiation source. XRD data is collected 3 months after the samples were synthesized. The data were recorded in the range $2\theta = 10–80^{\circ}$. The FTIR spectroscopy of the raw materials and selected SAAMs were collected using a Perkin Elmer Frontier FT-IR Spectrometer. Absorbance spectra was collected in the range from 4000-650 cm^{-1} at a resolution of 2 cm^{-1} and a scanning speed of 5 kHz with 16 scans. X-ray photoelectron spectroscopy (XPS) analysis was conducted on a Thermo Scientific K-Alpha X-ray Photoelectron Spectrometer and Avantage 5.9 software was utilized for XPS data fitting. Thermogravimetric analysis (TGA) was conducted on a Perkin Elmer TGA 4000 instrument. The analysis was done in a temperature range from 25 to 900 °C at a heating rate of 10 °C/min for raw sepiolite, calcined samples and the selected SAAMs under N_2 flow.

3.2.3. Compressive Strength Measurements

Compressive strength measurements were conducted on a MTS model servo-hydraulic test machine with capacity of 500 kN with a loading rate of 0.01 mm per second. After synthesis, the geopolymer samples were poured into 1 cm × 1 cm × 1 cm silicon molds and kept at room temperature for 6 weeks before compressive strength measurements.

3.2.4. Methylene Blue Adsorption Tests

Adsorption properties of the synthesized samples was investigated by the method introduced in the work by Kaya-Özkiper et al. [52]. 10 mg of powdered and sieved (#70 mesh sieve, 200 μm) adsorbent is immersed into 50 ml of methylene blue solution with a concentration of 20 mg/L. The mixtures were stirred at 700 rpm until equilibrium was reached. Aliquots were collected from the methylene blue solutions and analyzed with a

Flame-S-UV-Vis-ES spectrometer (Ocean Optics, USA) by measuring the absorbance value at λ = 664 nm. Removal efficiency (%) was measured as follows [61]:

$$Removal\ efficiency\ (\%) = \frac{C_o - C_t}{C_o}\ x\ 100 = \frac{A_o - A_t}{A_o}\ x\ 100, \qquad (3.1)$$

where C_0 and C_t are the concentration of MB solution at initial time t = 0 and at time t, respectively. A_0 and A_t denote to absorbance values at initial time t = 0 and at time t, respectively.

The amount of MB adsorbed on adsorbents were determined by:

$$q_e = \left(\frac{C_o - C_e}{m}\right) x\ V, \qquad (3.2)$$

where q_e is the amount of MB dye uptake by the adsorbent (mg MB dye/g adsorbent), m is the mass of the adsorbent (g), and V is the volume of the MB solution (L).

3.2.5. Experimental Design and Statistical Analysis

The effects of three parameters, namely molar Na/Mg ratio, sepiolite treatment temperature and molar Si/Mg ratio on the adsorption of methylene blue was investigated by Response Surface Methodology. The synthesis parameters of the SAAMs were selected using CCD with the adsorption capacity as the output. CCD offers the advantage of running sequentially, meaning that the design can be divided into subsets, the first to estimate linear and two- factor effects and the second to estimate curvature effects [80]. The levels of the synthesis parameters were chosen by making use of previous studies for the optimum conditions with alumina silicate analogues [62]. 20 synthesis conditions were determined in accordance with CCD methodology and were presented in Table 2.2.

3.2.6. Construction of the Predictive Model

The data collected from the experimental design is used to build a predictive model. The adsorption data was fit to a quadratic model with an equation of the form:

$$Y = a_0 + a_1A + a_2B + a_3C + a_{12}AB + a_{13}AC + a_{14}BC + a_{11}A^2 + a_{22}B^2 + a_{33}C^2, \qquad (3.3)$$

where, Y is adsorption capacity(mg/g), a_o is constant coefficient, a_i, a_{ii}, and a_{ij} are linear, quadratic and interaction coefficient; A, B, and, C, are Na/Mg ratio, Temperature and Si/Mg ratio, respectively.

The significance of the model is validated by analysis of variance (ANOVA) with a 95% confidence interval. Backward elimination is used to construct the model. Backward elimination is a method to select a set of exploratory variables for the model. At the beginning, the model contains all the exploratory variables and the variable with the highest p-value is removed from the model. The procedure is repeated until all the remaining exploratory variables are significant, meaning that p-value < alpha. The final model is selected so that only the parameters that are significant are present in the model.

3.3. Results

3.3.1. Structural Characterization

The XRD patterns for as-received sepiolite along with sepiolite calcined at 600, 750 and 900 °C and selected geopolymer samples are given in Figure 3.1. Contributions due to sepiolite and dolomite along with some contributions from quartz are observed in raw sepiolite. Formation of a new feature is observed upon calcination to 600 °C. This feature is attributed to calcite and it represents the first step of calcinations of dolomite to calcite [81]. At the 750 °C calcination temperature, the peaks related to dolomite and sepiolite completely disappear and the formation of new features are observed. These features are attributed to magnesium silicate and periclase. Further structural changes take place at 900 °C calcination temperature with the formation of new peaks that can be attributed to enstatite as a new crystalline phase [81, 82]. A comparison of the XRD patterns of calcined sepiolite with the SAAMs reveals that there is a significant decline in the crystalline phase upon alkali activation. SAAMs are characterized by a featureless hump that is centered around 28° [14]. The hump is present in the XRD patterns of SAAMs given in Figure 3.1, although some crystalline phases due to quartz, calcite and calcium magnesium silicate are still present.

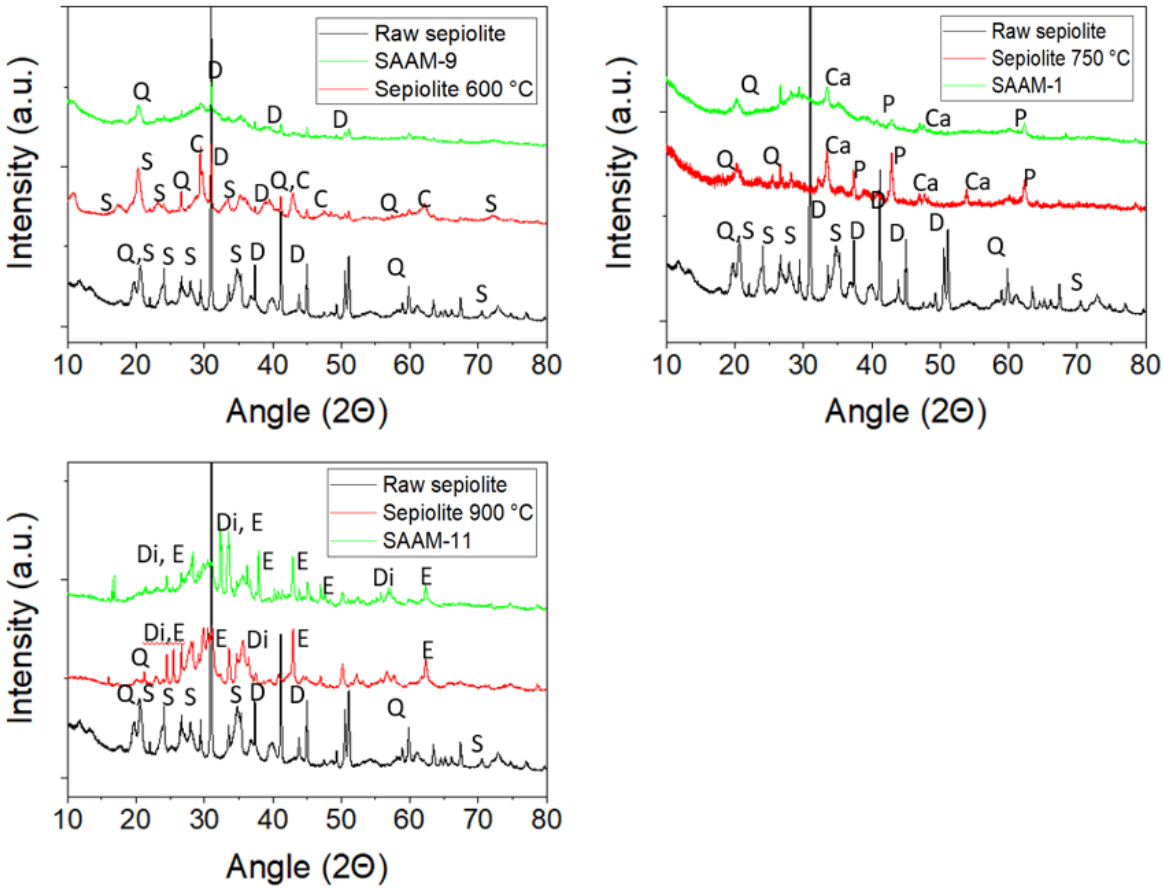

Figure 3.1. XRD Patterns of sepiolite, calcined sepiolite and selected SAAMs (D: Dolomite, S: Sepiolite, Q: Quartz, C: Calcite, Ca: Calcium Magnesium Silicate, P: Periclase, Di: Diopside, E: Enstatite).

The FTIR spectra of raw sepiolite and calcined sepiolite at 600 °C, 750 °C, and 900 °C along with chosen SAAM's are given in Figure 3.2. In the FTIR spectrum of raw sepiolite, the features located at 3690, 3620, 3560, 3370 and 3240 cm^{-1} are related with the presence of water molecules. The high intensity features at 1008 and 976 cm^{-1} are ascribed to Si–O in plane stretching vibration [87]. The feature at 1456 cm^{-1} is related to the stretching vibrations of C–O, which is an indication of carbon impurities [81], [85].

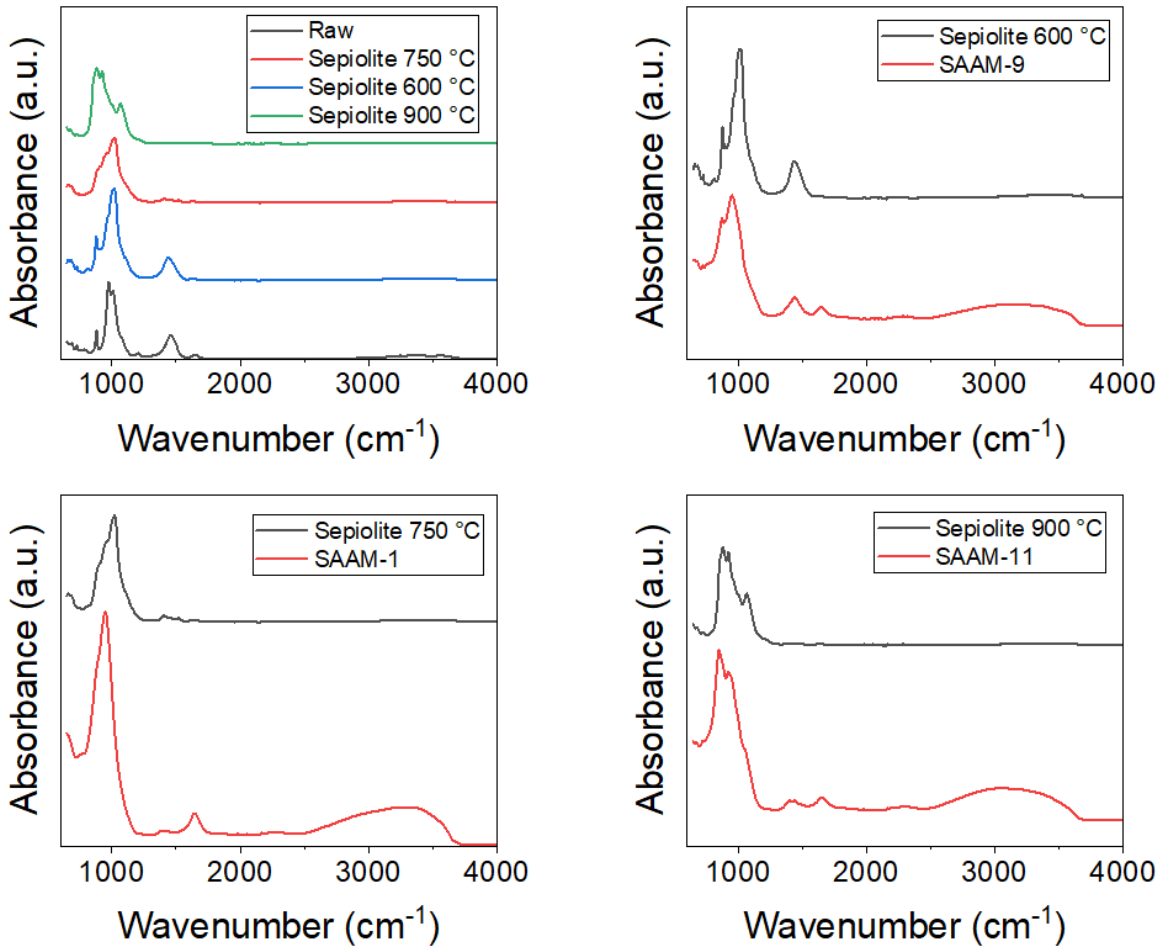

Figure 3.2. FTIR spectra of sepiolite, calcined sepiolite and selected SAAMs.

Upon calcination, several changes take place in the FTIR spectrum of the sepiolite. The features related to water decrease in intensity at 600 °C and completely disappear at 750 and 900 °C. The high intensity features at 1020 cm^{-1} for sepiolite calcined at 600 and 750 °C are associated with Si–O–Si in plane vibrations. The intensity of the feature at 1456 cm^{-1}, which is related to the presence of carbon impurities, decreases with increasing calcination temperatures. New features at 1068 and 925 cm^{-1} are formed for the sepiolite calcined at 900 °C. These features are associated with the formation of an enstatite phase [82]. This observation is in agreement with the XRD results presented in Figure 3.1. A comparison of the FTIR spectrum of the SAAMs and the raw materials which are used in the synthesis of these materials reveal that the position of the main feature shifts to lower wavenumbers upon alkali activation. In their study with fly ash geopolymers, Rees et al. collected in-situ FTIR data with one minute intervals over a time period of three days. They observed a similar shift

in the position of the main FTIR feature. They associated this shift with the formation of an Al-enriched gel phase [25]. The shift in FTIR main position of this study suggests that a similar mechanism to aluminosilicate system can be present for the magnesium silicate counterparts and the shift to lower wavenumbers can be associated with an increase in substitution of Mg in the silicon network A summary of the peak positions and the corresponding assignments are given in Table 3.1.

In a study on the thermal behaviour of sepiolite by TG/DTG analysis, it was observed that there are four distinct weight loss regions for sepiolite samples. The first region was related to zeolitic water, the second region was attributed to the loss of some portion of Mg-coordinated water. The third and fourth peak were related to the loss of remainder of the Mg-coordinated water and dehydroxilation of octahedrally coordinated hydroxly groups [90].

The TGA curve for raw sepiolite is given in Figure 3.3 together with the sepiolite samples calcined at 600 °C, 750 °C, and 900 °C, respectively.

A 6% weight loss is observed up to a temperature of 220 °C, which is attributed to the removal of hydroscopic water and water from the external surface. The bound water is removed from the structure up to a temperature of 700°C and this accounts to an 18% weight loss. The structural water is removed from the structure up to a temperature of 850°C and this corresponds to 1% weight loss. The weight loss for the sample calcined at 600 °C is around 16.4%. As the sample was calcined at 600 °C, most of this loss takes place above this temperature since the hydroscopic water, zeolitic water and some portion of bound water was already removed during calcination. The weight loss results for the samples treated at 750 and 900 °C are significantly lower, with weight loss values of 2.6% and 1.1%, respectively. The reason for this is that the removal of hydroscopic water, zeolitic water and bound water takes place until 700 °C. Structural water makes the 1% difference between 750 and 900 °C, and the weight loss results are in agreement with the raw sepiolite results, which exhibited a 1% weight loss for structural water.

Table 3.1. FTIR peak positions and assignments.

Position (cm^{-1})	**Peak Assignment**	**System**
3690	hydroxyl stretching vibrations of MgOH groups [83,84]	Sepiolite
3620 and 3560	vibrations associated with water coordinated to magnesium ions at the edge of structural blocks [84]	Sepiolite
3370, 3240 and 1640	zeolitic water [84]	Sepiolite
1456	stretching vibration of C–O [47]	Red mud and fly ash geopolymer
	stretching vibration of C-O [51]	Sepiolite
882	out- of- plane deformation of carbonate impurities [86]	Magnesium-aluminum hydrotalcite-like compounds
1008 and 976	Si-O in plane stretching vibration [87]	Sepiolite
689	translation of hydroxyls in Mg_3OH groupings [88]	Sepiolite
1020	Si-O-Si in plane vibrations [81]	Sepiolite
960	asymmetric stretching vibrations of Si-O-Si [89]	Red mud and blast furnace slag geopolymers
880	asymmetric stretching vibrations of Si-OH [89]	Red mud and blast furnace slag geopolymers
1068 and 925	Si-O stretching vibrations of enstatite [82]	MgO - Al_2O_3 – SiO_2 system

The surface characteristics of the raw materials and the SAAMs were investigated by XPS analysis. The XPS spectra were deconvoluted and the corresponding peak positions were presented in Table 3.2- 3.5.

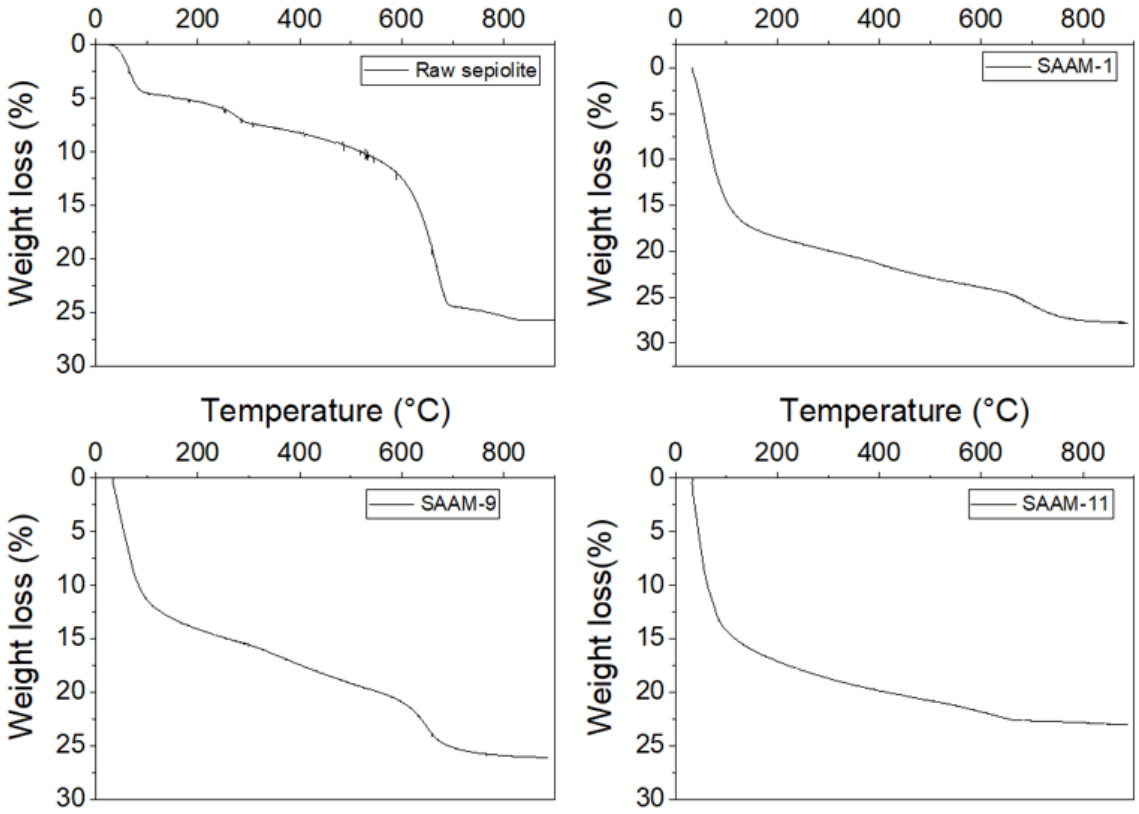

Figure 3.3. Weight loss results of (a) sepiolite and calcined sepiolite samples at (b) 600 °C, (c) 750 °C and (d) 900 °C.

Table 3.2. XPS Mg 1s and Si 2p peak binding positions for sepiolite treated at different temperatures.

	Mg 1s			**Si 2p**	
	~ 1304 eV	**~ 1305 eV**	**~ 1303 eV**	**Si 2p3**	**Si 2p1**
Sepiolite 600 °C	1304.03	1305.14		102.31	102.91
Sepiolite 750 °C	1303.8	1304.9	1302.72	102.39	103.12
Sepiolite 900 °C	1303.6	1304.64	1302.65	102.04	102.77

Table 3.3. XPS O 1s and C 1s peak binding positions for sepiolite treated at different temperatures.

	O 1s				**C 1s**	
	~ 530 eV	**~ 531 eV**	**~ 532 eV**	**~ 533 eV**	**~ 285 eV**	**~ 289 eV**
Sepiolite 600 °C		531.08	532.11	533.29	284.74	288.6
Sepiolite 750 °C	530.14	531.52		532.93	284.74	289.52
Sepiolite 900 °C	530.22	531.39		532.71	284.83	288.55

An investigation of the Si 2p spectra reveals that the Si 2p spectra of the geopolymer samples display two main features corresponding to Si bonding in Si–O–Mg and Si–O–Si environments [91].

The data presented in Table 3.2 and Table 3.4 points out that a shift in Mg 1s binding energy takes place upon alkali activation. This shift can be related to transition of octahedral Mg atoms to tetrahedral coordination [100], which was experimentally verified by ^{25}Mg MAS NMR spectroscopy in a previous study [58].

The data presented in Table 3.2 and Table 3.4 points out that a shift in Mg 1s binding energy takes place upon alkali activation. This shift can be related to transition of octahedral Mg atoms to tetrahedral coordination [100], which was experimentally verified by ^{25}Mg MAS NMR spectroscopy in a previous study [58].

The percentages of Si, O, Mg, Na and C elements obtained from XPS fittings are presented in Table 3.6.

Table 3.4. XPS Mg 1s, Si 2p and O 1s peak binding positions for SAAMs.

	Mg 1s		**Si 2p**		**O 1s**		
	~ 1303 eV	**~ 1300 eV**	**Si 2p3**	**Si 2p1**	**~ 531 eV**	**~ 532 eV**	**~ 536 eV**
SAAM-1	1303.98	1300.18	102.28	102.78	530.48	531.98	536.38
SAAM-2	1302.98		101.78	101.98	531.13	532.53	535.74
SAAM-3	1303.88	1300.38	102.48	103.18	530.48	532.08	536.38
SAAM-4	1303.68	1300.08	102.18	102.78	530.48	531.88	536.28
SAAM-5	1303.78	1299.98	102.38	103.08	530.68	531.78	536.18
SAAM-6	1303.48		101.78	102.48	530.56	531.45	535.23
SAAM-7	1303.78	1300.08	102.58	103.28	530.68	531.98	536.38
SAAM-8	1303.78	1300.08	102.38	103.08	530.68	531.88	536.28
SAAM-9	1303.28		102.08	102.78	530.79	531.42	535.29
SAAM-10	1303.18		102.08	102.78	530.89	532.3	535.42
SAAM-11	1303.38		102.18	102.88	530.83	532.22	535.44
SAAM-12	1303.78	1300.38	102.18	102.88	530.68	531.88	536.28
SAAM-13	1303.48		102.08	102.58	530.75	532.17	535.32
SAAM-14	1303.49		101.98	102.68	530.71	531.52	535.35
SAAM-15	1303.58		102.18	102.68	530.9	532.5	535.24
SAAM-16	1303.68		102.28	102.88	530.85	532.21	535.38
SAAM-17	1303.58		102.18	102.78	530.85	531.57	535.31
SAAM-18	1303.48		102.08	102.58	530.93	532.53	535.24
SAAM-19	1303.48		102.18	102.68	530.9	531.72	535.56
SAAM-20	1303.48		102.18	102.88	530.91	532.44	535.44

Table 3.5. XPS Na1s and C1s peak binding positions for SAAMs.

	Na 1s	**C 1s**	
	~ 1071 eV	**~ 285 eV**	**~ 288 eV**
SAAM-1	1071.63	284.83	287.8
SAAM-2	1071.02	284.52	288.78
SAAM-3	1071.77	284.84	288.04
SAAM-4	1071.55	284.86	288.09
SAAM-5	1071.67	284.81	288.65
SAAM-6	1071.01	284.53	288.94
SAAM-7	1071.62	284.84	288.09
SAAM-8	1071.67	284.87	288.15
SAAM-9	1070.83	284.5	289.03
SAAM-10	1071.09	284.54	288.74
SAAM-11	1071.04	284.5	288.65
SAAM-12	1071.7	284.83	288.04
SAAM-13	1070.97	284.52	288.86
SAAM-14	1070.91	284.55	288.86
SAAM-15	1071.03	284.51	288.79
SAAM-16	1071.02	284.52	288.73
SAAM-17	1071.09	284.55	288.83
SAAM-18	1070.98	284.53	288.77
SAAM-19	1071.15	284.51	288.69
SAAM-20	1071.1	284.52	288.7

Table 3.6. Atomic percentages Si, O, Mg, Na and C elements from XPS fittings.

	Si	**O**	**Mg**	**Na**	**C**
SAAM-1	27.79	36.13	8.66	6.54	18.45
SAAM-2	6.59	8.17	0.71	79.47	5.07
SAAM-3	30.25	34.99	5.91	5.84	20.56
SAAM-4	25.29	32.98	7.01	6.85	25.04
SAAM-5	18.72	36.16	6.28	10.28	25.82
SAAM-6	58.52	5.49	8.57	25.55	1.87
SAAM-7	28.71	32.90	4.85	5.51	25.92
SAAM-8	24.24	31.77	6.49	6.39	28.47
SAAM-9	26.75	7.73	1.42	59.68	4.42
SAAM-10	34.80	6.54	1.19	52.82	4.65
SAAM-11	48.96	5.43	3.00	39.73	2.89
SAAM-12	23.51	31.15	6.00	6.38	30.32
SAAM-13	5.53	13.60	3.81	68.46	8.61
SAAM-14	3.06	12.85	0.01	81.94	2.15
SAAM-15	38.79	6.82	4.86	45.93	3.60
SAAM-16	29.03	6.54	2.75	58.29	3.39
SAAM-17	42.29	6.97	7.55	40.02	3.17
SAAM-18	35.48	7.48	2.91	50.32	3.81
SAAM-19	54.00	5.25	6.51	31.64	2.60
SAAM-20	19.82	7.15	0.76	68.13	4.13

The data in Table 3.6 indicates that the atomic contents at the sample surface differ widely for different SAAMs. The surface characteristics are very important for the adsorption properties of the materials. The atomic content at the surface of the SAAMs along with the MB adsorption properties is investigated in more detail in Section 3.3.2.

The BET surface areas, pore volumes and average pore sizes of calcined sepiolite and SAAMs are given in Table 3.7 and Table 3.8.

Table 3.7. BET surface area, pore volume and pore size for calcined sepiolite.

	BET Surface Area (m^2/g)	**Pore Volume (cm^3/g)**	**Pore Size (Å)**
Sepiolite 600 °C	166.7	0.666	92.08
Sepiolite 750 °C	132.9	0.659	100.05
Sepiolite 900 °C	54.3	0.374	113.73

An investigation of Table 3.7 reveals that higher surface area values are observed with decreasing pore size. It is also seen that there is a slight decrease in surface area from 600 to 750 °C and a significant decrease at 900 °C.

The BET surface area, pore volume and the pore size results for SAAMs are presented in Table 3.8. The results in Table 3.8 indicate that the BET surface area of the SAAMs range between 4.5 and 28.6 m^2/g, with the highest surface area observed with SAAM-4. It is also seen in Table 3.8 that higher BET surface area values are observed for samples with higher pore volumes. In addition to that, a comparison between the results in Table 3.7 and Table 3.8 reveals that a significant decrease in surface area takes place upon alkali activation. This is in agreement with the findings from the studies of Kaya-Ozkiper et al., and Walczyk et al. [37], [92]. In the work by Walczyk et al., sepiolite was treated with NaOH to form loughlinite and a major decrease in the surface area of sepiolite was observed [92].

Table 3.8. BET surface area, pore volume and pore size for SAAMs.

	BET Surface Area (m^2/g)	**Pore Volume (cm^3/g)**	**Pore Size (Å)**
SAAM-1	15.3	0.024	29.54
SAAM-2	4.5	0.024	42.25
SAAM-3	8.0	0.006	28.31
SAAM-4	28.6	0.074	46.98
SAAM-5	7.4	0.029	43.43
SAAM-6	6.4	0.019	39.06
SAAM-7	4.9	0.005	35.88
SAAM-8	24.8	0.104	53.91
SAAM-9	7.8	0.015	41.08
SAAM-10	6.8	0.007	36.85
SAAM-11	5.5	0.006	33.04
SAAM-12	10.7	0.047	76.31
SAAM-13	12.9	0.018	47.71
SAAM-14	18.1	0.009	25.81
SAAM-15	6.6	0.026	42.97
SAAM-16	8.7	0.018	31.54
SAAM-17	17.0	0.025	36.93
SAAM-18	8.1	0.035	46.94
SAAM-19	14.5	0.019	33.74
SAAM-20	4.8	0.004	32.00

3.3.2. Methylene Blue Adsorption Tests

The methylene blue adsorption tests were conducted on 10 mg samples immersed in methylene blue with a concentration of 20 mg/L. The measurements were done at room temperature. The results obtained for different SAAM samples are given in Table 3.9.

The results in Table 3.9 indicate that the adsorption properties depend very much on the synthesis parameters. The adsorption capacity for SAAMs ranges between 4.78 to 110.42 mg/g. The highest adsorption capacity was observed for SAAM-4 with a value of 110.42 mg/g which was synthesized at a Na/Mg ratio of 1.3, pretreatment temperature of 750 °C and Si/Mg ratio of 2.5. The adsorption capacities of different SAAMs for MB removal is presented in Table 3.10.

An investigation of Table 3.10 reveals that the maximum uptake value of this study is higher than most of the alkali activated materials in literature. It is also observed from Table 3.10 that, although the adsorption properties of different alkali activated materials are widely studied, the mechanical properties of these materials are still somewhat less explored. The SAAMs of this study demonstrate a satisfactory performance in terms of both adsorption and mechanical properties.

Table 3.9. Methylene blue adsorption results for different geopolymer samples.

	Methylene Blue Uptake (mg MB dye/g adsorbent)
SAAM-1	97.67
SAAM-2	15.38
SAAM-3	56.33
SAAM-4	110.42
SAAM-5	70.50
SAAM-6	43.68
SAAM-7	65.78
SAAM-8	101.09
SAAM-9	54.76
SAAM-10	15.38
SAAM-11	4.78
SAAM-12	92.24
SAAM-13	86.25
SAAM-14	87.83
SAAM-15	66.72
SAAM-16	63.89
SAAM-17	84.68
SAAM-18	73.65
SAAM-19	98.43
SAAM-20	23.26

Table 3.10. MB adsorption capacity of different AAMs.

Material	**Adsorbent shape**	**mg/g**	**Compressive strength (MPa)**	**Reference**
Metakaolin geopolymer	powder	19.8	-	[130]
Coal fly ash waste	monolith	84	1.7	[48]
Nano copper oxide coated metakaolin geopolymer	monolith	14.4	45.6	[44]
Nano copper oxide coated metakaolin geopolymer	powder	87.2	-	[44]
Metakaolin geopolymer	monolith	3.4	20.4	[131]
Metakaolin geopolymer with 50% replacement of metakaolin with expanded glass	monolith	4.9	1.6	[131]
Metakaolin geopolymer	powder	43.48	-	[124]
Biomass fly ash geopolymer	cylindrical monolith	15.4	-	[47]
Fly ash geopolymer	spheres (d=2,6 mm)	30.1	-	[46]
Pyrophyllite clay-derived geopolymer	powder	64.1	-	[132]
Fly ash geopolymer	monolith	50.7	0.55	[133]
Fly ash geopolymer	powder	37.04	-	[134]
Sepiolite geopolymer	powder	99.92	40	[37]
This study	powder	4.78 - 110.42	1.5 - 135.5	

The XPS atomic percentage data presented in Table 3.6 is used to investigate the relationship between the surface characteristics and the adsorption capacity. The change of adsorption capacity with respect to the amounts of Mg, Na and O atoms is given in Figure 3.4 to Figure 3.6.

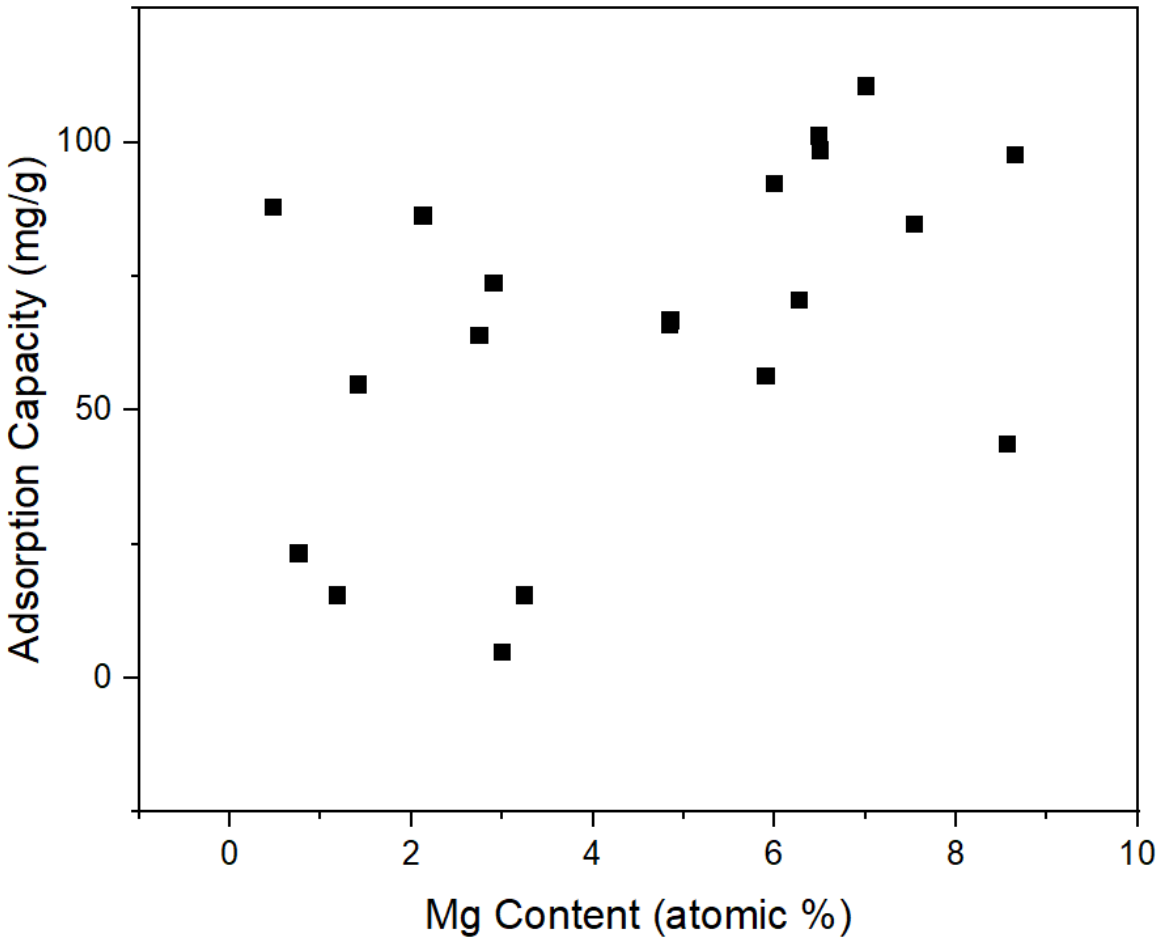

Figure 3.4. The change in adsorption capacity with Mg content at the sample surface.

An investigation of Figure 3.4 to Figure 3.6 reveals that Mg and O content at the surface has a positive impact while Na content seem to have a negative impact on the MB adsorption properties. The photocatalytic reaction mechanism for a fly ash geopolymer was previously described by Zhang and Liu [135]. They proposed that the MB dye molecules first ionize to cations in aqueous solution and the cations are then adsorbed by the negatively charged $[AlO_4]^{-5}$ tetrahedron. The metal oxide particles in the fly ash are irradiated by UV and the transition metal ions combine with H2O molecules to produce hydroxyl radicals. In the final step, the cations of MB adsorbed on the geopolymer framework are oxidized by hydroxyl radicals to form the degradation products [135].

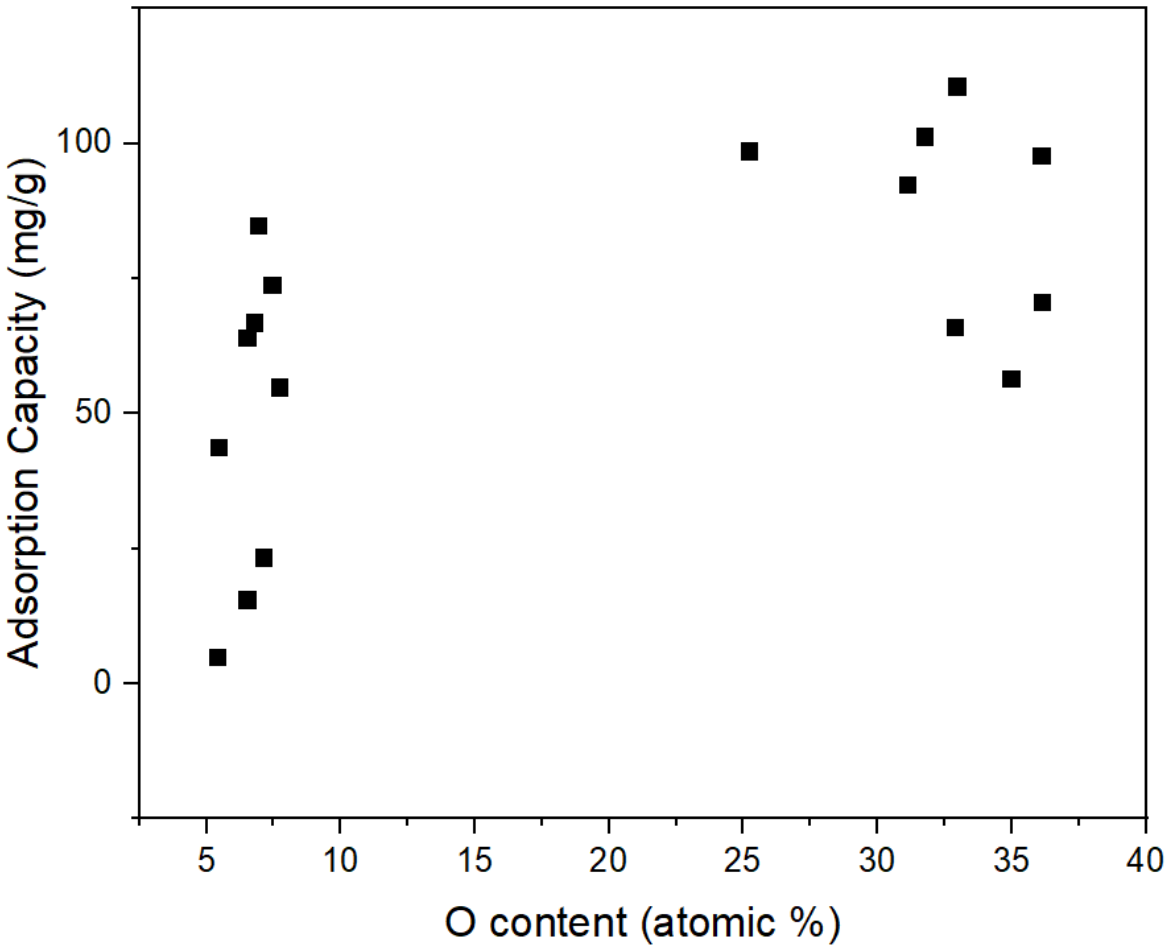

Figure 3.5. The change in adsorption capacity with O content at the sample surface.

The results presented in Figure 3.4 to 3.6 are in agreement with the mechanism proposed by Zhang and Liu. Considering that the SAAMs of this work are Mg counterparts of the fly ash geopolymers, it is possible that the increase in the Mg content results in a higher concentration of negatively charged counterparts of $[AlO_4]^{-5}$ tetrahedron. It is known from previous studies that surface hydroxyl groups enhance the MB adsorption properties of the SAAMs with their negative charges [37]. The high amount of oxygen at the surface of is an indication of higher surface hydroxyl groups and this might explain the positive correlation between the oxygen content and MB adsorption results of this study.

Sodium acts as a charge-balancing agent in the geopolymer structure. The presence of positive ions such as Na^+, K^+ are necessary to balance the negative charge of aluminum [16], [136]. The presence of higher amounts of Na at the surface might be an indication that Na^+

cations and MB dye cations produced in the first step of the photocatalysis reaction are in competition. This might explain the negative correlation between the Na content and the MB adsorption capacity.

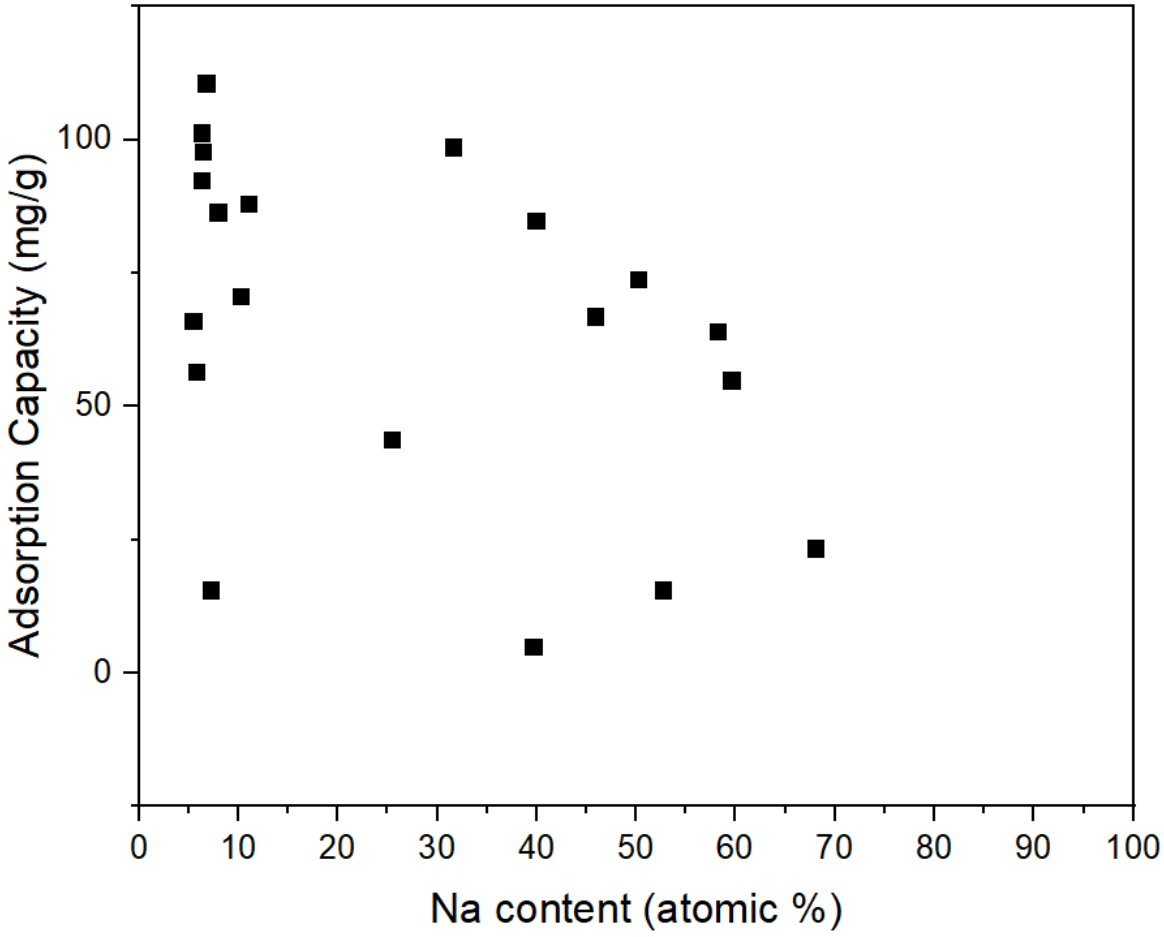

Figure 3.6. The change in adsorption capacity with Na content at the sample surface.

The adsorption properties of the SAAMs were analyzed by response surface methodology. A response surface regression with backward elimination was used to have a predictive tool for the methylene blue uptake based on the synthesis parameters. Analysis of variance (ANOVA) was used to investigate the significance of the model compared to residual error. The non-significant linear terms are added to the model to maintain the model hierarchy. The results of the ANOVA table for the adsorption capacity of SAAMs are given in Table 3.11.

It is seen in Table 3.11 that the values for the correlation coefficient (R^2) and adjusted R^2 were 0.865 and 0.802 respectively. These values indicate that the model and the data fit well and the predictions made by the model can be used for the prediction of the performance in the range that is chosen. Looking at Table 3.11, it is seen that the model is significant at the 95% confidence level with a p-value < 0.05. Temperature, Na/Mg Ratio*Na/Mg Ratio, Temperature*Temperature and Si/Mg Ratio*Si/Mg Ratio are the terms that are significant with a p-value less than 0.05. The impacts of the different parameters are compared by making use of the F-values given in Table 3.11 F-value is the ratio of the mean square for the individual term to the mean square for the residual. The results in Table 3.11 indicate that Temperature*Temperature with an F-value of 41.16 has the highest impact, while Na/Mg ratio with an F-value of 0.26 has the lowest impact on the MB adsorption of the SAAMs. Lack of fit is an important parameter to take into account while determining the adequacy of a model. The p-value of the lack of fit is found to be 0.054, which indicates that the lack of fit is not significant and the model is adequate. The graph between the residuals and the probability is given in Figure 3.7 and it verifies the assumption that the model errors are normally distributed.

The contour plots for the adsorption properties against synthesis parameters are given in Figure 3.8-3.10. From Figure 3.8, it is seen that higher adsorption capacity can be achieved with a Temperature in the range from 675 – 725 °C and Na/Mg ratio between 1.2-1.4. Higher adsorption capacities are observed for Si/Mg ratio between 2.2- 2.6 and Temperature between 675-725 °C as seen in Figure 3.9. From Figure 3.10, higher adsorption values are seen at a much wider range of Si/Mg and Na/Mg ratios at a Temperature of 750 °C with the ranges being 2.0-2.8 and 1.2-1.4 respectively.

Table 3.11. ANOVA results for adsorption capacity.

Source	DF	Adj SS	Adj MS	F-Value	P-Value
Model	6	16155.7	2692.61	13.86	0.000
Linear	3	4279.6	1426.53	7.34	0.004
Na/Mg Ratio	1	51.4	51.39	0.26	0.616
Temperature	1	4103.9	4103.93	21.12	0.001
Si/Mg Ratio	1	124.2	124.25	0.64	0.438
Square	3	11876.1	3958.70	20.38	0.000
Na/Mg Ratio*Na/Mg Ratio	1	3537.8	3537.76	18.21	0.001
Temperature*Temperature	1	7996.1	7996.14	41.16	0.000
Si/Mg Ratio*Si/Mg Ratio	1	1182.6	1182.63	6.09	0.028
Error	13	2525.8	194.29		
Lack-of-Fit	8	2225.1	278.13	4.62	0.054
Pure Error	5	300.7	60.15		
Total	19	18681.5			
R^2	0.865				
Adjusted R^2	0.802				

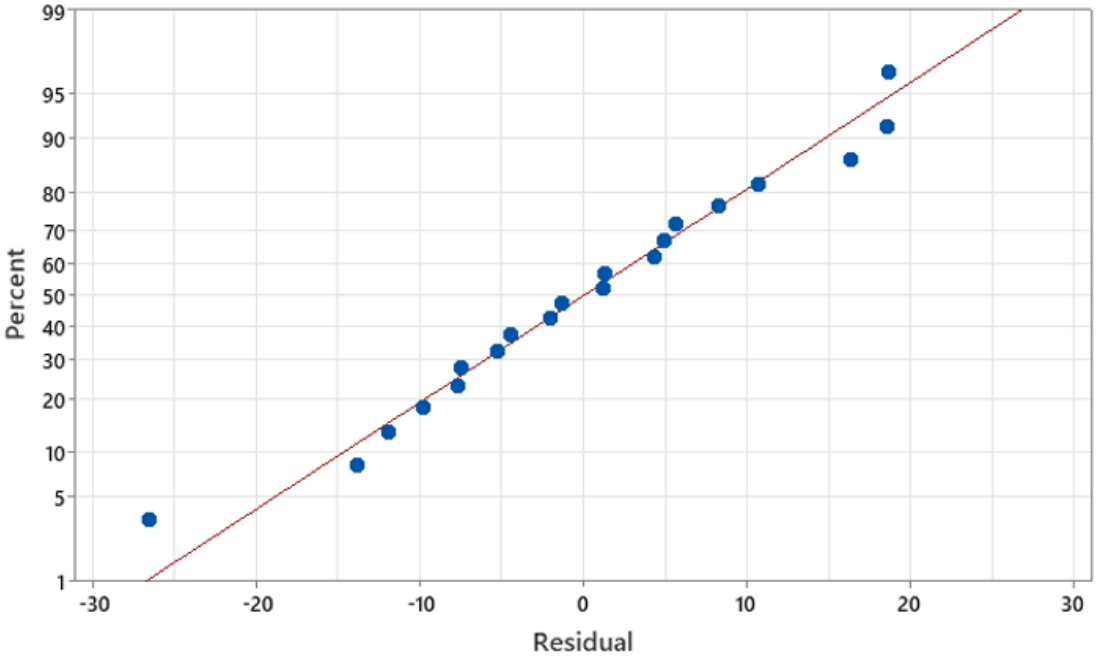

Figure 3.7. Normal probability plot of SAAMs.

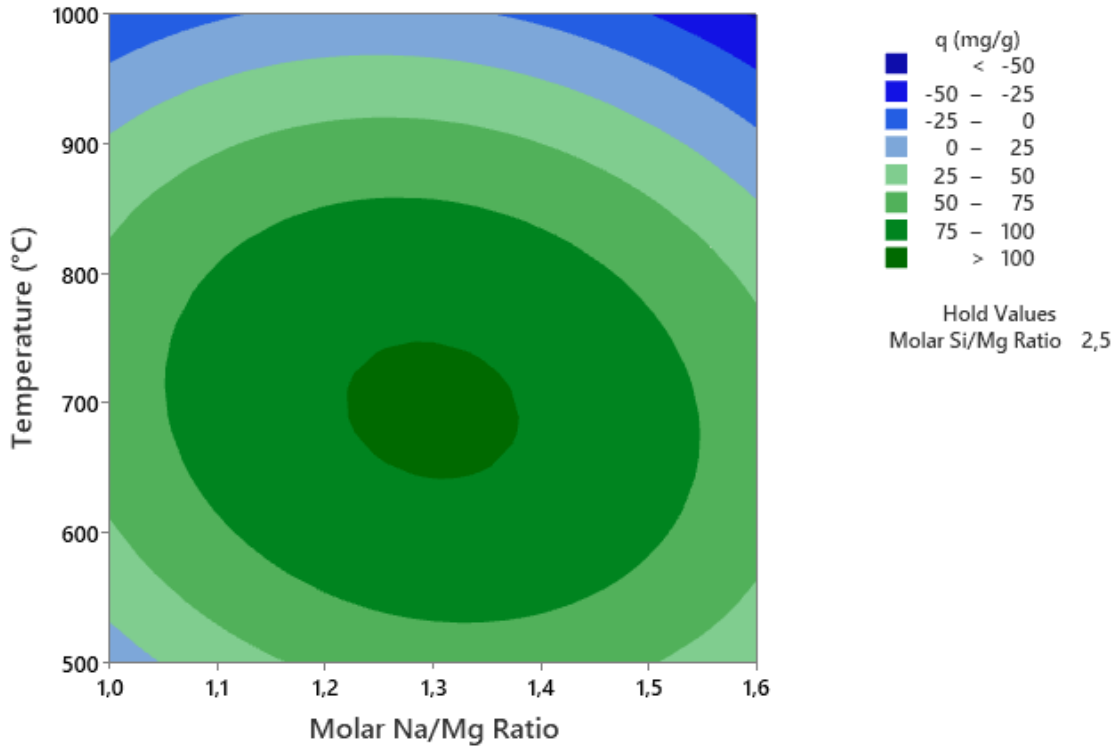

Figure 3.8. Contour plot showing the effects of Temperature and Na/Mg ratio at Si/Mg Ratio=2.5.

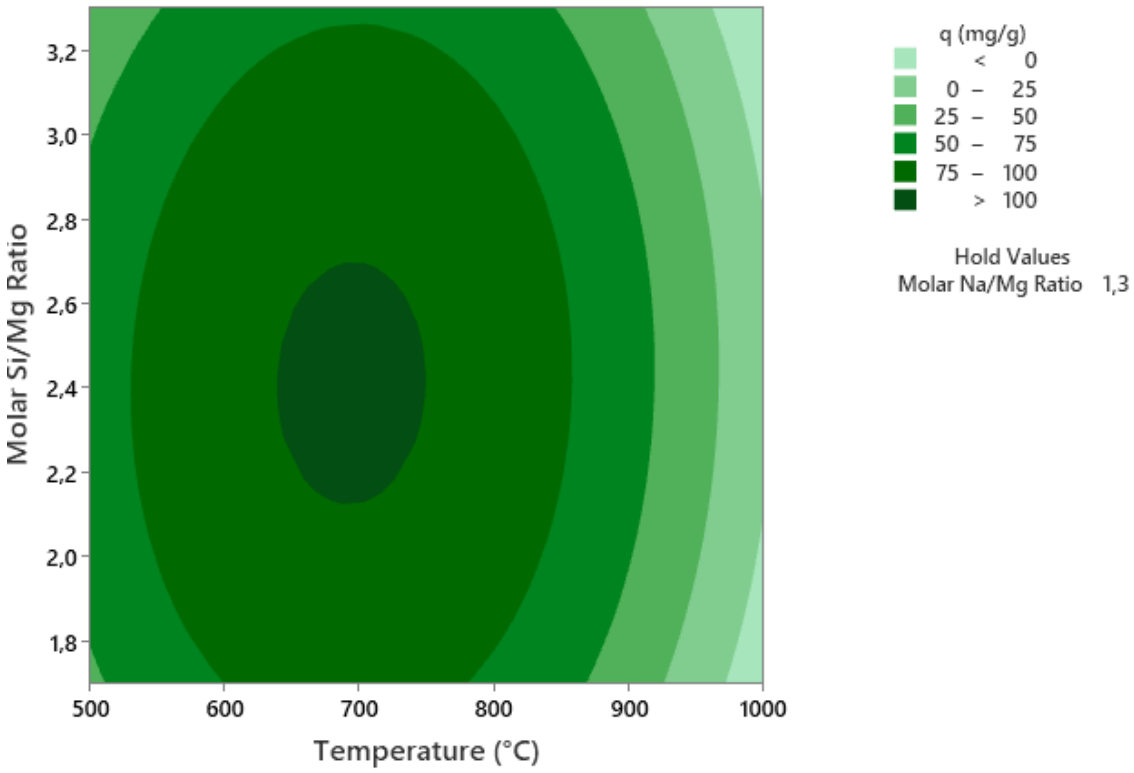

Figure 3.9. Contour plot showing the effects of Temperature and Si/Mg ratio at Na/Mg Ratio=1.3.

The effects of different synthesis parameters are investigated by making use of the coded coefficients from the model. Coded units are useful to determine the factors that have the largest impact and whether each factor has a positive or negative effect on the parameter of interest. The model in terms of the coded variables is given as:

$$MB\ Adsorption = 99.73 - 3.04*Na/Mg\ Ratio - 29.00*\ Temperature - 4.92*\ Si/Mg\ Ratio - 41.71*\ (Na/Mg\ Ratio)^2 - 66.00*\ (Temperature)^2 - 25.00*\ (Si/Mg\ Ratio)^2. \quad (3.4)$$

Based on the obtained model, a multiple response prediction is done to determine the optimum synthesis conditions for highest MB adsorption performance. The results of this study indicated that the optimum values for Na/Mg Ratio, Temperature and Si/Mg Ratio are 1.3, 697 °C, and 2.4, respectively.

The source of Na in the geopolymer formulations is sodium hydroxide. Sodium hydroxide is known to enhance the dissolution of silicate and aluminosilicate minerals in aqueous

systems [59]. Sodium hydroxide consists of Na+ and OH- ions. During geopolymerization reactions, OH- anions attack the Si-O-T bonds in the raw material and produce Si-O bonds [137]. Once the first bond is ruptured, the silanol groups deprotonate and the charge is balanced by the alkali cation [59]. The optimum value of 1.3 obtained from the model indicates that increasing the Na/Mg ratio to some extent has a positive effect on the MB adsorption properties and beyond the optimum value, further increases results in decreased performance. The reason for such a behavior might be that increasing Na/Mg ratios beyond a certain value can result in a decrease in the porosity of the geopolymer due to an increase in the setting time of the geopolymer [50].

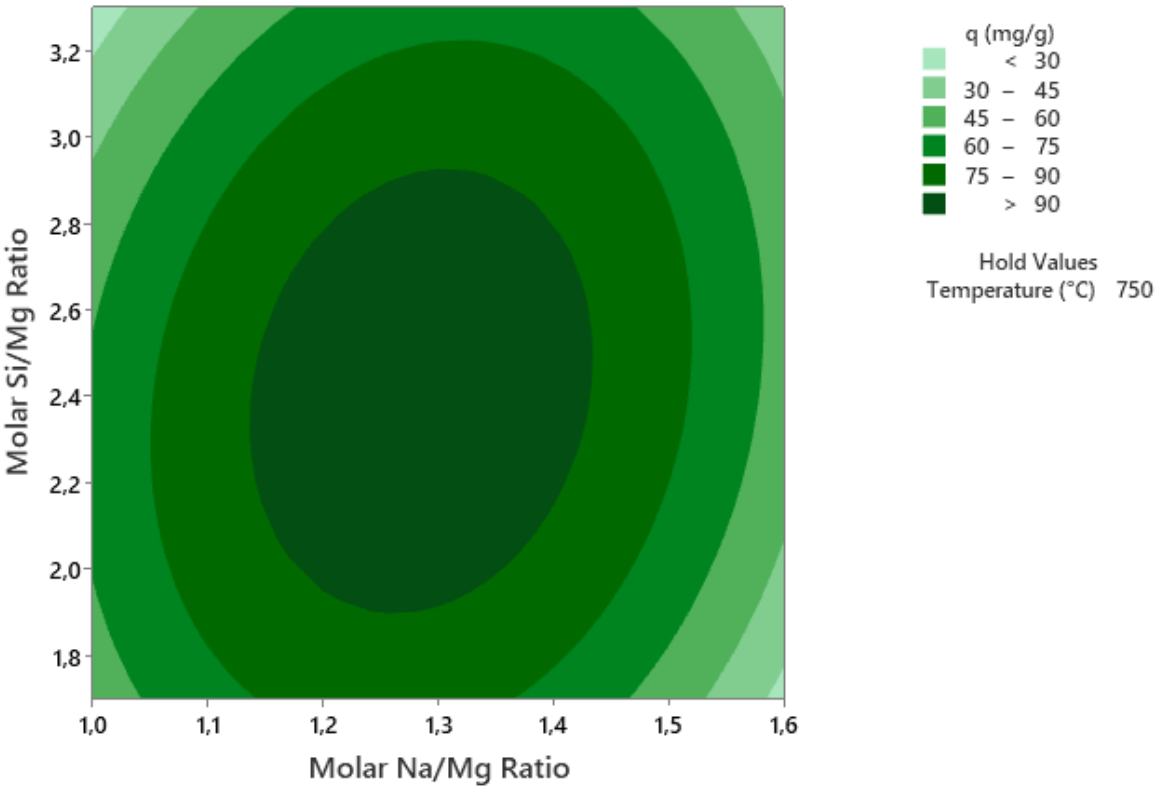

Figure 3.10. Contour plot showing the effects of Si/Mg ratio and Na/Mg ratio at a temperature of 750 °C.

It is seen from Equation (3.4) that temperature has the most impact and is inversely correlated with the MB adsorption capacity. From previous studies, it is known that the water molecules coordinated to Mg are lost from the structure of sepiolite up to a temperature of 500 °C and after this temperature the structure starts to fold. The decrease in the adsorption

properties can be explained by the channels becoming narrower and the superficial slots sintering [138]. These findings are verified by the BET data surface area results presented in Table 3.8.

The optimum value of Si/Mg molar ratio for high MB adsorption performance is found to be around 2.4 from the obtained model. Geopolymerization reactions involve dissolution, hydrolysis and condensation steps. It is reported in previous studies that silica content has a major role in the geopolymerization reactions of aluminosilicate containing raw materials. Depending on the silica content, the condensation reactions take place between aluminate and silicate species or silicate species themselves [139] and it is reported in previous studies that the rate of condensation between silicate species is slower than that of between silicate and aluminate species [140]. The availability of silicate increases the rate of reaction, which might explain the increase in the MB adsorption properties up to an optimum Si/Mg molar ratio. Beyond this optimum value, further increases in the Si/Mg ratio may decrease the porosity of the SAAM by blocking the pores, which might result in a decrease in the MB adsorption capacity [50]. Similar observations were made with aluminosilicate counterparts of the sepiolite AAMs, such as the work by Duxson et al., where they observed that the pore volume and the adsorption capacity decrease with increasing Si/Al ratio [16].

In addition to these studies, a model is generated for the estimation of the BET surface area. For this purpose, the synthesis parameters are used as input. A response surface model with backward elimination is generated. A summary of the generated model is given in Table 3.12.

Table 3.12. Summary of the BET surface area model.

	DF	Adj SS	Adj MS	F-Value	P-Value
Model	4	578.084	144.521	7.35	0.002
Linear	2	9.733	4.867	0.25	0.784
Na/Mg Ratio	1	0.146	0.146	0.01	0.933
Temperature	1	9.587	9.587	0.49	0.496
Square	2	568.351	284.176	14.45	0.000
Na/Mg Ratio*Na/Mg Ratio	1	304.895	304.895	15.50	0.001
Temperature*Temperature	1	285.588	285.588	14.52	0.002
Error	15	295.078	19.672		
Lack-of-Fit	10	66.304	6.630	0.14	0.995
Pure Error	5	228.773	45.755		
Total	19	873.162			
R^2	66.21				
Adjusted R^2	57.19				

The R^2 value of the model is found to be 0.66, which indicates that the model and the experimental data moderately fit. The p-value for the lack of fit is found to be > 0.05 which means that it is not significant and contributes to the adequacy of the model. One observation with the model is that there are some large residuals for some of the results. This might indicate a need to transform the output variable. For this investigation, a new model is constructed by using $1/\sqrt{BET\ surface\ area}$ as the output variable. The summary of the new model is given in Table 3.13.

Table 3.13. Summary of the revised BET surface area model.

Source	DF	Adj SS	Adj MS	F-Value	P-Value
Model	4	0.110	0.028	13.65	0.000
Linear	2	0.009	0.004	2.13	0.153
Na/Mg Ratio	1	0.000	0.000	0.01	0.914
Temperature	1	0.009	0.009	4.25	0.057
Square	2	0.102	0.051	25.16	0.000
Na/Mg Ratio*Na/Mg Ratio	1	0.049	0.049	24.11	0.000
Temperature*Temperature	1	0.057	0.057	28.17	0.000
Error	15	0.030	0.002		
Lack-of-Fit	10	0.021	0.002	1.10	0.486
Pure Error	5	0.009	0.002		
Total	19	0.141			
R^2	78.45				
Adjusted R^2	72.70				

An investigation of Table 3.13 reveals that the R^2 value improved significantly with the new model. In addition to that, the p-value of the lack of fit is > 0.05, which means that the model is adequate. In addition to these, no large residuals are observed for the new model, which indicates the validity of the model. The normal distribution plot is presented in Figure 3.11. The results indicate that there is not a large deviation from the normal distribution. Considering all these, it can be concluded that the model is valid and can be used in the prediction of BET surface area over the synthesis conditions that was used in this study.

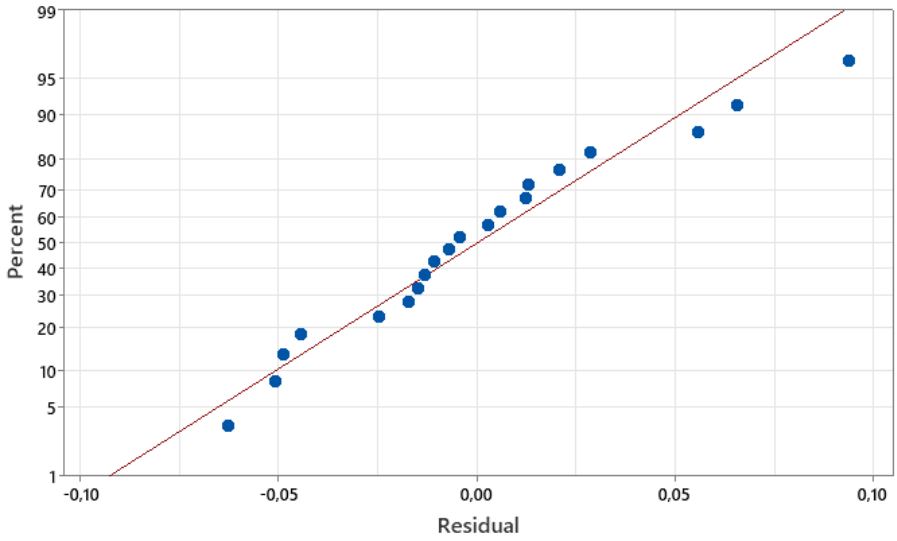

Figure 3.11. Normal distribution plot for revised BET surfaec area model.

The synthesis conditions that maximize the BET surface area are determined by the obtained model. According to the model, a molar Na/Mg ratio around 1.3 and a treatment temperature around 720 °C maximizes the BET surface area. The molar Na/Mg ratio of 1.3 indicates that above a threshold value, the presence of excess Na results in a decrease in the surface area. This observation was previously made with aluminosilicate geopolymers [50]. In this study, it was stated that increase of Na in the system beyond a certain point results in a longer setting time, which causes a decrease in porosity of the geopolymer [50]. In addition to that, it is seen that increasing temperature has a negative impact on the surface area. It can be related to the folding of the structure by the removal of Mg-coordinated water upon heating.

In addition to these studies, the possibility to generate a model to estimate MB adsorption capacity by using the XPS results and BET results as input is investigated. For this purpose, the atomic percentages of Si, Na, O and Mg at the surface along with the shift in binding energies for Mg 1s, Si 2p1, Si 2p3 and O 1s and BET surface area data is fed to the model. Backward elimination is used for the generation of the model. The obtained results are presented in Table 3.14.

Table 3.14. Modeling results for MB adsorption.

Source	DF	Adj SS	Adj MS	F-Value	P-Value
Regression	4	14669	3667.2	22.64	0.000
Si content (at. %)	1	6458	6458.1	39.88	0.000
Mg content (at. %)	1	5757	5757.3	35.55	0.000
Delta Si 2p3 (eV)	1	2011	2010.7	12.42	0.004
Delta Si 2p1 (ev)	1	6455	6455.3	39.86	0.000
Error	13	2105	161.9		
Total	17	16774			
R^2	87.45				
Adjusted R^2	83.59				

An investigation of Table 3.14 reveals that a model containing both atomic percent data and the shift in binding energy is obtained. The R^2 value around 0.87 indicates good fit between the experimental results and the model. Since the model only contains XPS data, the model makes it possible to estimate the MB adsorption properties of SAAM by XPS data.

3.3.3. Compressive Strength Measurements

In this Chapter, MB adsorbance performance of different SAAMs were investigated. The results indicated that with a MB uptake value of 110.42 mg/g, SAAM-4 displayed the best performance as an adsorbent. The compressive strength results for the SAAMs were given in Table 2.4. The compressive strength value of SAAM-4 was found to be 43.8 MPa. Considering the adsorbance performance along with the compressive strength values, it is seen that a novel material with very good adsorbent properties and satisfactory mechanical strength is synthesized and these materials can be considered as sustainable and innovative options for the removal of dye from wastewater.

3.4. Conclusions

The effects of different synthesis parameters on MB adsorption capacities of sepiolite-based AAMs are studied for the first time in literature. The results indicated that the AAM that is synthesized using sepiolite treated at 750 °C with a molar Si/Mg ratio of 2.5 and molar Na/Mg ratio of 1.3 displayed the highest MB adsorption capacity. The highest obtained capacity of 110.42 mg/g can be considered as a benchmark value for the materials that are used for this purpose. The adsorption data fitted well with the quadratic model with a correlation coefficient (R^2) of 0.865. The optimum values of molar Na/Mg Ratio, temperature and molar Si/Mg Ratio are found to be 1.3, 697 °C and 2.4, respectively for higher MB adsorption performance. It is observed from the BET analysis that samples with higher surface area have better MB adsorption properties, while the XPS results indicated that the amount of Mg, O and Na atoms at the sample surface has a major impact on the adsorption properties. It was observed that an increase in the amount of Mg and O at the sample surface resulted in higher adsorption capacities, possibly due to their negative charges that make it easier to be adsorbed for the positively charged MB. The mechanical strength of the SAAMs are also investigated for a more thorough investigation of the possible use of the material in real life cases. The results indicated that SAAMs displayed remarkable compressive strength values and they can be considered as sustainable and innovative options for the removal of dye from wastewater.

4. CONCLUSIONS AND RECOMMENDATIONS

4.1. Conclusions

In this thesis, the main motivation is to investigate the effects of synthesis parameters and formation kinetics on the structure, mechanical performance and methylene blue (MB) adsorption properties of alkali activated magnesium silicates. The compressive strength, MB removal performance, and the effects of the structures of the materials on these properties were investigated using different characterization techniques. Time- variant FTIR data is collected to shed light on the kinetics of geopolymerization and the impacts of reaction kinetics on mechanical performance.

In Chapter 2, an in-depth analysis of the effects of synthesis parameters on the compressive strength of SAAMs is studied. Compressive strength values ranging from 1.5 to 135.5 MPa were obtained, indicating the huge impact of synthesis conditions on the properties of the AAMs. The results of the study demonstrated that increasing pretreatment temperature has a negative impact, while increasing Si/Mg ratio has a positive impact on the compressive strength of the materials. The raw materials and the SAAMs are characterized by XRF, XRD, TGA and XPS. The comparison of the XRD patterns of the SAAMs and the calcined sepiolite samples demonstrate that there is a significant decline in crystalline phase upon alkali activation. The TGA results point out that the thermal stability of the SAAMs are high and the weight loss values decrease with increasing sepiolite pretreatment temperature, as expected. An investigation of the XPS results together with the compressive strength results indicated that a shift in the peak binding energy of Mg 1s spectra is correlated with the compressive strength results. The shift in Mg 1s binding energy can be an indication of the transition of octahedral Mg atoms into tetrahedral coordination. This shift takes place as a result of geopolymerization reactions and indicates a higher degree of geopolymerization, thus higher compressive strength results. The relation between the reaction kinetics and the compressive strength is investigated by collecting FTIR data at different reaction times. The relation is quantified by fitting an exponential function to the

position of the main FTIR feature over time. The results demonstrated that a higher compressive strength is obtained for samples for which the shift in FTIR peak position takes place at the early stage and in a more rapid pace. This result is a clear indication that early geopolymerization is a big contributor to the compressive strength.

In Chapter 3, the effects of different synthesis parameters on MB adsorption capacities of SAAMs are studied. The results indicated that the AAM that is synthesized using sepiolite treated at 750 °C with a Si/Mg ratio of 2.5 and Na/Mg ratio of 1.3 displayed the highest MB adsorption capacity. The highest obtained capacity of 110.42 mg/g can be considered as a benchmark value for the materials that are used for this purpose. The adsorption data fitted well with the quadratic model with a correlation coefficient (R^2) of 0.865. The optimum values of Na/Mg Ratio, Temperature and Si/Mg Ratio are found to be 1.3, 697 °C and 2.4, respectively for higher MB adsorption performance. It is observed from the BET analysis that samples with higher surface area have better MB adsorption properties. XPS results indicated that the amount of Mg, O and Na atoms at the sample surface has a major impact on the adsorption properties. It was observed that an increase in the amount of Mg and O at the sample surface resulted in higher adsorption capacities, possibly due to their negative charges that make it easier to be adsorbed for the positively charged MB. The mechanical strength of the AAMs are also discussed for a more thorough investigation of the possible use of the material in real life cases. The results indicated that AAMs displayed high compressive strength values and they can be considered as sustainable and innovative options for the removal of dye from wastewater.

These results shows that sepiolite, which is a cheap and abundant material, can be used for the production of environmentally friendly construction materials with high performance as an adsorbent for MB removal. It is also demonstrated that the mechanical strength and the MB adsorption performance of the materials can be tuned by the synthesis parameters, making these materials suitable for different construction and wastewater treatment applications.

4.2. Recommendations

In this thesis, SAAMs are studied to understand their potential applications as a construction material and adsorbent. For future studies, the following points can be considered. In Chapter 2, the effects of synthesis conditions on the structure and mechanical properties is investigated in detail. The kinetics of geopolymerization reactions were monitored and the effects of the kinetics on the mechanical strength is studied in detail. The temperature range of this study was too wide for the generation of a predictive model for the estimation of compressive strength based on synthesis conditions. As a further study, a predictive model based on the synthesis conditions can be generated by choosing a temperature range this is much narrower and collecting compressive strength data with these synthesis conditions.

In Chapter 3, it was shown that SAAMs have a huge potential as an adsorbent for the removal of MB dye. The MB removal performance of the SAAM can be further studied with the incorporation of other materials (such as anatase) to make use of the combined effects of adsorption and photocatalysis for MB removal.

In this study, sepiolite is used as the raw material. Sepiolite is a cheap and abundant material. However, the studies can be furthered with other waste materials, such as fly and blast furnace slag. Their mechanical performance along with their potential as an adsorbent can be evaluated to get a deeper understanding on the effects of raw materials. This would also support a sustainable world by making use of waste materials and contributing to circular economy.

REFERENCES

1. Shaikh, F. U. A., "Mechanical and Durability Properties of Fly Ash Geopolymer Concrete Containing Recycled Coarse Aggregates", *International Journal of Sustainable Built Environment*, Vol. 5, No. 2, pp. 277–287, 2016.

2. Almutairi A. L., B. A. Tayeh, A. Adesina, H. F. Isleem, and A. M. Zeyad, "Potential Applications of Geopolymer Concrete in Construction: A Review", *Case Studies in Construction Materials*, Vol. 15, p. 00733, 2021.

3. Amran, Y. H. M., R. Alyousef, H. Alabduljabbar, and M. El-Zeadani, "Clean Production and Properties of Geopolymer Concrete; A review", *Journal of Cleaner Production*, Vol. 251, p. 119679, 2020.

4. Amran, M., N. Makul, R. Fediuk, Y. H. Lee, N. I. Vatin, Y. Y. Lee and K. Mohammed, "Global Carbon Recoverability Experiences from the Cement Industry", *Case Studies in Construction Materials*, Vol. 17, p. 1439, 2023.

5. Segura, I. P., N. Ranjbar, A. J. Damo, L. S. Jensen, M. Canut and P. A. Jensen, "A Review: Alkali-Activated Cement and Concrete Production Technologies Available in the Industry", *Heliyon*, Vol. 9, p. 15718, 2023.

6. Provis, J. L., "Alkali-Activated Materials", *Cement and Concrete Research*, Vol. 114, pp. 40–48, 2018.

7. Provis, J. L. and S. A. Bernal, "Geopolymers and Related Alkali-Activated Materials", *Annual Review of Material Research*, Vol. 44, pp. 299–327, 2014.

8. Davidovits, J., "Geopolymers Inorganic Polymeric New Materials", *Journal of Thermal Analysis*, Vol. 37, pp. 1633-1656, 1991.

9. Arunachelam, N., J. Maheswaran, M. Chellapandian, G. Murali, and N. I. Vatin, "Development of High-Strength Geopolymer Concrete Incorporating High-Volume Copper Slag and Micro Silica", *Sustainability*, Vol. 14, No. 13, p.7601, 2022.

10. Tayeh, B. A., A. M. Zeyad, I. S. Agwa, and M. Amin, "Effect of Elevated Temperatures on Mechanical Properties of Lightweight Geopolymer Concrete", *Case Studies in Construction Materials*, Vol. 15, p. 673, 2021.

11. Komkova, A. and G. Habert, "Environmental Impact Assessment of Alkali-Activated Materials: Examining Impacts of Variability in Constituent Production Processes and Transportation", *Construction and Building Materials*, Vol. 363, p.129032, 2023.

12. Zhang, M., T. El-Korchi, G. Zhang, J. Liang, and M. Tao, "Synthesis Factors Affecting Mechanical Properties, Microstructure, and Chemical Composition of Red Mud-Fly Ash Based Geopolymers", *Fuel*, Vol. 134, pp. 315–325, 2014.

13. Provis, J. L. and J. S. J. Van Deventer, "Direct Measurement of the Kinetics of Geopolymerisation by in-situ Energy Dispersive X-ray Diffractometry", *Journal of Material Science*, Vol. 42, No. 9, pp. 2974–2981, 2007.

14. Duxson, P., A. Fernández-Jiménez, J. L. Provis, G. C. Lukey, A. Palomo, and J. S. J. Van Deventer, "Geopolymer Technology: The Current State of the Art", *Journal of Material Science*, Vol. 42, No. 9, pp. 2917–2933, 2007.

15. Castillo, H., H. Collado, T. Droguett, S. Sanchez, "Factors Affecting the Compressive Strength of Geopolymers: A Review", *Minerals*, Vol. 11, No. 12, p. 1317, 2021.

16. Duxson, P., J. L. Provis, G. C. Lukey, S. W. Mallicoat, W. M. Kriven, and J. S. J. Van Deventer, "Understanding the Relationship Between Geopolymer Composition, Microstructure and Mechanical Properties", *Colloids Surfaces A: Physicochemical Engineering Aspects*, Vol. 269, No. 1–3, pp. 47–58, 2005.

17. Ozer, I. and S. Soyer-Uzun, “Relations Between the Structural Characteristics and Compressive Strength in Metakaolin Based Geopolymers with Different Molar Si/Al Ratios”, *Ceramics International*, Vol. 41, No. 8, pp. 10192–10198, 2015.

18. Lahoti, M., P. Narang, K. H. Tan, and E. H. Yang, “Mix Design Factors and Strength Prediction of Metakaolin-Based Geopolymer”, *Ceramics International*, Vol. 43, No. 14, pp. 11433–11441, 2017.

19. Muracchioli, M., G. Menardi, M. D’Agostini, G. Franchin, and P. Colombo, “Modeling the Compressive Strength of Metakaolin-Based Geopolymers Based on the Statistical Analysis of Experimental Data”, *Applied Clay Science*, Vol. 242, p. 107020, 2023.

20. Alterary, S. S. and N. H. Marei, “Fly Ash Properties, Characterization, and Applications: A Review”, *Journal of King Saud University - Science*, Vol. 33, No. 6, p. 101536, 2021.

21. Leelarungroj, K., S. Likitlersuang, T. Chompoorat, and and D. Janjaroen, “Leaching Mechanisms of Heavy Metals from Fly Ash Stabilised Soils”, *Waste Management & Research*, Vol. 36, No. 7, pp. 616–623, 2018.

22. Shekhawat, P., G. Sharma, and R. M. Singh, “A Comprehensive Review of Development and Properties of Flyash-Based Geopolymer as a Sustainable Construction Material”, *Geotechnical and Geological Engineering*, Vol. 40, No. 11, pp. 5607–5629, 2022.

23. Fernández-Jiménez, A. and A. Palomo, “Composition and Microstructure of Alkali Activated Fly Ash Binder: Effect of the Activator”, *Cement and Concrete Research*, Vol. 35, No. 10, pp. 1984–1992, 2005.

24. Ryu, G. S., Y. B. Lee, K. T. Koh, and Y. S. Chung, “The Mechanical Properties of Fly Ash-Based Geopolymer Concrete with Alkaline Activators”, *Construction Building Materials*, Vol. 47, pp. 409–418, 2013.

25. Rees, C. A., J. L. Provis, G. C. Lukey, and J. S. J. Van Deventer, “In situ ATR-FTIR Study of the Early Stages of Fly Ash Geopolymer Gel Formation”, *Langmuir*, Vol. 23, No. 17, pp. 9076–9082, 2007.

26. Hadi, M. N. S., M. Al-Azzawi, and T. Yu, “Effects of Fly Ash Characteristics and Alkaline Activator Components on Compressive Strength of Fly Ash-Based Geopolymer Mortar”, *Construction Building Materials*, Vol. 175, pp. 41–54, 2018.

27. de Oliveira, L. B., A. R. G. de Azevedo, M. T. Marvila, E. C. Pereira, R. Fediuk, and C. M. F. Vieira, “Durability of Geopolymers with Industrial Waste”, *Case Studies in Construction Materials*, Vol. 16, p. 00839, 2022.

28. Aziz, I. H., M. M. A. B. Abdullah, M. A. A. Mohd Salleh, E. A. Azimi, J. Chaiprapa, and A. V. Sandu, “Strength Development of Solely Ground Granulated Blast Furnace Slag Geopolymers”, *Construction Building Materials*, Vol. 250, p. 118720, 2020.

29. Mallikarjuna Rao G. and T. D. Gunneswara Rao, “Final Setting Time and Compressive Strength of Fly Ash and GGBS-Based Geopolymer Paste and Mortar”, *Arabian Journal for Science and Engineering*, Vol. 40, No. 11, pp. 3067–3074, 2015.

30. Yurt, Ü., “High Performance Cementless Composites from Alkali Activated GGBFS”, *Construction and Building Materials*, Vol. 264, p. 120222, 2020.

31. Kaya K. and S. Soyer-Uzun, “Evolution of Structural Characteristics and Compressive Strength in Red Mud-Metakaolin Based Geopolymer Systems”, *Ceramics International*, Vol. 42, No. 6, pp. 7406–7413, 2016.

32. Aouan, B., S. Alehyen, M. Fadil, M. El Alouani, H. Saufi, and M. Taibi, "Characteristics, Microstructures, and Optimization of the Geopolymer Paste Based on Three Aluminosilicate Materials Using a Mixture Design Methodology", *Construction and Building Materials*, Vol. 384, p. 131475, 2023.

33. Yi, Y., M. Liska, and A. Al-Tabbaa, "Properties and Microstructure of GGBS–Magnesia Pastes", *Advances in Cement Research*, Vol. 26, No. 2, pp. 114–122, 2014.

34. Abdalqader, A. F., F. Jin, and A. Al-Tabbaa, "Characterisation of Reactive Magnesia and Sodium Carbonate-Activated Fly Ash/Slag Paste Blends", *Construction and Building Materials*, Vol. 93, pp. 506–513, 2015.

35. Wang, C., K. Sun, H. Niu, G. Sun, Z. Zhang, and L. Kong, "Effect of Binary Admixture of Sepiolite and Fly Ash on Carbonation and Chloride Resistance of Modified Cement Mortar", *Construction and Building Mater*ials, Vol. 279, p. 122509, 2021.

36. Kaya-Özkiper, K., A. Uzun, and S. Soyer-Uzun, "Tuning Adsorption, Structure and Compressive Strength of Sepiolite- and Metakaolin-Based Alkali Activated Monoliths for Methylene Blue Removal from Waste Water", *Surfaces and Interfaces*, Vol. 33, p. 102110, 2022.

37. Kaya-Özkiper, K., A. Uzun, and S. Soyer-Uzun, "A Novel Alkali Activated Magnesium Silicate as an Effective and Mechanically Strong Adsorbent for Methylene Blue Removal", *Journal of Hazardous Materials*, Vol. 424, p. 127256, 2022.

38. Temuujin, J., W. Rickard, M. Lee, and A. Van Riessen, "Preparation and Thermal Properties of Fire Resistant Metakaolin-Based Geopolymer-Type Coatings", *Journal of Non Crystalline Solids*, Vol. 357, No. 5, pp. 1399–1404, 2011.

39. Kim, B., J. Kang, Y. Shin, T. Yeo, J. Heo, and W. Um, “Effect of Si/Al Molar Ratio and Curing Temperatures on the Immobilization of Radioactive Borate Waste in Metakaolin-Based Geopolymer Waste Form”, *Journal of Hazardous Materials*, Vol. 458, p. 131884, 2023.

40. Kim, B., J. Kang, Y. Shin, T. min Yeo, and W. Um, “Immobilization Mechanism of Radioactive Borate Waste in Phosphate-Based Geopolymer Waste Forms”, *Cement and Concrete Research*, Vol. 161, p. 106959, 2022.

41. Singh, N. B., G. Nagpal, S. Agrawal, and Rachna, “Water Purification by Using Adsorbents: A Review”, *Environmental Technology and Innovation*, Vol. 11, pp. 187–240, 2018.

42. Lee, N. K., H. R. Khalid, and H. K. Lee, “Synthesis of Mesoporous Geopolymers Containing Zeolite Phases by a Hydrothermal Treatment”, *Microporous and Mesoporous Materials*, Vol. 229, pp. 22–30, 2016.

43. Li, L., S. Wang, and Z. Zhu, “Geopolymeric Adsorbents from Fly Ash for Dye Removal from Aqueous Solution”, *Journal of Colloid Interface Science*, Vol. 300, No. 1, pp. 52–59, 2006.

44. Karuppaiyan, J., A. Mullaimalar, and R. Jeyalakshmi, “Adsorption of Dyestuff by Nano Copper Oxide Coated Alkali Metakaoline Geopolymer in Monolith and Powder Forms: Kinetics, Isotherms and Microstructural Analysis”, *Environmental Research*, Vol. 218, p. 115002, 2023.

45. Fumba G., J.S. Essomba, G.M. Tagne and N.J. Nsami, “Equilibrium and Kinetic Adsorption Studies of Methyl Orange from Aqueous Solutions Using Kaolinite, Metakaolinite and Activated Geopolymer as Low Cost Adsorbents”, *Journal of Academia and Industrial Research*, Vol. 3, p. 156, 2014.

46. Novais, R. M., J. Carvalheiras, D. M. Tobaldi, M. P. Seabra, R. C. Pullar, and J. A. Labrincha, “Synthesis of Porous Biomass Fly Ash-Based Geopolymer Spheres for Efficient Removal of Methylene Blue from Wastewaters”, *Journal of Cleaner Production*, Vol. 207, pp. 350–362, 201.

47. Novais R. M., G. Ascensão, D. M. Tobaldi, M. P. Seabra, and J. A. Labrincha, “Biomass Fly Ash Geopolymer Monoliths for Effective Methylene Blue Removal from Wastewaters”, *Journal of Cleaner Production*, Vol. 171, pp. 783–794, 2018.

48. Kaewmee, P., M. Song, M. Iwanami, H. Tsutsumi, and F. Takahashi, “Porous and Reusable Potassium-Activated Geopolymer Adsorbent with High Compressive Strength Fabricated from Coal Fly Ash Wastes”, *Journal of Cleaner Production*, Vol. 272, p. 122617, 2020.

49. Açışlı, Ö., İ. Acar, and A. Khataee, “Preparation of a Surface Modified Fly Ash-Based Geopolymer for Removal of an Anionic Dye: Parameters and Adsorption Mechanism”, *Chemosphere*, Vol. 295, p. 133870, 2022.

50. Siyal, A. A., M. R. Shamsuddin, S. H. Khahro, A. Low, and M. Ayoub, “Optimization of Synthesis of Geopolymer Adsorbent for the Effective Removal of Anionic Surfactant from Aqueous Solution”, *Journal of Environmental Chemical Engineering*, Vol. 9, No. 1, p. 104949, 2021.

51. Aouan, B., S. Aleyhen, M. Fadil, M. El Alouani, H. Saufi, E. H. El Herradi, F. El Makhoukhi and M. Taibi, “Development and Optimization of Geopolymer Adsorbent for Water Treatment: Application of Mixture Design Approach”, *Journal of Environmental Management*, Vol. 338, p. 117853, 2023.

52. Kaya-Özkiper, K., A. Uzun, and S. Soyer-Uzun, “Tuning Adsorption, Structure and Compressive Strength of Sepiolite- and Metakaolin-Based Alkali Activated Monoliths for Methylene Blue Removal from Waste Water”, *Surfaces and Interfaces*, Vol. 33, p. 102110, 2022.

53. Ouellet-Plamondon, C., P. Aranda, A. Favier, G. Habert, H. van Damme, and E. Ruiz-Hitzky, “The Maya Blue Nanostructured Material Concept Applied to Colouring Geopolymers”, *Royal Society of Chemistry Advances,* Vol. 5, No. 120, pp. 98834–98841, 2015.

54. Galan, E., “Properties and Application of Palygorskite-Sepiolite Clays”, *Clay Minerals,* Vol. 31, pp. 443–453, 1996.

55. Doğan, M., Y. Özdemir, and M. Alkan, “Adsorption Kinetics and Mechanism of Cationic Methyl Violet and Methylene Blue Dyes onto Sepiolite”, *Dyes and Pigments,* Vol. 75, No. 3, pp. 701–713, 2007.

56. Largo, F., R. Haounati, S. Akhouairi, H. Ouachtak, R. El Haouti, A. El Guerdaoui, N. Hafid, D.M.F. Santos, F. Akbal, A. Kuleyin, A. Jada and A.A. Addi, “Adsorptive Removal of Both Cationic and Anionic Dyes by Using Sepiolite Clay Mineral as Adsorbent: Experimental and Molecular Dynamic Simulation Studies”, *Journal of Molecular Liquids,* Vol. 318, p. 114247, 2020.

57. David, E., “Mechanical Strength and Reliability of the Porous Materials Used as Adsorbents Catalysts and the New Development Trends”, *Archives of Material Science and Engineering*, Vol. 73, pp. 5–17, 2015.

58. Mackenzie, K., S. Bradley, J. Hanna, and M. Smith, “Magnesium Analogues of Aluminosilicate Inorganic Polymers (Geopolymers) from Magnesium Minerals”, *Journal of Material Science,* Vol. 48, pp. 1787–1793, 2013.

59. Rees, C., J. Provis, G. Lukey, and J. Van Deventer, “Attenuated Total Reflectance Fourier Transform Infrared Analysis of Fly Ash Geopolymer Gel Aging”, *Langmuir*, Vol. 23, pp. 8170–8179, 2007.

60. Hajimohammadi A. and J. S. J. van Deventer, “Characterisation of One-Part Geopolymer Binders Made from Fly Ash”, *Waste Biomass Valorization*, Vol. 8, No. 1, pp. 225–233, 2017.

61. Zhang, Y. J., P. Y. He, Y. X. Zhang, and H. Chen, “A Novel Electroconductive Graphene/Fly Ash-Based Geopolymer Composite and its Photocatalytic Performance”, *Chemical Engineering Journal*, Vol. 334, pp. 2459–2466, 2018.

62. Williams R. P. and A. van Riessen, “Development of Alkali Activated Borosilicate Inorganic Polymers (AABSIP)”, *Journal of European Ceramic Society*, Vol. 31, No. 8, pp. 1513–1516, 2011.

63. Nguyen T. D. L. and B. Bleys, “Applying Analytic Hierarchy Process to Adaptation to Saltwater Intrusion in Vietnam”, *Sustainability*, Vol. 13, No. 4, p. 2311, 2021.

64. Miller, S. A., A. Horvath, and P. J. M. Monteiro, “Readily Implementable Techniques Can Cut Annual CO_2 Emissions from the Production of Concrete by over 20%”, *Environmental Research Letters*, Vol. 11, No. 7, p. 74029, 2016.

65. Davis, S. J., N.S. Lewis, M. Shaner, S. Aggarval, D. Arent, I. Azededo, S.M. Benson, T. Bradley, J. Brouwer, Y. Chiang, C.T.M. Clack, A. Cohen, S. Doig, J. Edmonds, P. Fennell, C.B. Field, B. Hannegan, B. Hodge, M.I. Hoffert, E. Ingersoll, P. Jaramillo, K.S. Lackner, K.J. Mach, M. Mastrandrea, J.Ogden, P.F. Peterson, D.L. Sanchez, D. Sperling, J. Stagner, J.E. Trancik, C. Yang, and K. Calderia, “Net-Zero Emissions Energy Systems”, *Science*, Vol. 360, No. 6396, p. 9793, 2018.

66. Abiodun, Y. O., O. A. Olanrewaju, O. P. Gbenebor, E. F. Ochulor, D. V. Obasa, and S. O. Adeosun, “Cutting Cement Industry CO_2 Emissions through Metakaolin Use in Construction”, *Atmosphere*, Vol. 13, No. 9, p. 1494, 2022.

67. Farooq, F., J. Xin, M.F. Javed, A. Akbar, M.I. Shah, F. Aslam, R. Alyousef, "Geopolymer Concrete as Sustainable Material: A State of the Art Review", *Construction and Building Materials*, Vol. 306, p. 124762, 2021.

68. Van Deventer, J. S. J., J. L. Provis, and P. Duxson, "Technical and Commercial Progress in the Adoption of Geopolymer Cement", *Minerals Engineering*, Vol. 29, pp. 89–104, 2012.

69. Çetintaş, R. and S. Soyer-Uzun, "Relations Between Structural Characteristics and Compressive Strength in Volcanic Ash Based One–Part Geopolymer Systems", *Journal of Building Engineering*, Vol. 20, pp. 130–136, 2018.

70. Kaya-Özkiper, K., A. Uzun, and S. Soyer-Uzun, "Red Mud- and Metakaolin-Based Geopolymers for Adsorption and Photocatalytic Degradation of Methylene Blue: Towards Self-Cleaning Construction Materials", *Journal of Cleaner Production*, Vol. 288, p. 125120, 2021.

71. Kaya, K., S. F. Kurtoğlu, A. Uzun, and S. Soyer-Uzun, "Consequences of Simple Acid-Pretreatments on Geopolymerization and Thermal Stability of Red Mud-Based Geopolymers", *Industrial & Engineering Chemistry Research*, Vol. 57, No. 21, pp. 7156–7168, 2018.

72. Ben Haha, M., B. Lothenbach, G. Le Saout, and F. Winnefeld, "Influence of Slag Chemistry on the Hydration of Alkali-Activated Blast-Furnace Slag — Part I: Effect of MgO", *Cement and Concrete Research*, Vol. 41, No. 9, pp. 955–963, 2011.

73. Jin, F., K. Gu, and A. Al-Tabbaa, "Strength and Hydration Properties of Reactive MgO-Activated Ground Granulated Blast Furnace Slag Paste", *Cement and Concrete Composites*, Vol. 57, pp. 8–16, 2015.

74. Song, N., A. Hursthouse, I. McLellan, and Z. Wang, "Treatment of Environmental Contamination Using Sepiolite: Current Approaches and Future Potential", *Environmental Geochemistry Health*, Vol. 43, No. 7, pp. 2679–2697, 2021.

75. Kurtoğlu, S. F., S. Sarp, C.Y. Akkaya, B. Yağcı, A. Motallebzadeh, S. Soyer-Uzun, A. Uzun., "COx-Free Hydrogen Production from Ammonia Decomposition over Sepiolite-Supported Nickel Catalysts", *International Journal of Hydrogen Energy*, Vol. 43, No. 21, pp. 9954–9968, 2018.

76. Beyli, P. T., M. Doğan, M. Alkan, A. Türkyılmaz, Y. Turhan, Ö. Demirbaş and H. Namlı., "Characterization, Adsorption, and Electrokinetic Properties of Modified Sepiolite", *Desalination Water Treatment*, Vol. 57, No. 41, pp. 19248–19261, 2016.

77. Barroso-Solares, S., B. Merillas, P. Cimavilla-Román, M. A. Rodriguez-Perez, and J. Pinto, "Enhanced Nitrates-Polluted Water Remediation by Polyurethane/Sepiolite Cellular Nanocomposites", *Journal of Cleaner Production*, Vol. 254, p. 120038, 2020.

78. Pu, S., P. Duan, C. Yan, and D. Ren, "Influence of Sepiolite Addition on Mechanical Strength and Microstructure of Fly Ash-Metakaolin Geopolymer Paste", *Advanced Powder Technology*, Vol. 27, No. 6, pp. 2470–2477, 2016.

79. Yan, B., P. Duan, and D. Ren, "Mechanical Strength, Surface Abrasion Resistance and Microstructure of Fly Ash-Metakaolin-Sepiolite Geopolymer Composites", *Ceramics International*, Vol. 43, No. 1, pp. 1052–1060, 2017.

80. Montgomery, D. C., *Introduction to Statistical Quality Control.*, Third Edition, Wiley, New York, 1996.

81. Perraki, T. and A. Orfanoudaki, "Study of Raw and Thermally Treated Sepiolite from the Mantoudi Area, Euboea, Greece", *Journal of Thermal Analysis and Calorimetry*, Vol. 91, No. 2, pp. 589–593, 2008.

82. d'Azevedo, C. A., F. Garrido, and M. Medeiros, "The Effect of Mechanochemical Activation on the Reactivity in the $MgO–Al_2O_3–SiO_2$ System", *Journal of Thermal Analysis and Calorimetry*, Vol. 83, pp. 649-655, 2006.

83. Ahlrichs, J. L., C. Serna, and J. M. Serratosa, “Structural Hydroxyls in Sepiolites”, *Clays Clay Minerals*, Vol. 23, No. 2, pp. 119–124, 1975.

84. Casal, B., J. Merino, J.-M. Serratosa, and E. Ruiz-Hitzky, “Sepiolite-Based Materials for the Photo and Thermal Stabilization of Pesticides”, *Applied Clay Science*, Vol. 18, No. 5, pp. 245–254, 2001.

85. Kumar, A. and S. Kumar, “Development of Paving Blocks from Synergistic Use of Red Mud and Fly Ash Using Geopolymerization”, *Construction and Building Materials*, Vol. 38, pp. 865–871, 2013.

86. Olszówka J. E., R. Karcz, E. Bielanska, J. Krysciak-Czerwenka, B.D. Napruszewka, B. Sulikowski, R.P. Socha, A. Gawel, K. Bahranowski, Z. Olejniczak and E. M. Serwicka, “New Insight into the Preferred Valency of Interlayer Anions in Hydrotalcite-like Compounds: The effect of Mg/Al Ratio”, *Applied Clay Science*, Vol. 155, pp. 84–94, 2018.

87. Bukas, V. J., M. Tsampodimou, V. Gionis, and G. D. Chryssikos, “Synchronous ATR Infrared and NIR-Spectroscopy Investigation of Sepiolite Upon Drying”, *Vibrational Spectroscopy*, Vol. 68, pp. 51–60, 2013.

88. Frost R. and Z. Ding, “Controlled Rate Thermal Analysis and Differantial Scanning Calorimetry of Sepiolites and Palygorskites”, *Thermochimica Acta*, Vol. 397, pp. 119–128, 2003.

89. Ye, N., J. Yang, X. Ke, J. Zhu, Y. Li, C. Xiang, H. Wang, L. Li and B. Xiao, “Synthesis and Characterization of Geopolymer from Bayer Red Mud with Thermal Pretreatment”, *Journal of the American Ceramic Society*, Vol. 97, No. 5, pp. 1652–1660, 2014.

90. Kok, M. V., “Thermal Characterization of Sepiolite Samples”, *Energy Sources, Part A: Recovery, Utilization, and Environmental Effects*, Vol. 35, No. 2, pp. 173–183, 2013.

91. Vengatesan, M. R., S. Singh, S. Stephen, K. Prasanna, C. W. Lee, and V. Mittal, “Facile Synthesis of Thermally Reduced Graphene Oxide-Sepiolite Nanohybrid via Intercalation and Thermal Reduction Method”, *Applied Clay Science*, Vol. 135, pp. 510–515, 2017.

92. Walczyk, A., A. Michalik, B.D. Napruszewska, J. Krysciak-Czerwenka, R. Karcz, D. Duraczynska, R.P. Socha, Z. Olejniczak, A. Gawel, A. Klimek, M. Wojcik-Bania, K. Bahranowski and E. M. Serwicka., “New Insight into the Phase Transformation of Sepiolite upon Alkali Activation: Impact on Composition, Structure, Texture, and Catalytic/Sorptive Properties”, *Applied Clay Science*, Vol. 195, p. 105740, 2020.

93. Xu, Z., W. Li, Y. Zhang, Z. Xue, X. Guo, and G. Zhang, “Facile Synthesis of Mesoporous Reduced Graphene Oxide Microspheres with Well-Distributed Fe_2O_3 Nanoparticles for Photochemical Catalysis”, *Industrial & Engineering Chemistry Research*, Vol. 55, No. 40, pp. 10591–10599, 2016.

94. Soe, T., A. Jityen, T. Kongkaew, K. Subannajui, A. Sinsarp, and T. Osotchan, “X-ray Photoelectron Spectroscopy Study of Chromium and Magnesium Doped Copper Ferrite Thin Film”, *AIP Conference Proceedings*, Vol. 2279, p. 140002, 2020.

95. Provis, J. L., P. Duxson, J. S. J. Van Deventer, and G. C. Lukey, “The Role of Mathematical Modelling and Gel Chemistry in Advancing Geopolymer Technology”, *Chemical Engineering Research and Design*, Vol. 83, No. 7, pp. 853–860, 2005.

96. Murayama, N., H. Yamamoto, and J. Shibata, “Mechanism of Zeolite Synthesis from Coal Fly Ash by Alkali Hydrothermal Reaction”, *International Journal of Mineral Process*, Vol. 64, No. 1, pp. 1–17, 2002.

97. Rowles, M. and B. O'Connor, "Chemical optimisation of the compressive strength of aluminosilicate geopolymers synthesised by sodium silicate activation of metakaolinite", *Journal of Materials Chemitry.*, vol. 13, no. 5, pp. 1161–1165, 2003.

98. Najafi, E. and H. Mehdizadeh, "Investigating Gel Molecular Structure and Its Relation with Mechanical Strength in Geopolymer Cement Based on Natural Pozzolan Using In Situ ATR-FTIR Spectroscopy", *Journal of Materials in Civil Engineering*, Vol. 29, p. 4017078, 2017.

99. Hajimohammadi, A., J. Provis, and J. Van Deventer, "The Effect of Alumina Release Rate on the Mechanism of Geopolymer Gel Formation", *Chemistry of Materials*, Vol. 22, pp. 5199-5208, 2010.

100. Mittal, V. K., S. Bera, R. Nithya, M. P. Srinivasan, S. Velmurugan, and S. V Narasimhan, "Solid State Synthesis of Mg–Ni Ferrite and Characterization by XRD and XPS", *Journal of Nuclear Materials*, Vol. 335, No. 3, pp. 302–310, 2004.

101. Gümüş, D. and F. Akbal, "Photocatalytic Degradation of Textile Dye and Wastewater", *Water Air Soil Pollution*, Vol. 216, No. 1, pp. 117–124, 2011.

102. Russo, V., D. Masiello, M. Trifuoggi, M. Di Serio, and R. Tesser, "Design of an Adsorption Column for Methylene Blue Abatement Over Silica: From Batch to Continuous Modeling", *Chemical Engineering Journal*, Vol. 302, pp. 287-295, 2016.

103. Sarayu K. and S. Sandhya, "Current Technologies for Biological Treatment of Textile Wastewater–A Review", *Applied Biochemistry and Biotechnology*, Vol. 167, No. 3, pp. 645–661, 2012.

104. Khehra, M. S., H. S. Saini, D. K. Sharma, B. S. Chadha, and S. S. Chimni, "Biodegradation of Azo Dye C.I. Acid Red 88 by an Anoxic–Aerobic Sequential Bioreactor", *Dyes and Pigments*, Vol. 70, No. 1, pp. 1–7, 2006.

105. Gharabaghi, M., M. Irannajad, and A. R. Azadmehr, “Selective Sulphide Precipitation of Heavy Metals from Acidic Polymetallic Aqueous Solution by Thioacetamide”, *Industrial & Engineering Chemistry Research*, Vol. 51, No. 2, pp. 954–963, 2012.

106. Alventosa-deLara, E., S. Barredo-Damas, M. I. Alcaina-Miranda, and M. I. Iborra-Clar, “Ultrafiltration Technology with a Ceramic Membrane for Reactive Dye Removal: Optimization of Membrane Performance”, *Journal of Hazardous Materials*, Vol. 209–210, pp. 492–500, 2012.

107. Li, Q., Y. Li, X. Ma, Q. Du, K. Sui, D. Wang, C. Wang, H. Li, Y. Xia., “Filtration and Adsorption Properties of Porous Calcium Alginate Membrane for Methylene Blue Removal from Water”, *Chemical Engineering Journal*, Vol. 316, pp. 623–630, 2017.

108. Nasuha, N., S. Ismail, and B. Hameed, “Activated Electric Arc Furnace Slag as an Efficient and Reusable Heterogeneous Fenton-Like Catalyst for the Degradation of Reactive Black 5”, *Journal of the Taiwan Institute of Chemical Engineers*, Vol. 67, pp. 235-243, 2016.

109. Tehrani-Bagha, A. R., N. M. Mahmoodi, and F. M. Menger, “Degradation of a Persistent Organic Dye from Colored Textile Wastewater by Ozonation”, *Desalination*, Vol. 260, No. 1, pp. 34–38, 2010.

110. Bensalah, H., S. Younssi, M. Ouammou, A. Gurlo, and M. Bekheet, “Azo Dye Adsorption on an Industrial Waste-Transformed Hydroxyapatite Adsorbent: Kinetics, Isotherms, Mechanism and Regeneration Studies”, *Journal of Environmental Chemical Engineering*, Vol. 8, p. 103807, 2020.

111. Gupta, V., I. Ali, T. Saleh, A. Nayak, and S. Agarwal, “Chemical Treatment Technologies for Wastewater Recycling–an Overview”, *RSC Advances*, Vol. 2, pp. 6380–6388, 2012.

112. Dotto, G. L. and G. McKay, “Current Scenario and Challenges in Adsorption for Water Treatment”, *Journal of Environmental Chemical Engineering*, Vol. 8, No. 4, p. 103988, 2020.

113. Lyu, H., B. Gao, F. He, A.R. Zimmerman, C. Ding, J. Tang and J.C. Crittenden, “Experimental and Modeling Investigations of Ball-Milled Biochar for the Removal of Aqueous Methylene Blue”, *Chemical Engineering Journal*, Vol. 335, pp. 110–119, 2018.

114. Li, B., Y. Zhang, D. Ma, Z. Shi, and S. Ma, “Mercury Nano-Trap for Effective and Efficient Removal of Mercury(II) from Aqueous Solution”, *Nature Communications*, Vol. 5, p. 5537, 2014.

115. Bentahar, S., A. Dbik, M. El Khomri, N. El Messaoudi, and A. Lacherai, “Adsorption of Methylene Blue, Crystal Violet and Congo Red from Binary and Ternary systems with Natural Clay: Kinetic, Isotherm, and Thermodynamic”, *Journal of Environmental Chemical Engineering*, Vol. 5, No. 6, pp. 5921–5932, 2017.

116. Mouni, L., L. Belkhiri, J. Bollinger, A. Bouzaza, A. Assadi, A. Tirri, F. Dahmoune, K. Madani and H. Remini, “Removal of Methylene Blue from Aqueous Solutions by Adsorption on Kaolin: Kinetic and Equilibrium Studies”, *Applied Clay Science*, Vol. 153, pp. 38–45, 2018.

117. Kavand, M., T. Kaghazchi, and M. Soleimani, “Optimization of Parameters for Competitive Adsorption of Heavy Metal Ions (Pb^{+2}, Ni^{+2}, Cd^{+2}) onto Activated Carbon”, *Korean Journal of Chemical Engineering*, Vol. 31, No. 4, pp. 692–700, 2014.

118. Li, Z, H. Hanafy, L. Zhang, L. Sellaoui, M.S. Netto, M.L.S. Oliviera, M.K. Seliem, G.L. Dotto, A. Bonilla-Petriciolet and Q. Li, “Adsorption of Congo Red and Methylene Blue Dyes on an Ashitaba Waste and a Walnut Shell-Based Activated

Carbon from Aqueous Solutions: Experiments, Characterization and Physical Interpretations", *Chemical Engineering Journal*, Vol. 388, p. 124263, 2020.

119. Yoo, D. K., B. N. Bhadra, and S. H. Jhung, "Adsorptive Removal of Hazardous Organics from Water and Fuel with Functionalized Metal-Organic Frameworks: Contribution of Functional Groups", *Journal of Hazardous Materials*, Vol. 403, p. 123655, 2021.

120. Mestre, A. S., R.A. Pires, I. Aroso, E.M. Fernandes, M.L. Pinto, R.L. Reis, M.A. Andrade, J. Pires, S.P. Silva and A.P. Carvalho, "Activated Carbons Prepared from Industrial Pre-treated Cork: Sustainable Adsorbents for Pharmaceutical Compounds Removal", *Chemical Engineering Journal*, Vol. 253, pp. 408–417, 2014.

121. Rafatullah, M., O. Sulaiman, R. Hashim, and A. Ahmad, "Adsorption of Methylene Blue on Low-Cost Adsorbents: A Review", *Journal of Hazardous Materials,* Vol. 177, No. 1, pp. 70–80, 2010.

122. Padmapriya, M., S. T. Ramesh, and V. M. Biju, "Synthesis of Seawater Based Geopolymer: Characterization and Adsorption Capacity of Methylene Blue from Wastewater", *Materials Today Proceeding*, Vol. 51, pp. 1770–1776, 2022.

123. Li, C. J., Y. J. Zhang, H. Chen, P. Y. He, and Q. Meng, "Development of Porous and Reusable Geopolymer Adsorbents for Dye Wastewater Treatment", *Journal of Cleaner Production*, Vol. 348, p. 131278, 2022.

124. el Alouani, M., S. Alehyen, M. el Achouri, and M. Taibi, "Preparation, Characterization, and Application of Metakaolin-Based Geopolymer for Removal of Methylene Blue from Aqueous Solution", *Journal of Chemistry*, Vol. 2019, pp. 1–14, 2019.

125. Kaya K. and S. Soyer-Uzun, "Evolution of Structural Characteristics and Compressive Strength in Red Mud–Metakaolin Based Geopolymer Systems", *Ceramics International,* Vol. 42, No. 6, pp. 7406–7413, 2016.

126. Küncek İ. and S. Şener, "Adsorption of Methylene Blue onto Sonicated Sepiolite from Aqueous Solutions", *Ultrasonics Sonochemistry,* Vol. 17, No. 1, pp. 250–257, 2010.

127. Alkan, M., S. Çelikçapa, Ö. Demirbaş, and M. Doğan, "Removal of Reactive Blue 221 and Acid Blue 62 Anionic Dyes from Aqueous Solutions by Sepiolite", *Dyes and Pigments,* Vol. 65, No. 3, pp. 251–259, 2005.

128. Kocaoba, S., "Adsorption of Cd(II), Cr(III) and Mn(II) on Natural Sepiolite", *Desalination,* Vol. 244, No. 1, pp. 24–30, 2009.

129. Sabah E., "Decolorization of Vegetable oils: Chlorophyll-a Adsorption by acid-Activated Sepiolite", *Journal of Colloid Interface Science,* Vol. 310, No. 1, pp. 1–7, 2007.

130. Jin, H., Y. Zhang, Q. Wang, Q. Chang, and C. Li, "Rapid Removal of Methylene Blue and Nickel Ions and Adsorption/Desorption Mechanism Based on Geopolymer Adsorbent," *Colloid and Interface Science Communications,* Vol. 45, p. 100551, 2021.

131. Rożek P., M. Król, and W. Mozgawa, "Lightweight Geopolymer-Expanded Glass Composites for Removal of Methylene Blue from Aqueous Solutions", *Ceramics International,* Vol. 46, No. 12, pp. 19785–19791, 2020.

132. Ettahiri, Y., L. Bouna, J.V. Hanna, A. Benlhachemi, H.L. Pilsworth, A. Bouddoch and B. Bakiz., "Pyrophyllite Clay-Derived Porous Geopolymers for Removal of Methylene Blue from Aqueous Solutions", *Materials Chemistry and Physics,* Vol. 296, p. 127281, 2023.

133. Liu, Y., C. Yan, Z. Zhang, Y. Gong, H. Wang, and X. Qiu, “A Facile Method for Preparation of Floatable and Permeable Fly Ash-Based Geopolymer Block”, *Materials Letters*, Vol. 185, pp. 370–373, 2016.

134. el Alouani, M., S. Alehyen, M. el Achouri, and M. Taibi, “Removal of Cationic Dye - Methylene Blue from Aqueous Solution by Adsorption on Fly Ash-Based Geopolymer”, *Journal of Materials and Environmental Science*, Vol. 9, pp. 32–46, 2018.

135. Zhang Y. and L. Liu, “Fly Ash-Based Geopolymer as a Novel Photocatalyst for Degradation of Dye from Wastewater”, *Particuology*, Vol. 11, No. 3, pp. 353–358, 2013.

136. Allahverdi, A., E. Najafi, and M. Yazdanipour, “Effects of Blast-Furnace Slag on Natural Pozzolan-Based Geopolymer Cement”, *Ceramics - Silikaty*, Vol. 55, No. 1, pp. 58-68, 2011.

137. Bunker, B.C., “Molecular Mechanisms for Corrosion of Silica and Silicate Glasses”, *Journal of Non Crystalline Solids*, Vol. 179, pp. 300–308, 1994.

138. Tekin, N., A. Dinçer, Ö. Demirbaş, and M. Alkan, “Adsorption of Cationic Polyacrylamide onto Sepiolite”, *Journal of Hazardous Materials*, Vol. 134, No. 1, pp. 211–219, 2006.

139. De Silva, P., K. Sagoe-Crenstil, and V. Sirivivatnanon, “Kinetics of Geopolymerization: Role of Al_2O_3 and SiO_2”, *Cement and Concrete Research*, Vol. 37, No. 4, pp. 512–518, 2007.

140. North M. R. and T. W. Swaddle, “Kinetics of Silicate Exchange in Alkaline Aluminosilicate Solutions”, *Inorganic Chemistry*, Vol. 39, No. 12, pp. 2661–2665, 2000.

APPENDIX

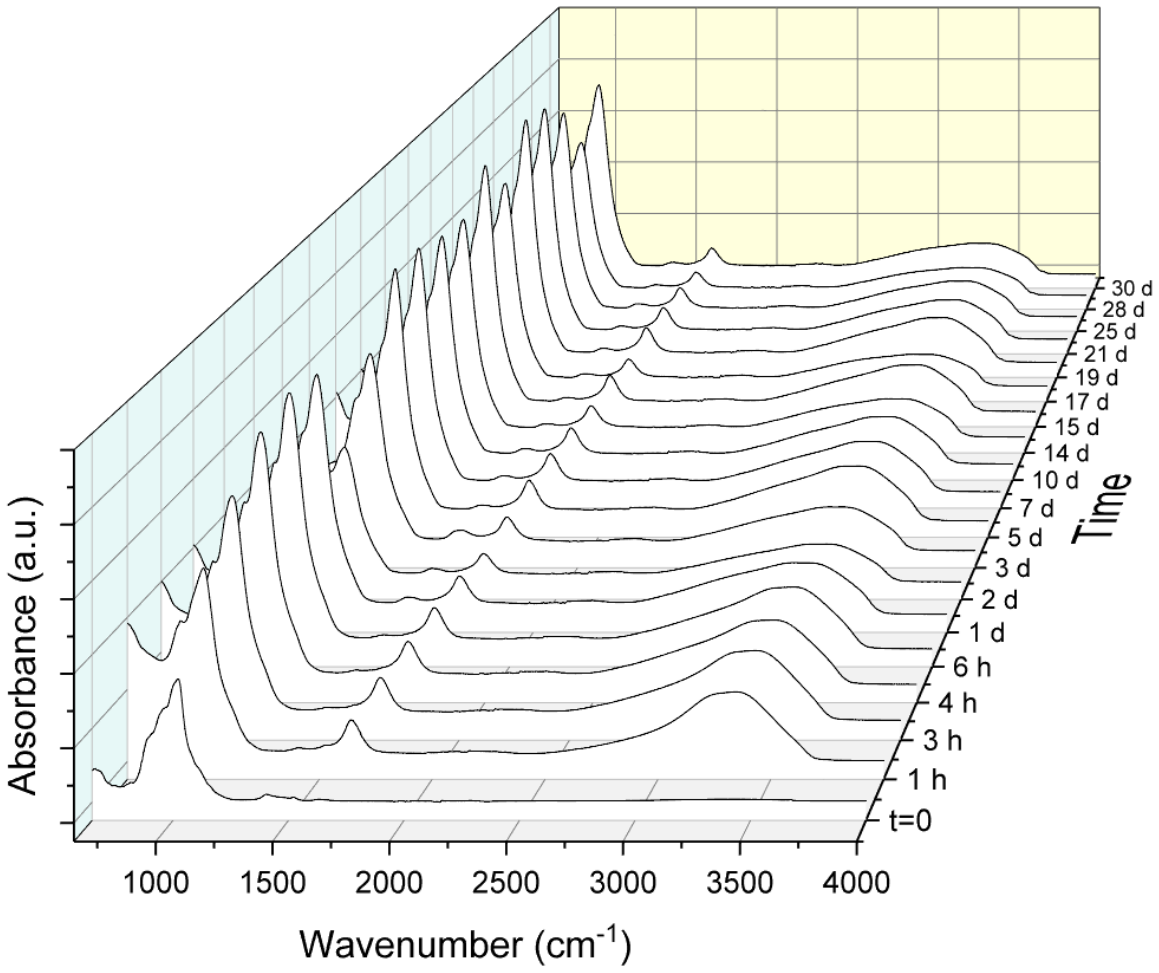

Figure A.1. FTIR data over time for SAAM-1.

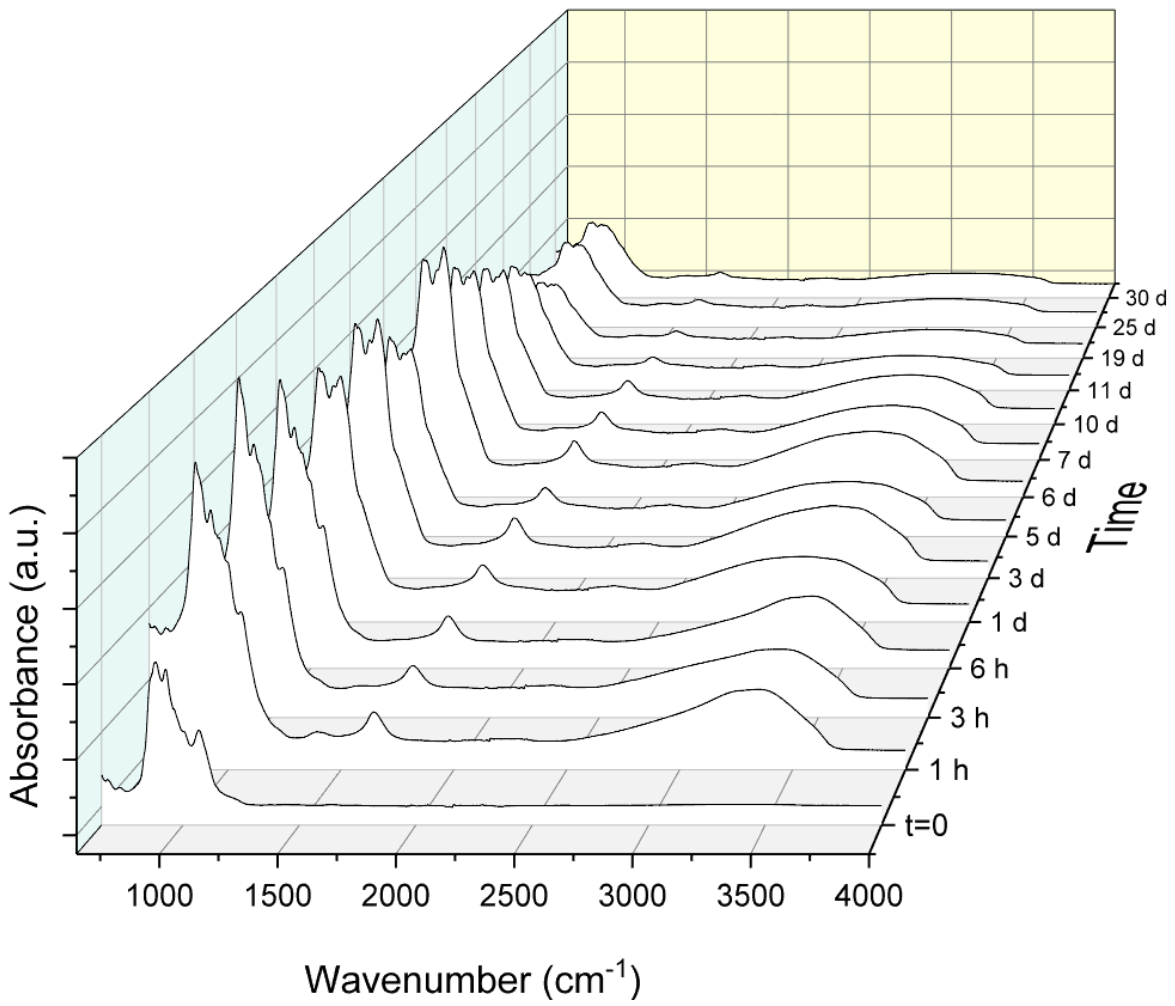

Figure A.2. FTIR data over time for SAAM-2.

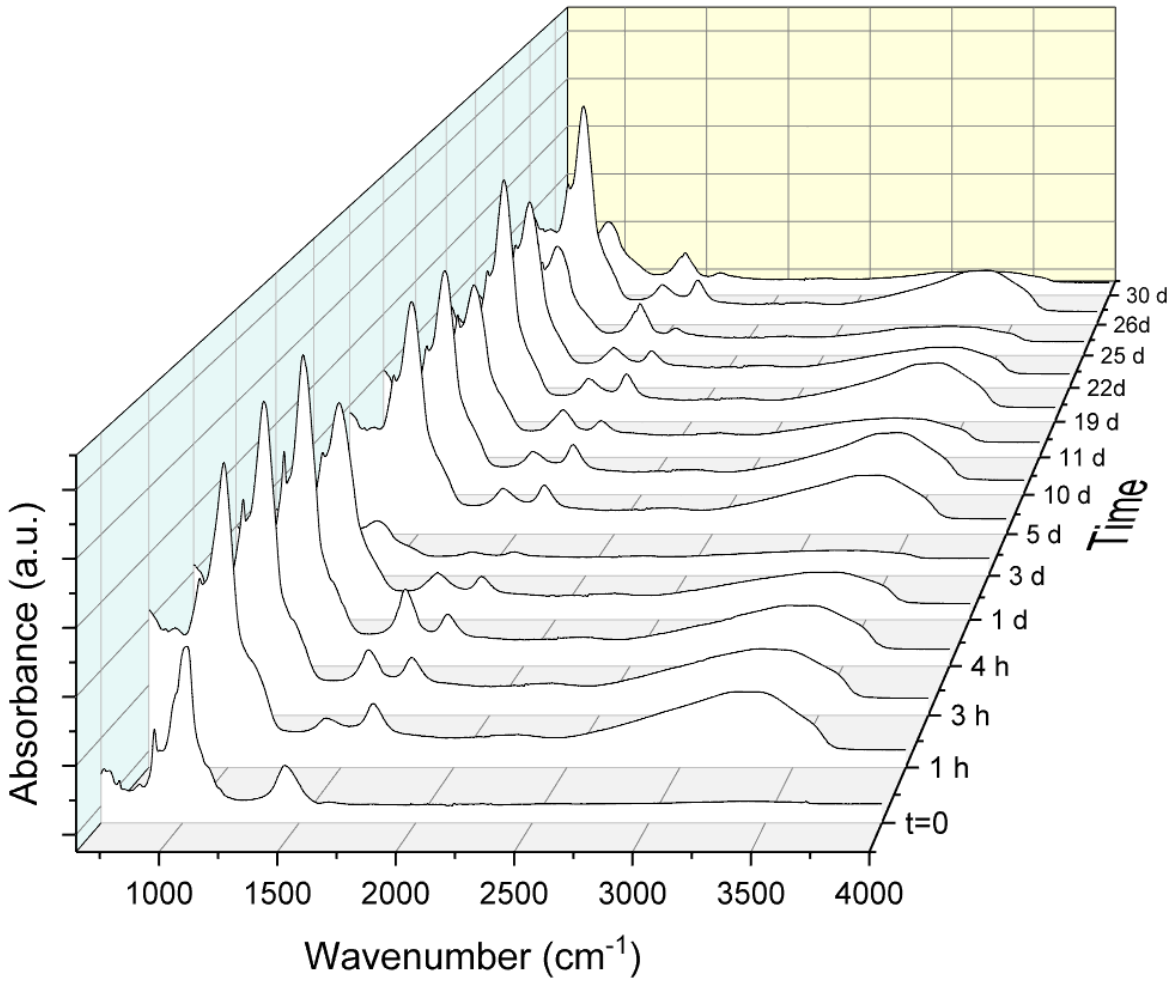

Figure A.3. FTIR data over time for SAAM-3.

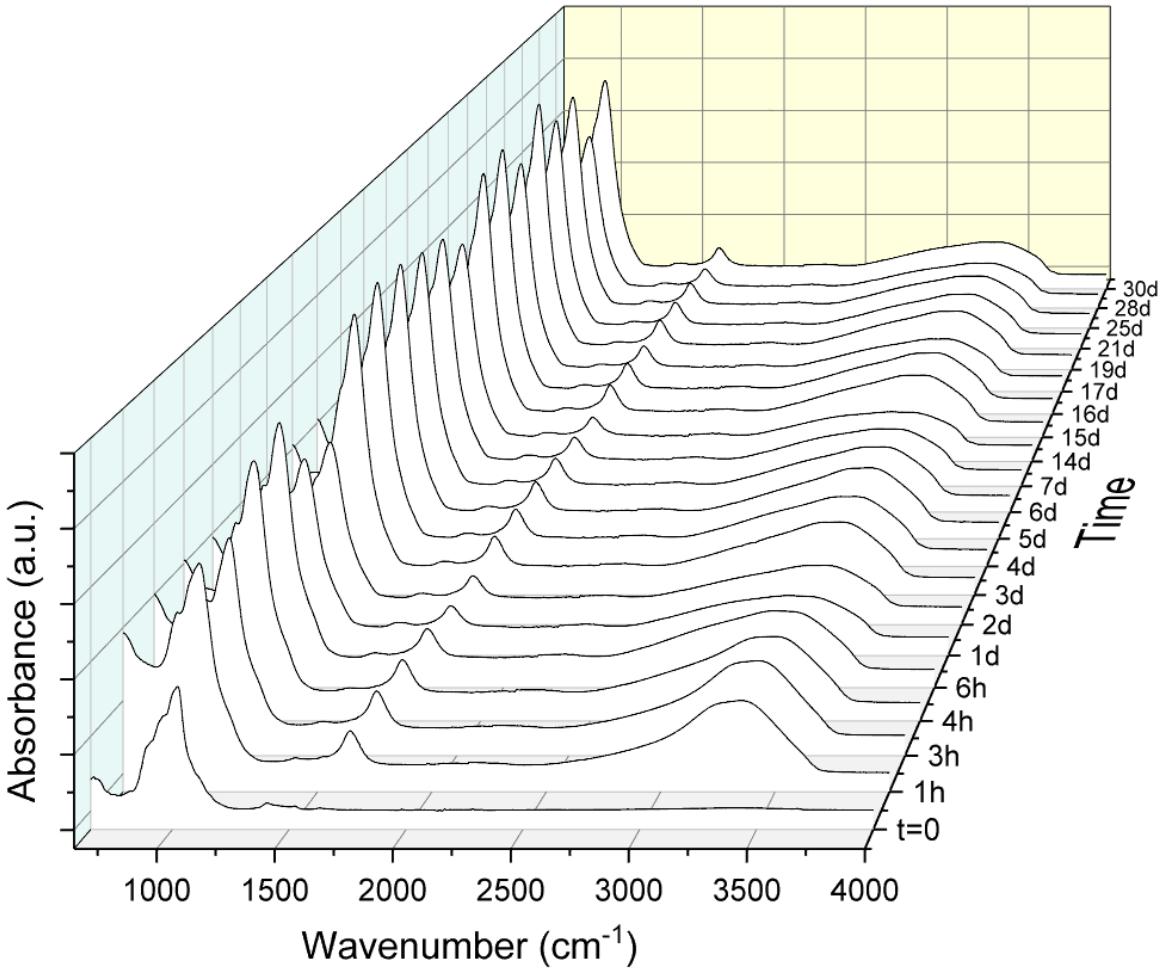

Figure A.4. FTIR data over time for SAAM-4.

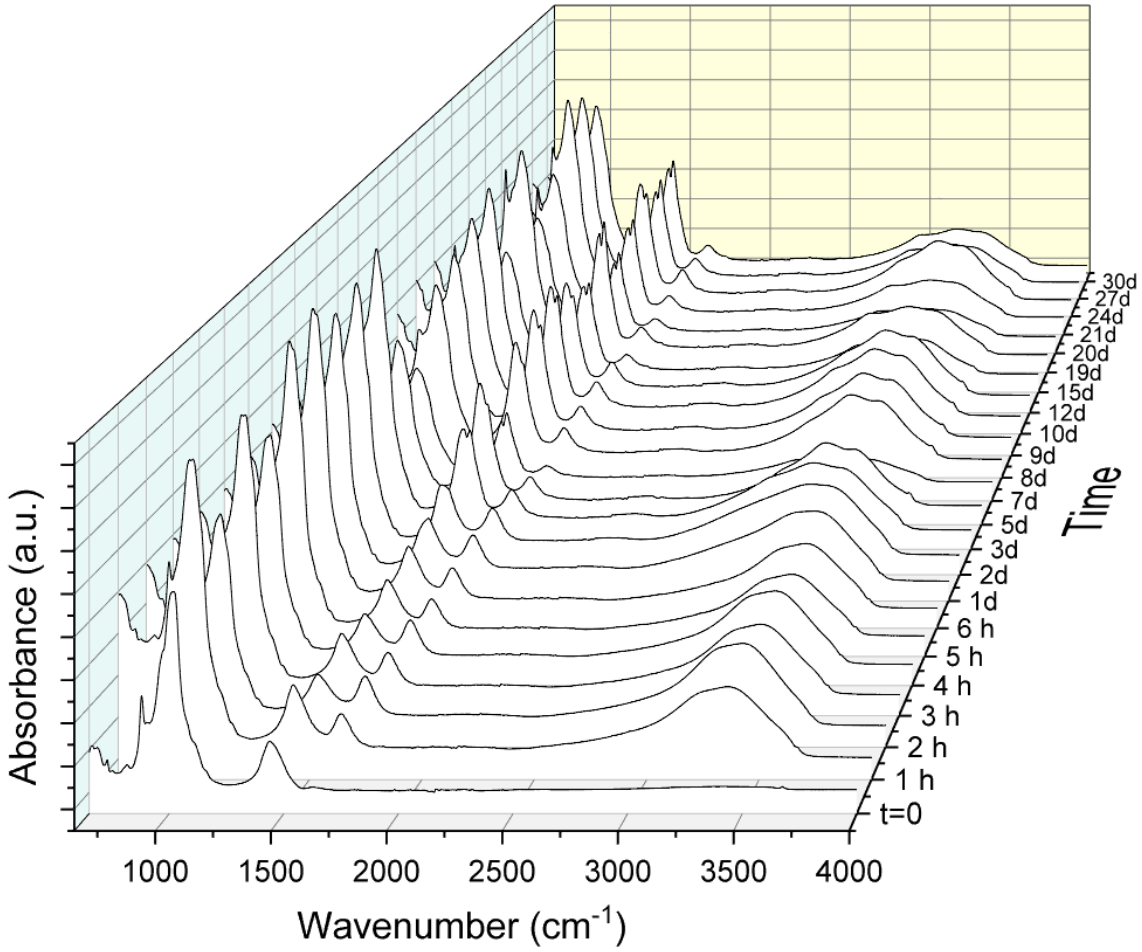

Figure A.5. FTIR data over time for SAAM-5.

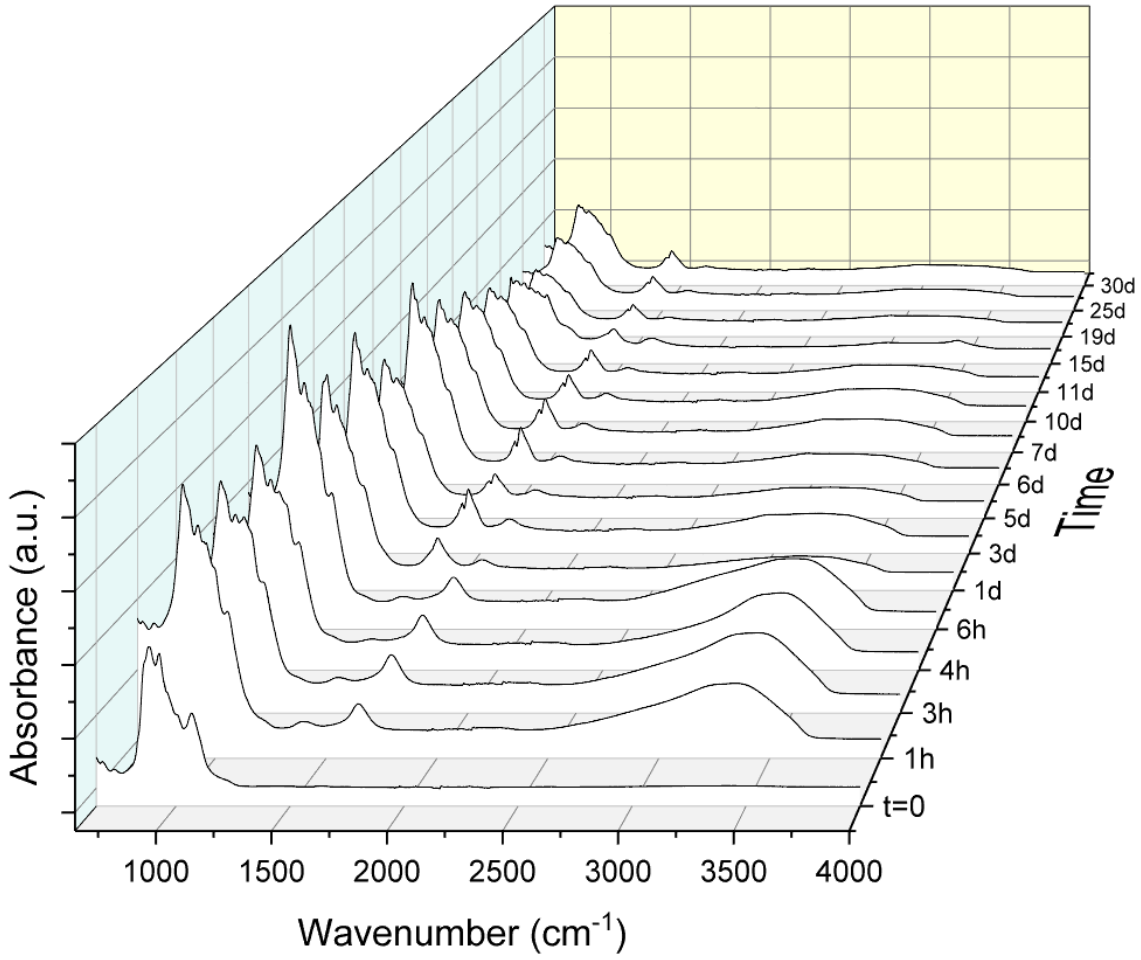

Figure A.6. FTIR data over time for SAAM-6.

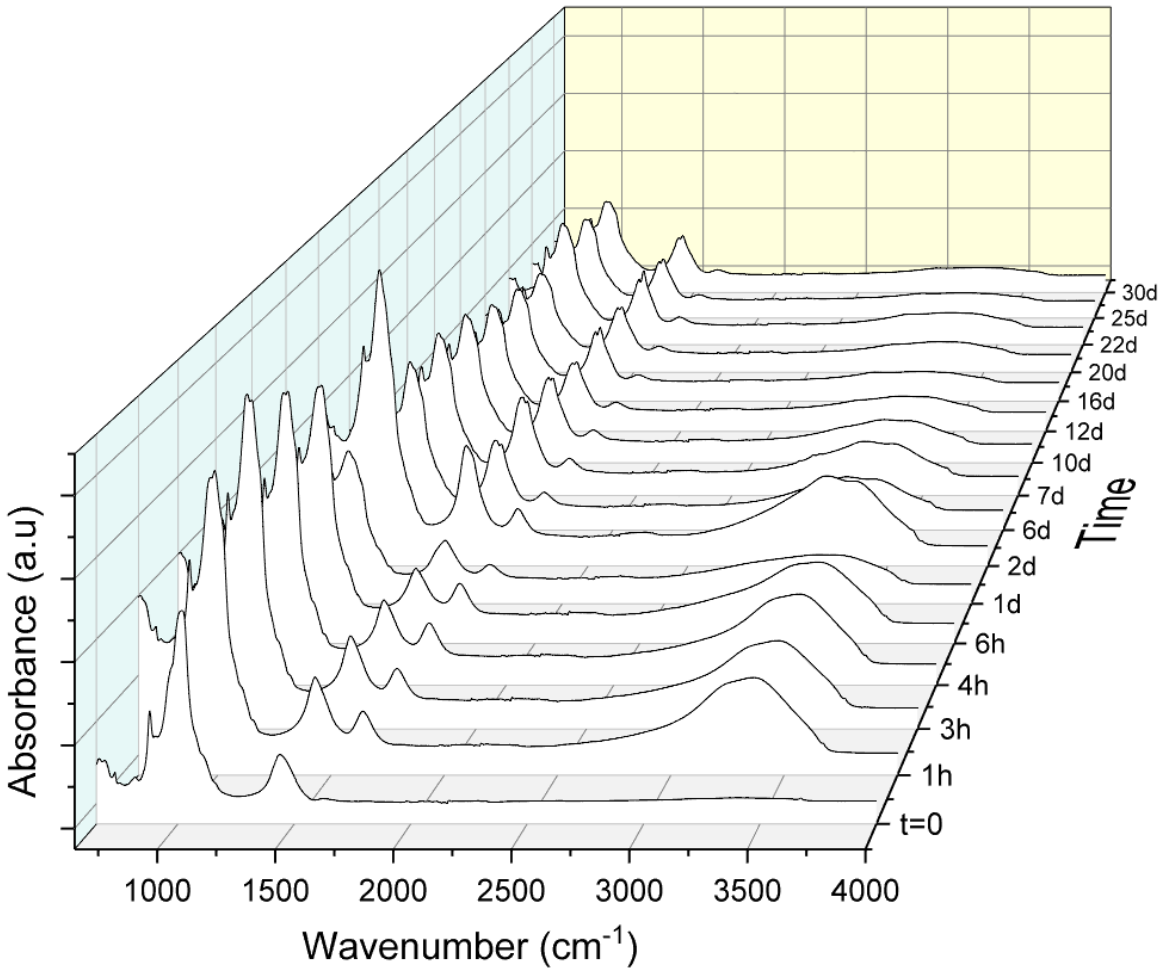

Figure A.7. FTIR data over time for SAAM-7.

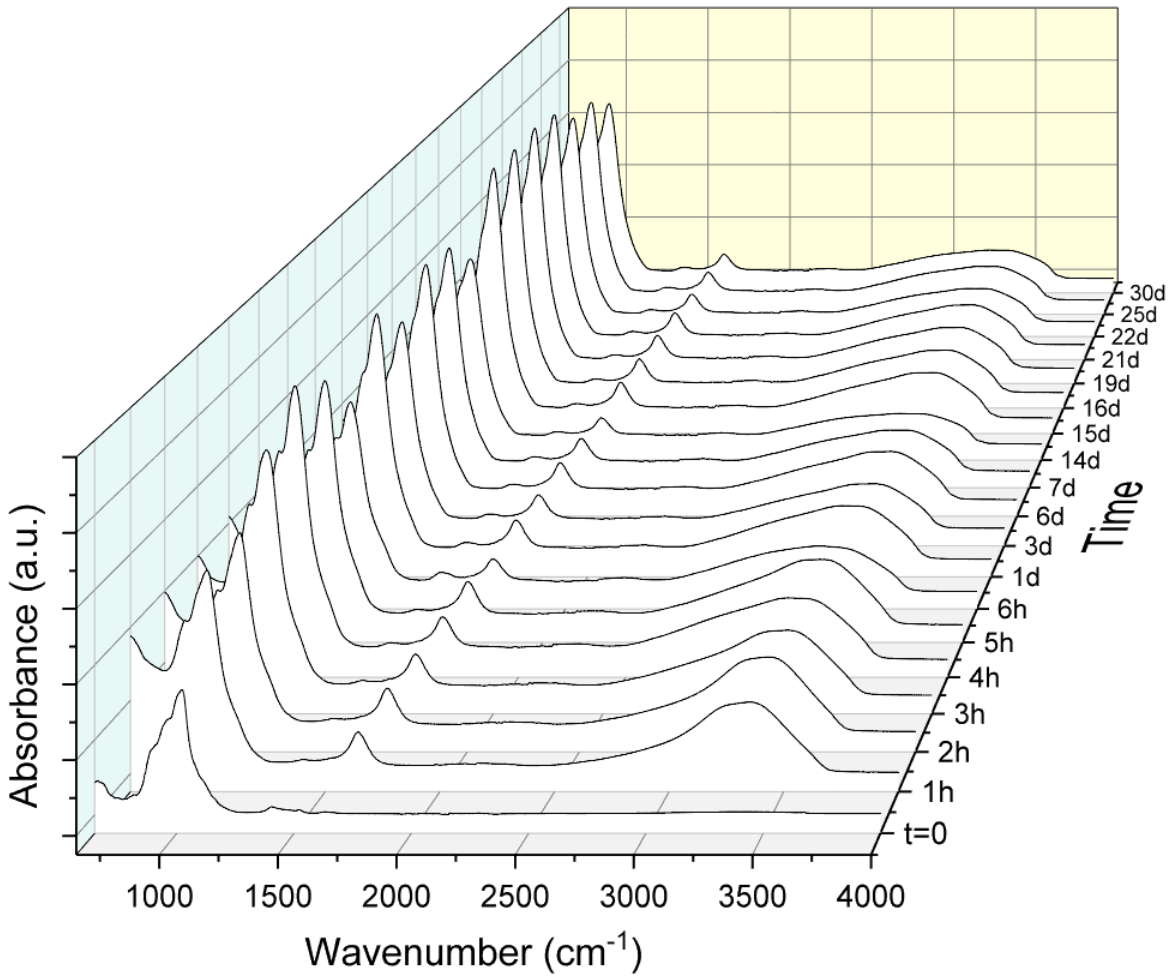

Figure A.8. FTIR data over time for SAAM-8.

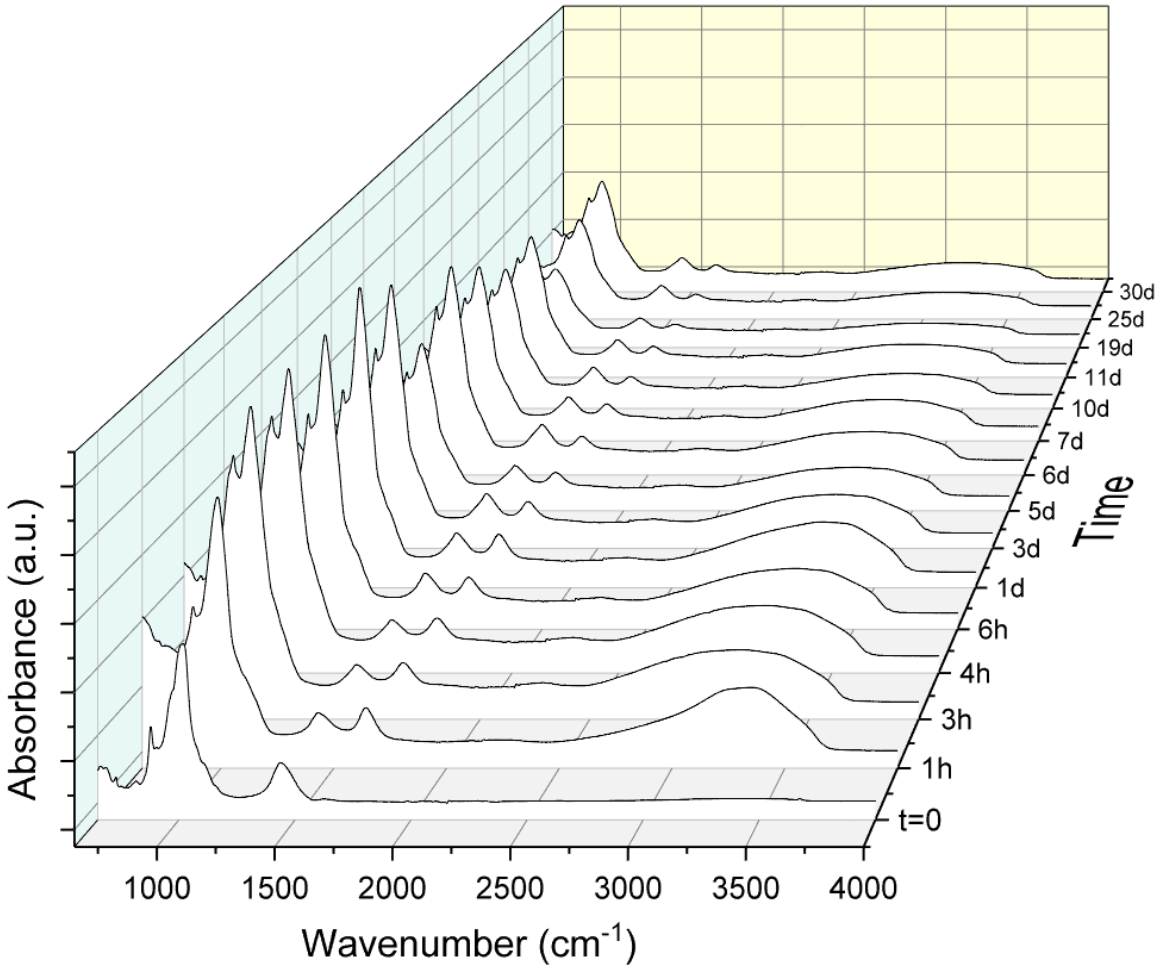

Figure A.9. FTIR data over time for SAAM-9.

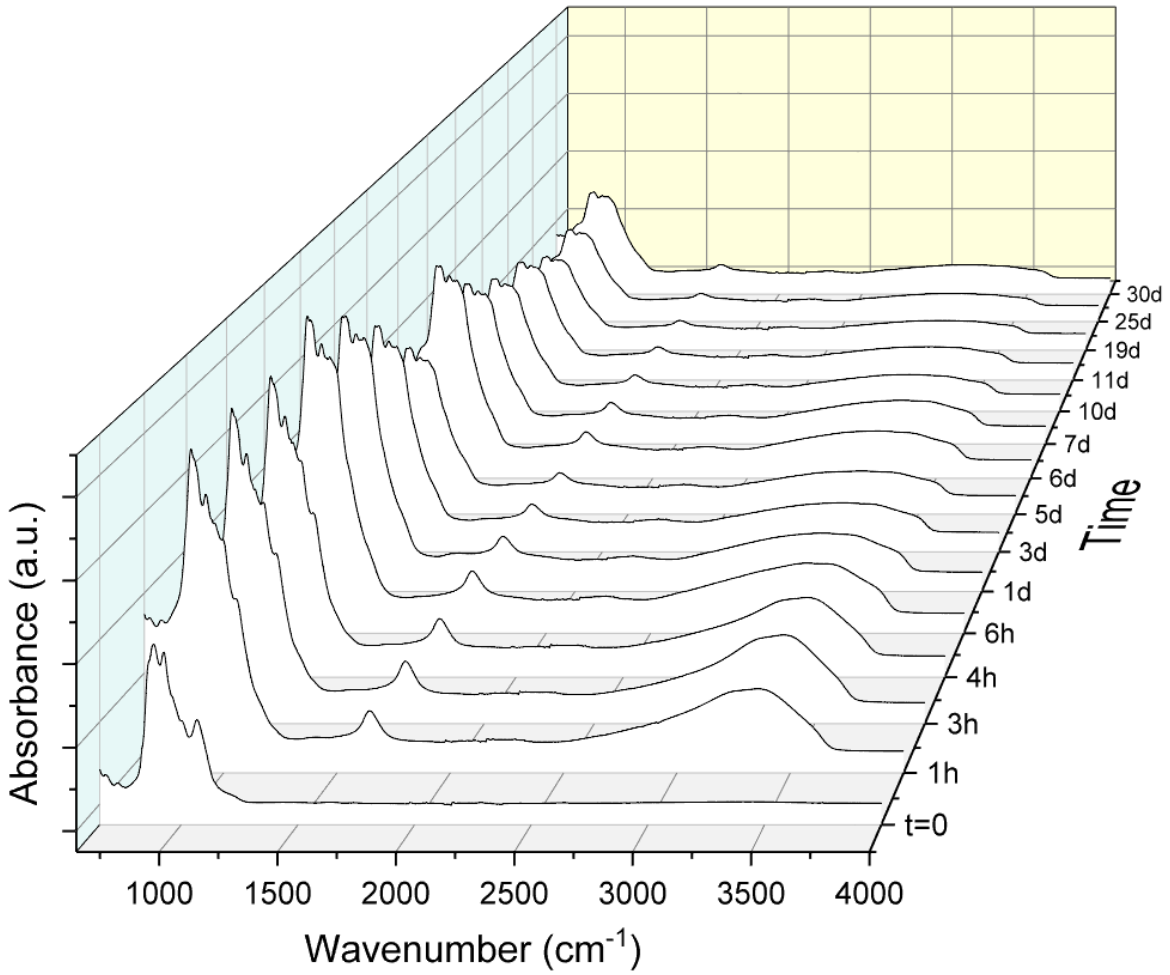

Figure A.10. FTIR data over time for SAAM-10.

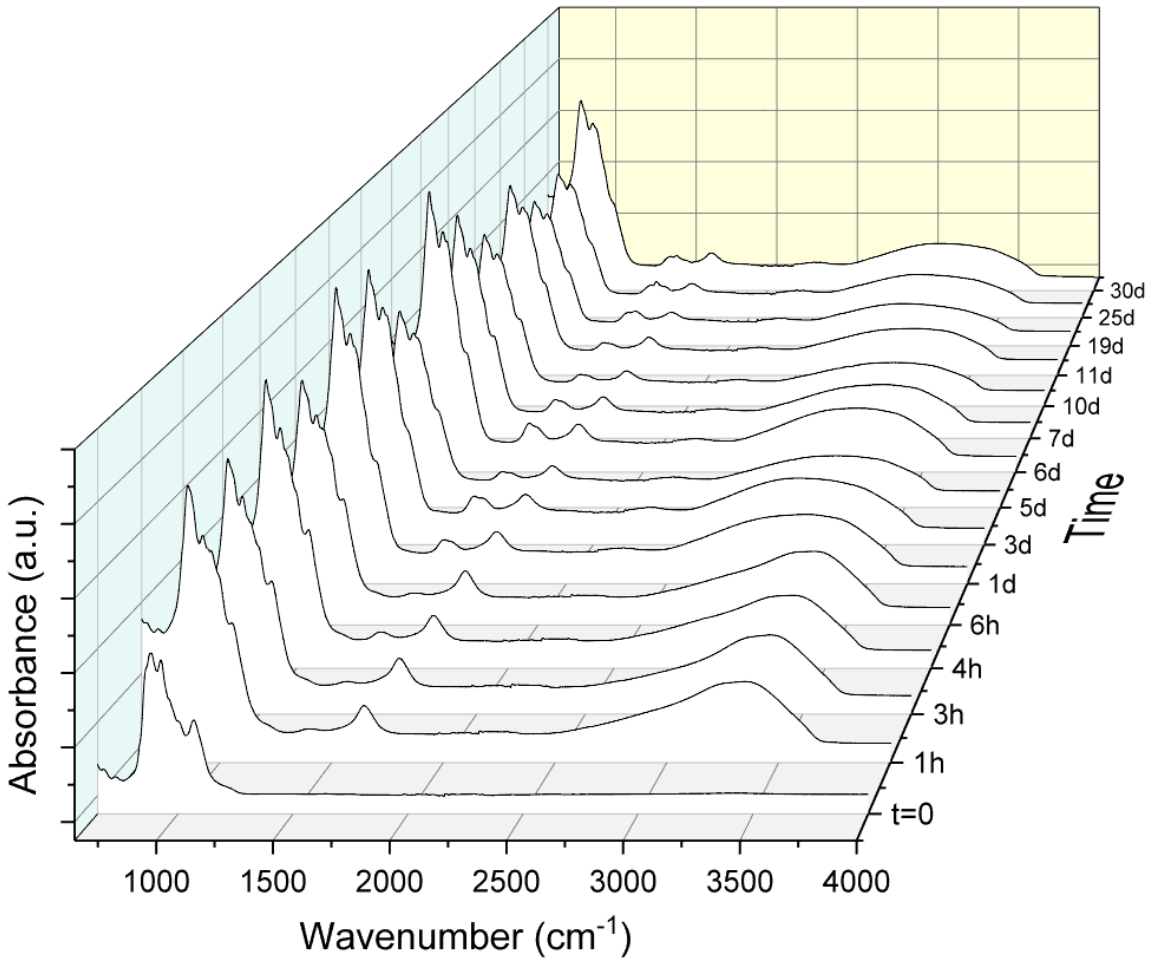

Figure A.11. FTIR data over time for SAAM-11.

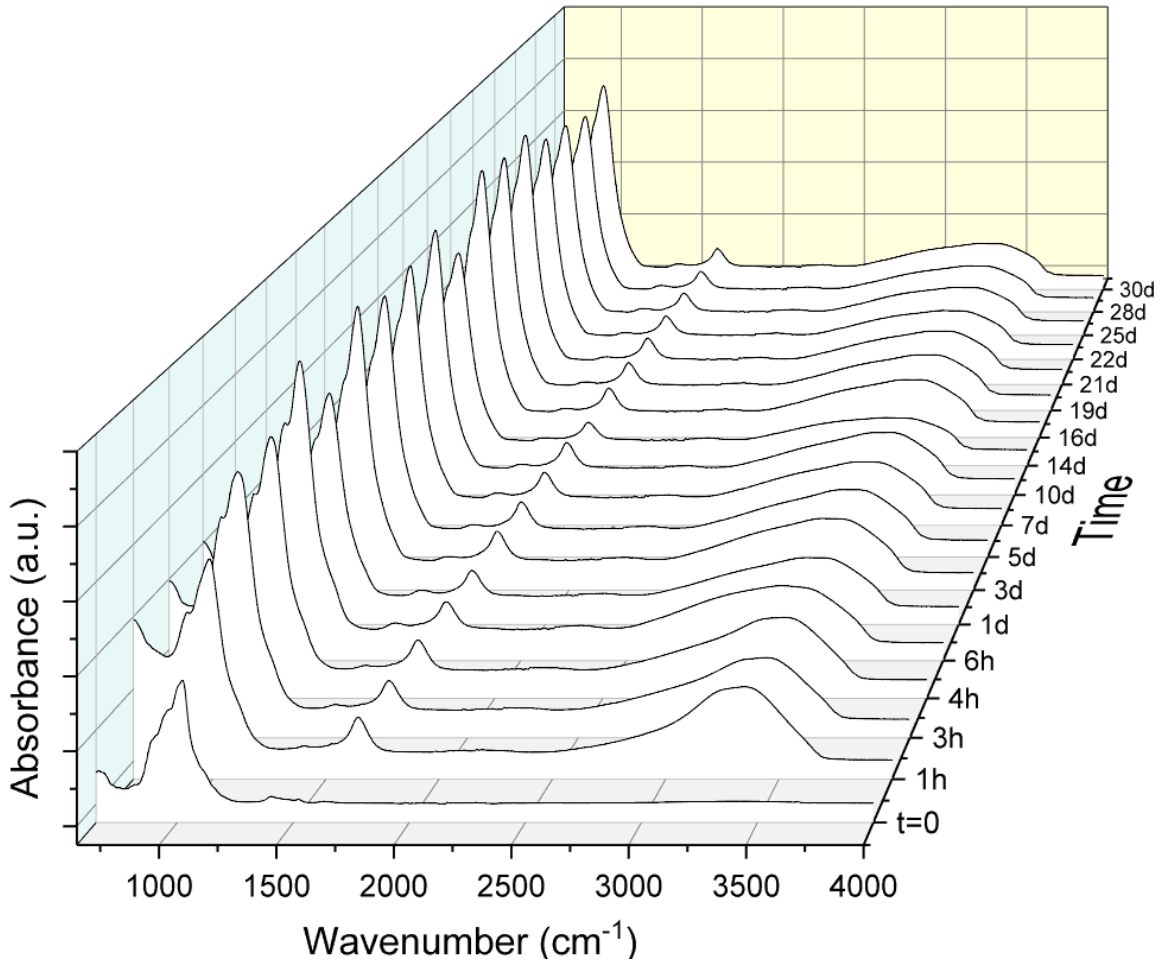

Figure A.12. FTIR data over time for SAAM-12.

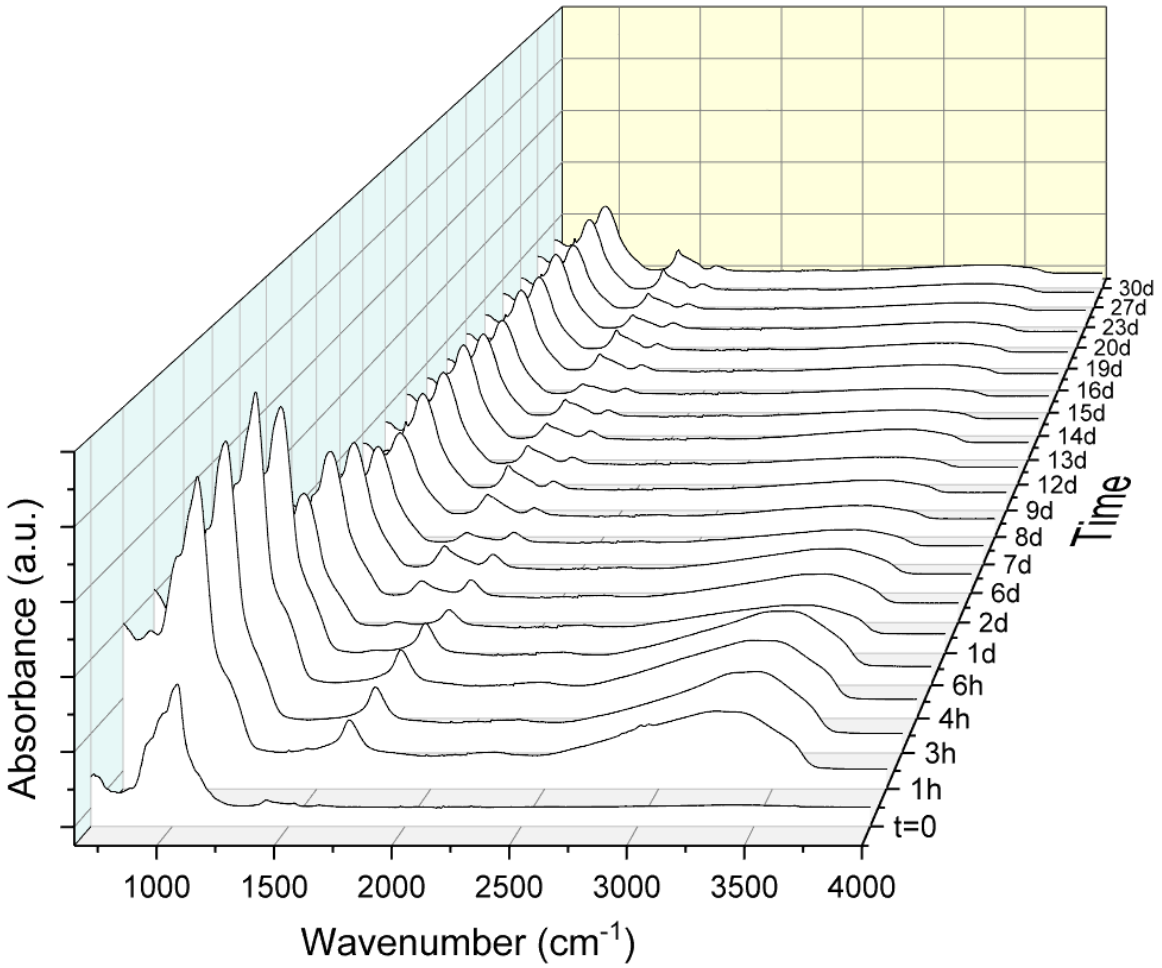

Figure A.13. FTIR data over time for SAAM-13.

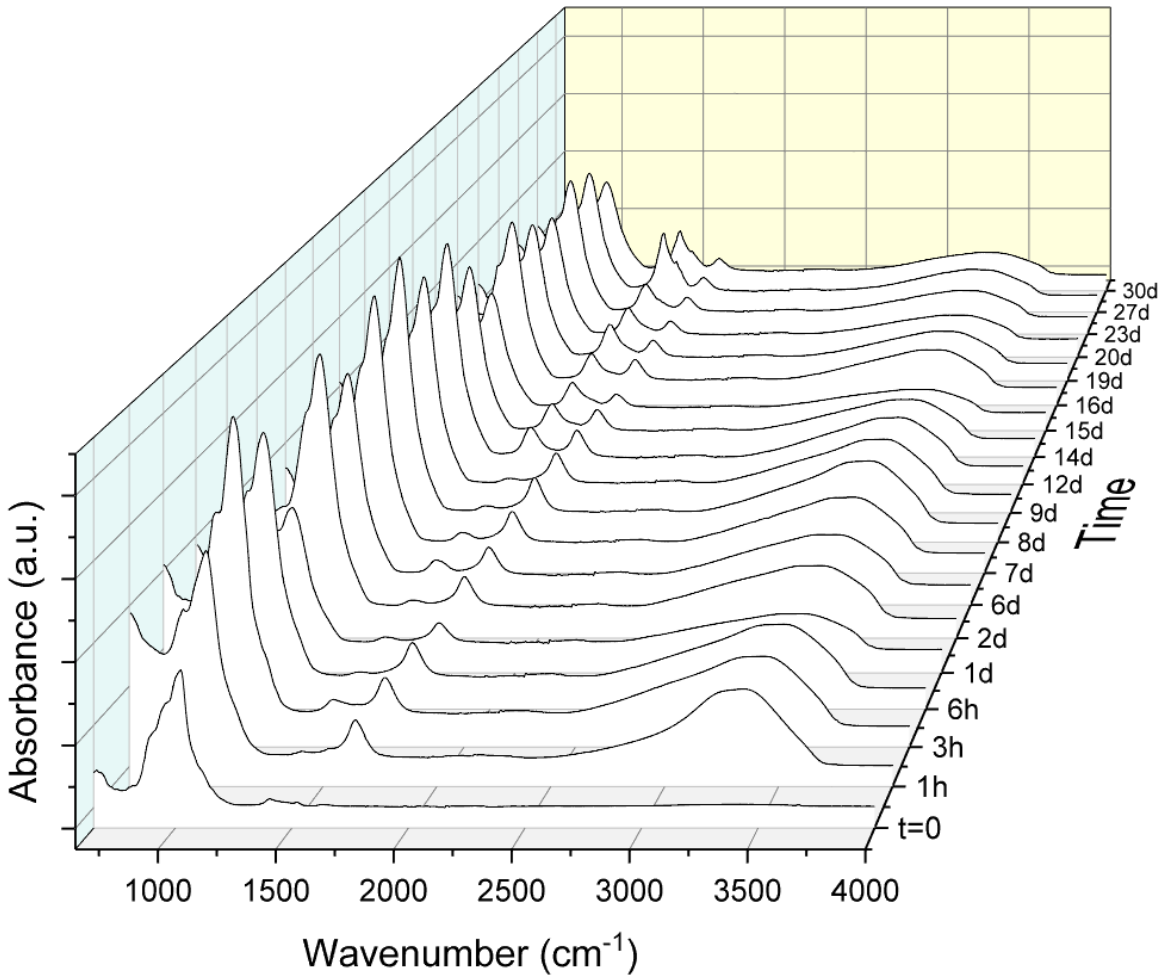

Figure A.14. FTIR data over time for SAAM-14.

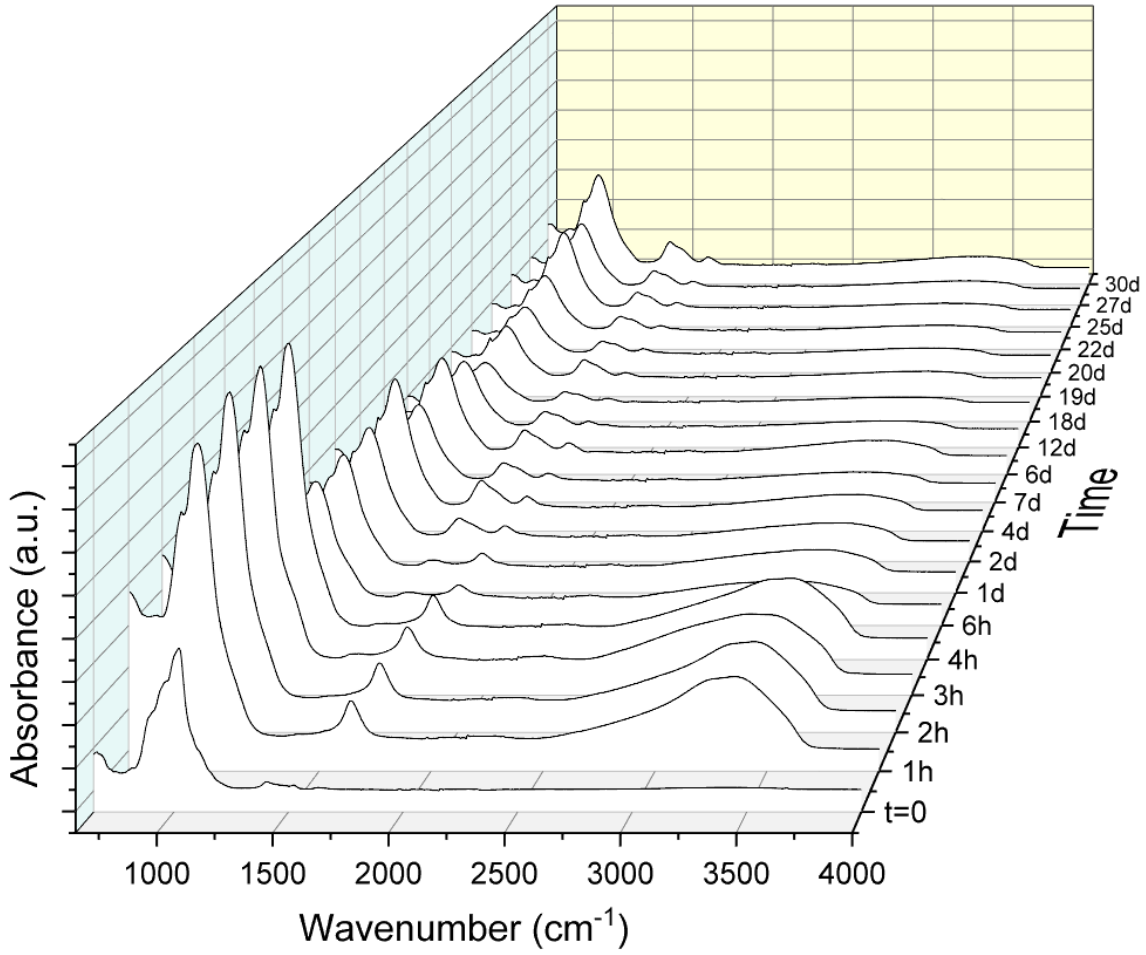

Figure A.15. FTIR data over time for SAAM-15.

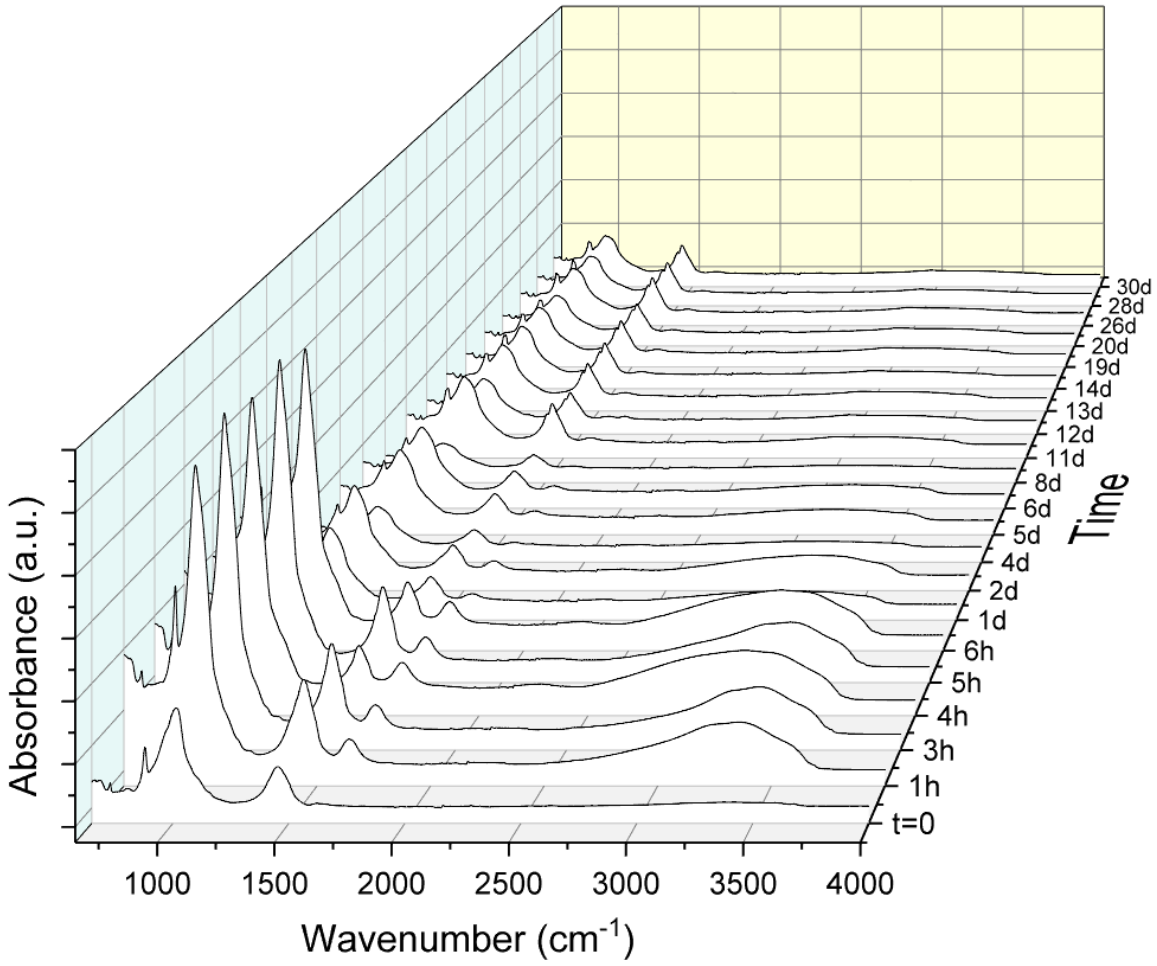

Figure A.16. FTIR data over time for SAAM-16.

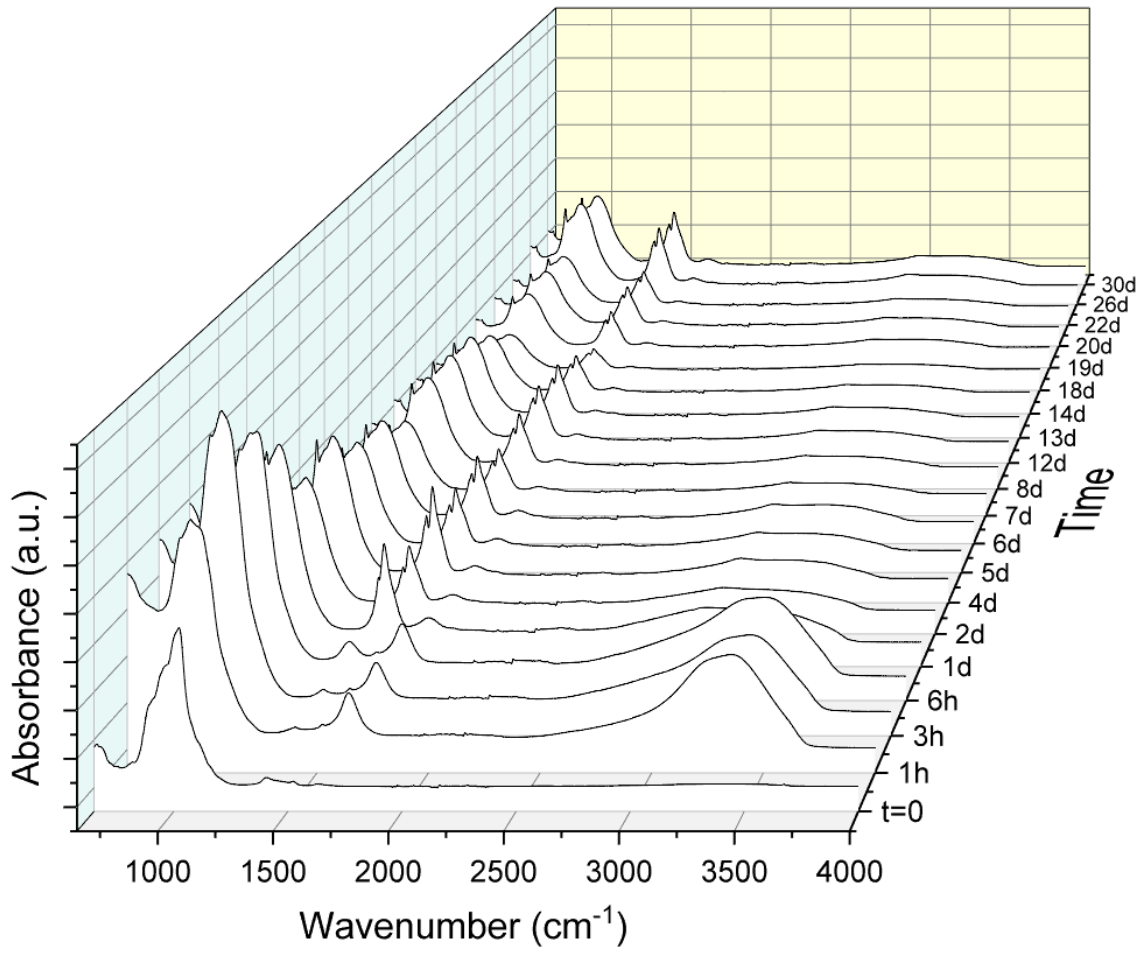

Figure A.17. FTIR data over time for SAAM-17.

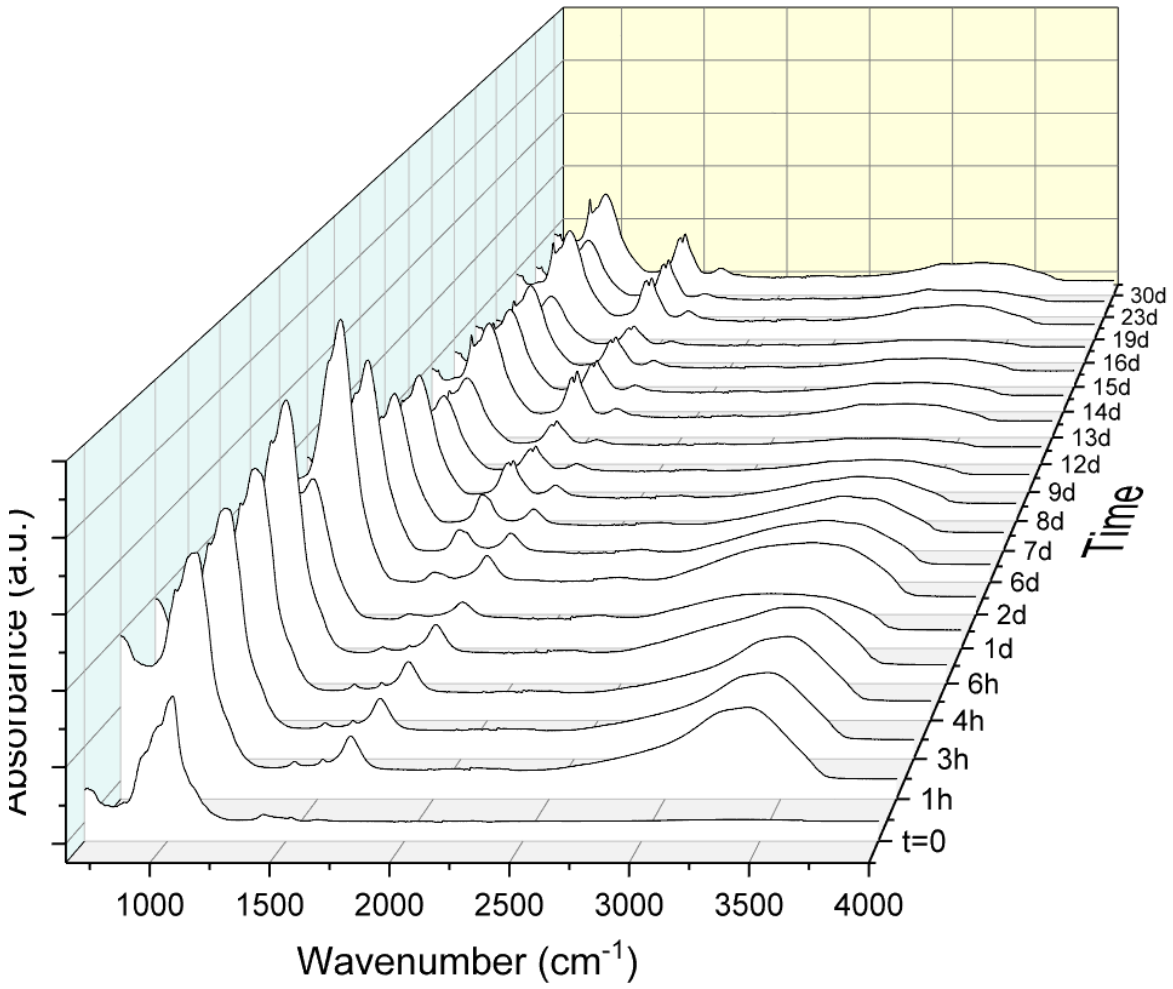

Figure A.18. FTIR data over time for SAAM-18.

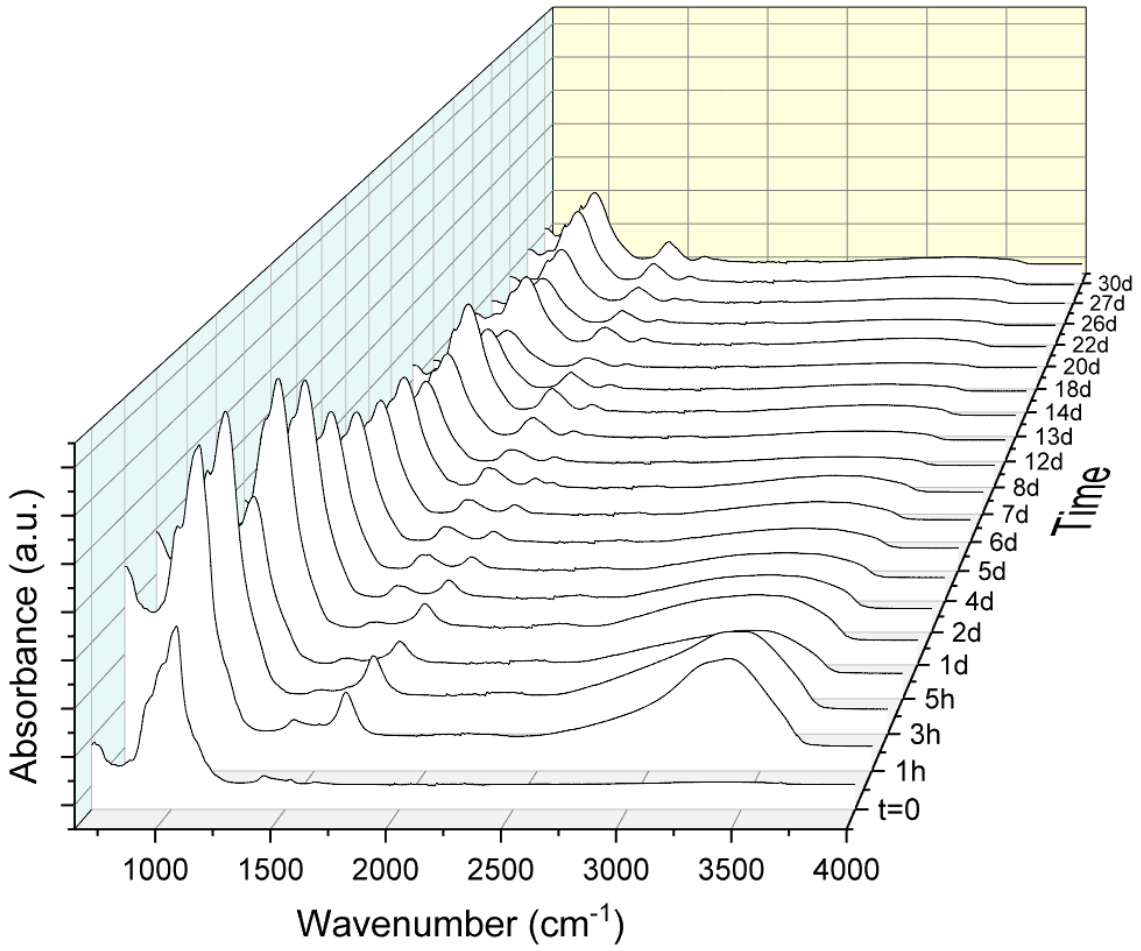

Figure A.19. FTIR data over time for SAAM-19.

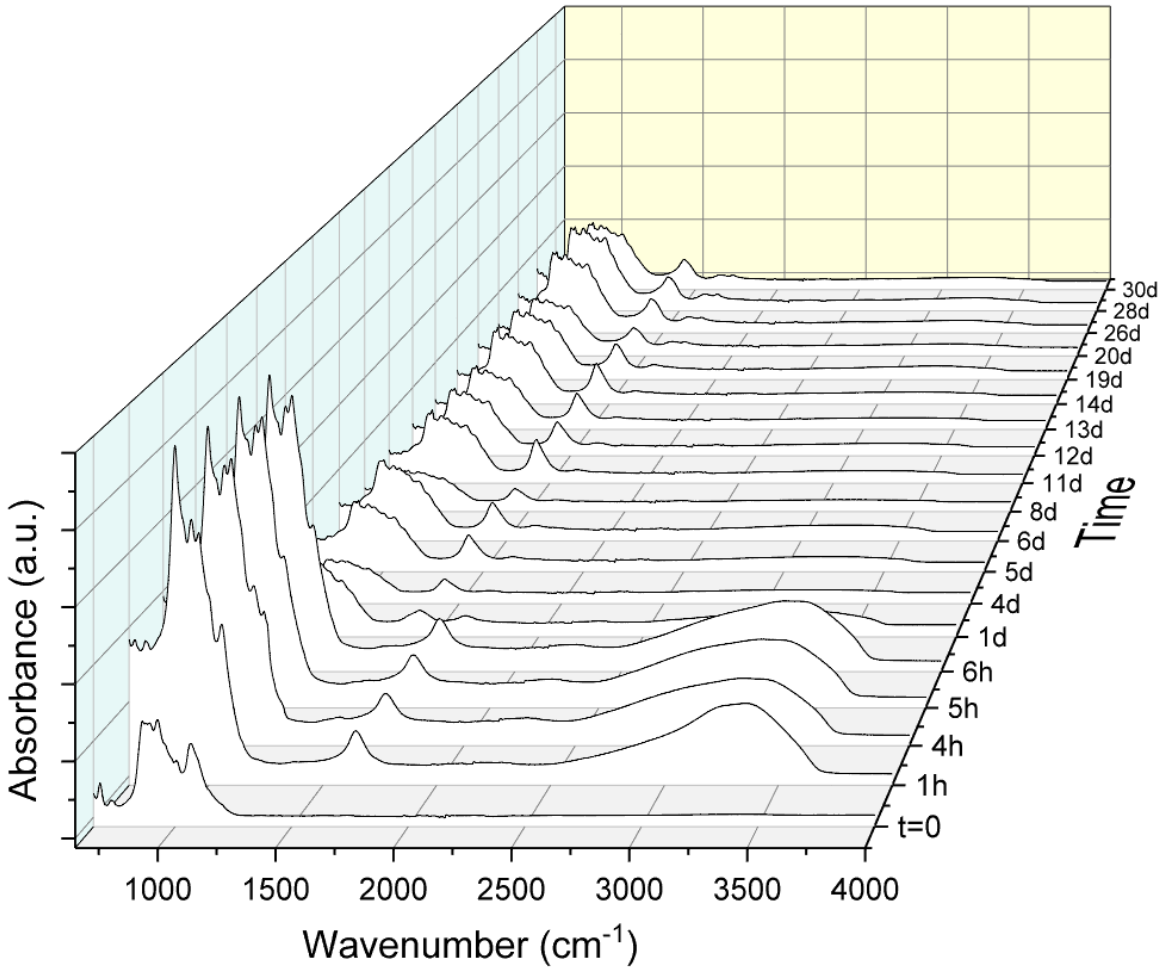

Figure A.20. FTIR data over time for SAAM-20.